Assessment of vision restoration strategies in *ex vivo* photoreceptor-degenerated mouse retina using microelectrode array

Dissertation

zur Erlangung des Grades eines
Doktors der Naturwissenschaften

der Mathematisch-Naturwissenschaftlichen Fakultät
und
der Medizinischen Fakultät
der Eberhard-Karls-Universität Tübingen

vorgelegt
von

Andrea Corna
aus Treviglio, Italien

2021

Tag der mündlichen Prüfung: 26.03.2021

Dekan der Math.-Nat. Fakultät: Prof. Dr. T. Stehle
Dekan der Medizinischen Fakultät: Prof. Dr. B. Pichler

1. Berichterstatter:	Prof. Dr. Günther Zeck
2. Berichterstatter:	Prof. Dr. Eberhart Zrenner
Prüfungskommission:	Prof. Dr. Günther Zeck
	Prof. Dr. Eberhart Zrenner
	Prof. Dr. Jakob H Macke
	Prof. Dr. Katarina Stingl

Erklärung / Declaration:

Ich erkläre, dass ich die zur Promotion eingereichte Arbeit mit dem Titel: „Assessment of vision restoration strategies in *ex vivo* photoreceptor-degenerated mouse retina using microelectrode array“ selbständig verfasst, nur die angegebenen Quellen und Hilfsmittel benutzt und wörtlich oder inhaltlich übernommene Stellen als solche gekennzeichnet habe. Ich versichere an Eides statt, dass diese Angaben wahr sind und dass ich nichts verschwiegen habe. Mir ist be-kannt, dass die falsche Abgabe einer Versicherung an Eides statt mit Freiheitsstrafe bis zu drei Jahren oder mit Geldstrafe bestraft wird.

I hereby declare that I have produced the work entitled “Assessment of vision restoration strategies in *ex vivo* photoreceptor-degenerated mouse retina using microelectrode array”, submitted for the award of a doctorate, on my own (without external help), have used only the sources and aids indicated and have marked passages included from other works, whether verbatim or in content, as such. I swear upon oath that these statements are true and that I have not concealed anything. I am aware that making a false declaration under oath is punishable by a term of imprisonment of up to three years or by a fine.

Tübingen, den ....

Datum / Date Unterschrift /Signature

CONTENTS

ABBREVIATIONS

AMD	age-related macular degeneration
AP	action potential
cGMP	cyclic guanosine monophosphate
CMOS	complementary metal-oxide-semiconductor
e-RF	electrical receptive field
FET	field-effect transistor
FLEX MEA	flexible MEA
HD	high density
HDAC	histone deacetylases
IT	inferior temporal cortex
INL	inner nuclear layer
IPL	inner plexiform layer
LGN	lateral geniculate nucleus
MEA	microelectrode array
MPDA	multi photodiode array
OGFET	open-gate field-effect transistors
OPL	outer plexiform layer
OSFET	oxide-semiconductor field-effect transistors
PCA	principal component analysis
RF	receptive field
RGC	retinal ganglion cell
RP	retinitis pigmentosa
RPE	retinal pigment epithelium
STA	spike-triggered average
V1	primary visual cortex
v-RF	visual receptive field

ABSTRACT

Millions of people worldwide suffer from retina degeneration pathologies. To this day the only clinically approved treatment for these pathologies are retina implants. However, state of the art implants fail to rescue vision beyond the level of legal blindness. New stimulation strategies are therefore required to improve retina implant performances, and new treatments must be developed to avoid or delay retina degeneration. In this framework, microelectrode arrays represent an optimal platform to investigate vision restoration strategies *in vitro*.

In the dissertation three different studies are included, with the goal of evaluating current approaches to vision restoration and to investigate new solutions to improve artificial vision. (1) I investigated subretinal electrical pulsatile stimulation of photoreceptor-degenerated mouse retina (*rd10* strain) using the retina implant ALPHA AMS R3 chip. I demonstrated efficient and safe stimulation with a single 30 µm electrode. I evaluated the charge threshold dependency with electrode size and reported non-monotonic stimulus response relationship. (2) Using a high-density CMOS based microelectrode array, I evaluated spatial and contrast resolution obtained by sinusoidal epiretinal stimulation. I demonstrated reliable and continuous stimulation without fading and axonal stimulation. Using a logistic regression model to analyze RGCs responses with simple shapes stimulation, I demonstrated high accuracy discrimination of spatial object displacement of 32 µm and artificial contrast level of 10%. (3) Evaluating light responsiveness of organotypic retina culture, I contributed to the assessment of the efficacy of HDAC inhibition to improve cone survival in retinitis pigmentosa.

1 SYNOPSIS

Vision is one of the fundamental senses, serving as one of the primary means of interaction with the world. For people suffering from late stage retina degeneration pathologies, vision is lost, deeply affecting life quality. Retina degeneration affects the ability of the retina to detect light, leading initially to vision impairment, and eventually to blindness. Degeneration affects the photosensitive layer of the retina and only partially the remaining retina structure, while connection to higher brain structure is still functional. Exploiting the remaining retina functionality and artificially restoring photosensitivity is possible to recover vision. Different approaches have been proposed to achieve artificial vision. However, to date the only clinically approved therapy for these patients are retina prosthetics.

Retina prosthetics aim to restore vision by electrically stimulating the retina using an implanted microchip, converting light in electrical pulses. The idea of using electrical stimulation to elicit visual percept is one century old [1] and it was applied to vision restoration more than 50 years ago [2]. But the technology able to implement this approach to implanted clinical devices has been developed only much later [3, 4]. During the early 2000s, several groups around the world started developing such devices, and within 10-15 years retina implants obtained clinical approval [5, 6]. However, despite the great efforts and remarkable results in the field, current technology is still far from achieving a full sight recovery. The two implants that reached the market, the Retina Implant ALPHA AMS (Retina Implant AG, Reutlingen Germany) and the ARGUS II (Second Sight, Sylmar CA, USA), were discon-

tinued in 2019. The main drawback of these implants was the poor degree of vision restoration, especially compared to patients' expectations. In addition, more and more alternative solutions provided by portable electronics, i.e. smartphone apps, offer life quality improvement without the need of invasive surgical procedures [7].

The future of Retina prosthetics relies on the capacity to overcome several limitations of the current clinical outcomes. There is a need for faster and less invasive surgical procedures. New Implant designs are required to achieve chronic stability and larger visual field. But most importantly new stimulation strategies must be developed to achieve higher spatial resolution and improved contrast.

Long regulatory process slows down the implementation of lab-tested technical solutions to clinical devices [7]. Advancement of *in vitro* testing is therefore crucial to develop new stimulation strategies, and to bridge the gap between laboratory and clinical conditions. In this framework, modern microelectrode arrays provide a powerful tool. Here I show how this technology can be applied to study artificial vision and treatment for retina degeneration.

In the dissertation three different studies are included, with the goal of evaluating current approaches to vision restoration and to investigate new solutions to improve artificial vision. First, I investigated electrical stimulation using the retina implant ALPHA AMS R3 chip. I demonstrated the stimulation of retinal ganglion cell activity in photoreceptor-degenerated mouse retina (*rd10* strain) with single pixels of the chip in *ex vivo* subretinal configuration. In the same configuration I investigated charge threshold dependency with electrode size and non-monotonic stimulus response relationships (Chapter 2). Secondly, using a high-density CMOS based microelectrode array I demonstrated continuous, reliable and spatially localized

sinusoidal stimulation in epiretinal configuration without axonal activation. For this stimulation strategy, the discrimination accuracy of spatial displacement and artificial contrast upon simple shapes stimulation was evaluates whit a logistic regression model (Chapter 3). Thirdly, I contributed to the assessment of the efficacy of HDAC inhibition to improve cone survival in retinitis pigmentosa, as an alternative or complementary treatment to retina implants (Chapter 4).

1.1 MICRO ELECTRODE ARRAYS A PLATFORM TO STUDY VISION RESTORATION

1.1.1 *Visual System*

The visual system is the part of the central nervous system allowing visual perception. Its function is to sense the visual input and elaborate it to extract visual information. Its structure is very well conserved across animal species, in this document I will especially focus on human and mammalian visual systems. Visual system is composed of a sensory organ, the eye, a part of the human cerebral cortex, the visual cortex, and the neuronal pathway that connects them.

The first step of vision happens in the retina, where photoreceptors, a light sensitive neuron, transduce the light in an electrical signal. The output of the retina is conveyed by the optic nerve and is transmitted to the lateral geniculate nucleus (LGN) and from the LGN to the primary visual cortex (V1). From V1 the visual signal is elaborated along different visual pathways involving specific areas of the visual and cerebral cortex. Each pathway and area extracts and elaborates specific features of the visual stimulus and the different visual information are processed in parallel. According to the "two-streams hypothesis" [8] two main visual streams can be identified in humans, the dorsal and the ventral stream. The dorsal stream, comprising V1, V2, V3 and V5/MT, is involved in guided motor behaviors. The ventral stream, comprising V1, V2, V4 and the inferior temporal cortex (IT), is involved in object and face recognition. (Figure 1.1, A).

Parallel processing of different information of the visual input is one of the mechanisms at the base of visual system information processing efficiency. Every element of the visual system performs a signal processing step, where

only relevant information are extracted while unnecessary ones are discarded. Most importantly every element of the pathway is developed to receive and transmit exclusively specific signals. Retina is not only responsible for phototransduction but provides the first steps of visual information processing. Some of the major limitations of current retina implants arise from their incapability to restore these functions. Understanding retina signal processing of the retina and how to possibly replicate it is therefore crucial to achieve vision restoration via retina stimulation. Retina functionality arises from his peculiar structure and anatomy, that will be described in detail in the next dedicated section.

1.1.2 *Retina structure and functionality*

Retina includes five major cell types and its structure is divided in three nuclear and two synaptic layers (Figure 1.1, B):

PHOTORECEPTOR The outer layer, located towards the back of the eye in contact with the retinal pigment epithelium, is composed by two types of photo sensitive neurons (photoreceptors): the rods and the cones. Photoreceptors are responsible for visual photo-transduction, the mechanism translating light in electrical signals. A photoreceptor is composed of four anatomical regions, the synaptic terminal, the nucleus, the inner segment and the outer segment. The photoreceptor outer segment contains the light-sensitive protein responsible for the cell photosensitivity. When unstimulated (resting state, in the dark), photoreceptors are depolarized by the influx of sodium ions through GMP-gated membrane channels ("dark-current"). The light-sensitive protein contained in the outer segment is composed by a chromophore bound to an opsin, a cell membrane protein. When hit by

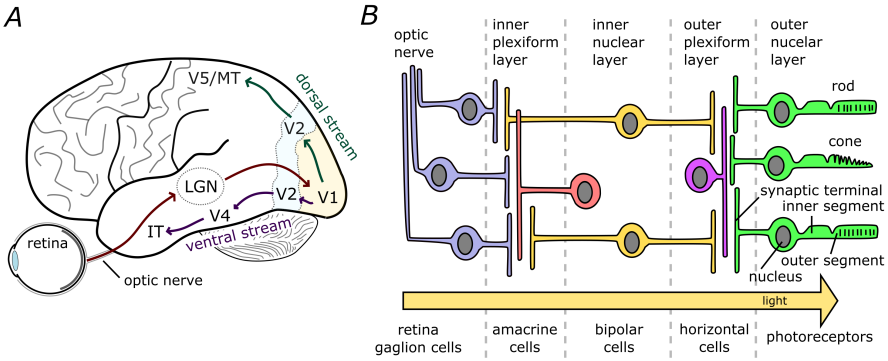

Figure 1.1: (A) The visual system structure and the retina anatomy with its major cell classes. Incoming light is projected by the eye optics on the retina. The visual input is processed by the retina, and traveling across the optic nerve is transmitted to the LGN and then to V1. From V1 the visual signal is elaborated along two different visual streams: The dorsal stream comprising V1, V2, V3 and V5/MT and the ventral stream comprising V1, V2, V4 and IT.
(B) Retina structure and anatomy. Retina performs two main functions, one is phototransduction, i.e. converting light input in electrical signal, and the second is to extract visual features from visual input and transmit them to the visual cortex. Photoreceptors cells are responsible for phototransduction. In the retina there are two types of photoreceptors, rods and cones. Signal processing is guaranteed by retina structure and anatomy. Together with the photoreceptor, in the retina there are 4 other main cell classes: bipolar cells, retinal ganglion cells (RGCs), horizontal cells and amacrine cells. Photoreceptor, bipolar cells and horizontal cell synapsis connect in the outer plexiform layer (OPL). Bipolar cells, RGCs and amacrine cells connect in the inner plexiform layer (IPL).

a photon the chromophore undergoes photoisomerization and the opsin undergoes a conformational change leading to a signal transduction cascades lowering the intracellular concentration of cGMP (cyclic guanosine monophosphate) [9]. The lower concentration of cGMP causes the closure of GMP-gated sodium channels, blocking the dark current and hyperpolarizing the cell. The hyperpolarization causes calcium channels to close that results in a decrease of glutamate release in the synapsis with the bipolar cells. The phototransduction cycle ends with the photoreceptor returning to its original resting state .

The light-sensitive protein contained in the rods is the rhodopsin, while cones can contain different light-sensitive proteins (photopsins) with different absorption spectrum. Based on the absorption spectrum of the photopsin, in primates there types of cones can be identified: S-cones, M-cones, and L-cones (short, medium, and long wavelengths). Cone differentiation is at the base of color vision.

Rods and cones are differentiated by the light intensity level in which they operate. Rods are responsible for vision at low intensity levels, i.e. night vision. Cones instead are active in day-light vision. In humans and some other mammalians, the central area of the retina, the macula, contains almost entirely cones. In the central part of the macula, the fovea, photoreceptors are connected with a single bipolar cell and RGC to generate high acuity vision. Mouse retina, the animal model used in the studies presented here, has a comparable structure to primate retina. However, it only contains S- and M-cones, and does not have a fovea.

BIPOLAR, HORIZONTAL AND AMACRINE CELLS The central nuclear layer of the retina is the inner nuclear layer (INL). It contains the nuclei of three different cell types, the bipolar cells, the horizontal cells and amacrine

cells. Bipolar cells synaptically connect to photoreceptors in the outer plexiform layer (OPL) and to retinal ganglion cells (RGCs) in the inner plexiform layer (IPL). Bipolar cells receive input exclusively from a single photoreceptor type, and therefore it is possible to identify rod bipolar cells and cone bipolar cells. Rod bipolar cells are activated solely by rod depolarization to incoming light. Cone bipolar cells instead, can be classified as ON or OFF. ON-bipolar cells are depolarized by a light intensity increase (decrease of glutamate release due to cone phototransduction), while OFF-bipolar cells are hyperpolarized. The diverse response of the cone bipolar cell arises from the receptor type in the synapsis with the photoreceptor, metabotropic for ON-bipolar cells and ionotropic for OFF-bipolar cells.
Horizontal and amacrine cells are exclusively connected inside the synaptic layers, respectively in the outer and the inner plexiform layer. They do not transmit the signal across the retina but through lateral inhibition along the horizontal pathway, serving in several image processing functions. For example, horizontal cells integrating signals from several photoreceptors provide inhibitory feedback to the photoreceptors playing a crucial role in the antagonistic center-surround organization of bipolar and retinal ganglion cells receptive fields (RF) (see next paragraph). Acting on the photoreceptor-bipolar cell synapse they also modulate retina response in respect of environmental light conditions, increasing the light intensity range of retina response.

RETINAL GANGLION CELLS The last nuclear cell layer of the retina is the RGC layer. RGCs receive inputs from bipolar and amacrine cells and their axons collect in the optic nerve to connect to the LGN. RGCs are, with few exceptions, the only cell type in the retina generating action potentials. RCGs can be morphologically identified in two major classes, midget and

parasol cells. Midget cells are characterized by their smaller size and a more confined receptive field when compared to the parasol cells.

RGCs can be also classified based on their functionality, i.e. the visual feature extracted from the light input, that is defined by the RGC visual receptive field (v-RF, or RF for simplicity). For a sensory neuron a receptive field is the portion of the sensory space that, if stimulated, elicits a response in the neuron. A receptive field has a spatial dimension but can also include other parameters as time or, for a v-RF, light intensity or light pattern [10]. Each RGC collects signals from several bipolar cells and therefore from several photoreceptors (Figure 1.2, A). The portion of the visual field covered by the photoreceptor connected to a RGC defines the spatial extent of the RF. The processing of the visual input done by the receptive field network, defines the spatio-temporal pattern of the stimulus activating the cell. Together, all the receptive fields of RGCs are organized as a mosaic, fully covering and spatially segmenting the visual field. The main classification divides RGC in center-surround receptive fields. ON-center neurons respond to a light spot on a dark surround and OFF-center neurons to a dark spot on a dark surround (Figure 1.1, B). However, the complete RGC classification is more complex. For example, some RGC could respond to selective directional motion or to color. In recent studies at least 32 different RGC types were identified in mice [11].

Due to the current limitations of the technology, in the field of retina implants, a simplified functional classification in only two RGC types is used. RGC are classified on ON and OFF cells based on the polarity of the receptive field centers. An ON RGC increases its firing rate upon stimulation with incremental light, while the same stimulus reduces the activity of the OFF RGC.

RGCs can be also classified based on the response firing patterns' frequency

or duration. A cell can be defined as "brisk" or "sluggish" if it produces respectively a high or low firing rate response. A brisk or sluggish cell can be in turn transient or sustained. Transient cells generate a short burst in response to an intensity change; sustained cells are active across the full length of the stimulus [12, 13].

In mouse retina, cones cell density is ~12,400 cells/mm^2 while RGCs density is only ~3300 cells/mm^2, resulting in a ratio close to 4:1 [17]. In humans the ratio is supposed to be lower and more variable between central, especially in the fovea, and peripheral retina [18], however still larger than one. The size difference of the two cell populations represents a true bottleneck in terms of the amount of visual information that can be transmitted to the visual cortex. Retina cannot transmit all the information collected by photoreceptors across the optic nerve, but must process the visual input to reduce the number of information. To achieve this, retina uses different RGC RF to extract different features from the visual input creating different neuronal representations of the visual stimuli that will be processed by the visual system (Figure 1.2, C) . Each representation will be a simplified version of the original input including a specific visual information.

1.1.3 *Micro electrode array*

The retina and the visual system are a part of the central nervous system. To understand retina functionality, and how to restore it, we need to understand how neural networks work and how the brain transmits and elaborates information and which techniques can be used to study or modulate it. The nervous system is able to acquire and process a large amount of information at millisecond time scale. To perform its functions, it operates at different

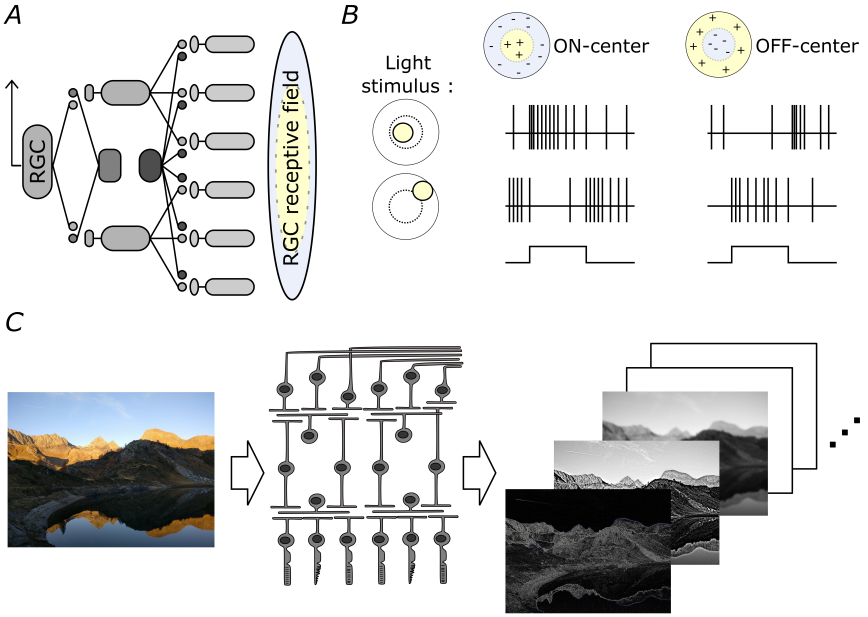

Figure 1.2:
(A) Schematic of the visual RGC receptive field. Each RGC integrates and elaborates signals from several photoreceptors, horizontal, bipolar and amacrine cells. The network topology and the type of synaptic connection of a RGC with the other retina cells define the RGC RF type, i.e. the stimulus parameters that evoke a response of that cell. (B) Schematic representation of the two major receptive field types in the retina and their responses to different light stimuli. An ON-center RGC responds to a light stimulus in RF center with an increase of firing rate, while an OFF-center cell responds with a decrease. The response pattern is inverted in case of a light stimulus in the RF surround.
(C) Schematic of retina signal processing. Different receptive fields extract different features from the visual input, i.e. image edges, colors and motion. Different RGC functional classes create multiple neural representations of the original image that are processed by the visual system. The same principle, but to a higher level of abstraction with more complex RF, is common across the visual system. Adapted from: A [14], B [15] and C [16].

spatial and temporal scales, relying on different chemical or physical processes. However the brain's basic function can be almost solely inferred from the neural network topology, and from the type and strength of connections between neurons. Neurons, the basic building block of the nervous system, are electrically excitable cells, and they communicate between each other with electrical signals, the action potentials (AP). The AP can be considered, in similitude with electronics, as the "bit" or the smaller piece of information transmitted across the nervous system.

During the action potential, the ion flux through the membrane generates an electrical gradient across the neuron cell membrane, and in a localized area around the neuron. Electrophysiological techniques allow to measure this gradient, both across the cell membrane using intracellular recording or outside the cell with extracellular recording. Commonly an AP recorded extracellularly is referred to as a "spike".

Intracellular recording, such as the patch clamp technique, uses micro-metric electrodes to access the cytoplasm in order to measure the intracellular voltage, or the currents across the membrane. Even though these techniques are very powerful tools, patch clamp and intracellular recording techniques are generally limited to few cells per experiment [19, 20]. Simultaneously recording a large population of neurons is possible using a combination of multiple extracellular electrodes. Such devices with micron-sized electrodes are called microelectrode arrays (MEAs). The first MEAs proposed more than 50 years ago contained only a few dozens of electrodes [21]. Technological advances allowed to increase the number of electrodes and the electrode density to current MEAs containing thousands of electrodes in a few millimeters. MEAs can be used to record *ex vivo* neural tissue or, with implanted devices, neural activity of living animals. Based on their application, they are classified as *in vitro* or *in vivo*.

in vitro MEAs can be used to study different experimental models, such as brain slices or cell cultures. Due to the peculiar planar layered structure of retina, MEAs allows an optimal interfacing with the tissue, offering an ideal device to *in vitro* studies of RGCs activity. MEAs recording of dissected retina or of organotypic retina cultures allows simultaneous recording of a large population of RGCs, providing access to retina information encoding.

STANDARD PASSIVE MEAS AND ACTIVE CMOS MEAS Standard *in vitro* MEAs consist of a conductive material electrode micro-fabricated on an insulating surface. This technology provides the possibility to produce high signal to noise ratio electrodes at a sustainable cost (Figure 1.3, A and 1.4, A). A standard glass MEA was used in Chapter 4 to study light response of organotypic retina culture.

Due to physical and fabrication constraints, the channel density of passive MEA is limited to hundreds of electrodes for millimeter square. In addition, standard MEA recording setup consists of a headstage where the MEA chip is inserted to connect the electrodes to an external hardware for the amplification and the digitalization of the signal. The necessity to connect each electrode, due to necessary wiring, further limits the electrode density. To overcome these limitations the latest generation of MEAs implemented complementary-metal-oxide semiconductor (CMOS) technology (Figure 1.3, C and 1.4, B) [22]. CMOS MEAs use transistor based electrodes (open-gate field-effect transistors, OGFETs, or oxide-semiconductor FET, OSFET) instead of standard conductive electrodes. Appling CMOS fabrication technology is possible to increase channel number and density to thousands of electrodes in a few millimeter squares. It is impossible to simultaneously connect such a large number of electrodes to an external hardware, and therefore it is required to time-multiplex the signals. CMOS technology allows to

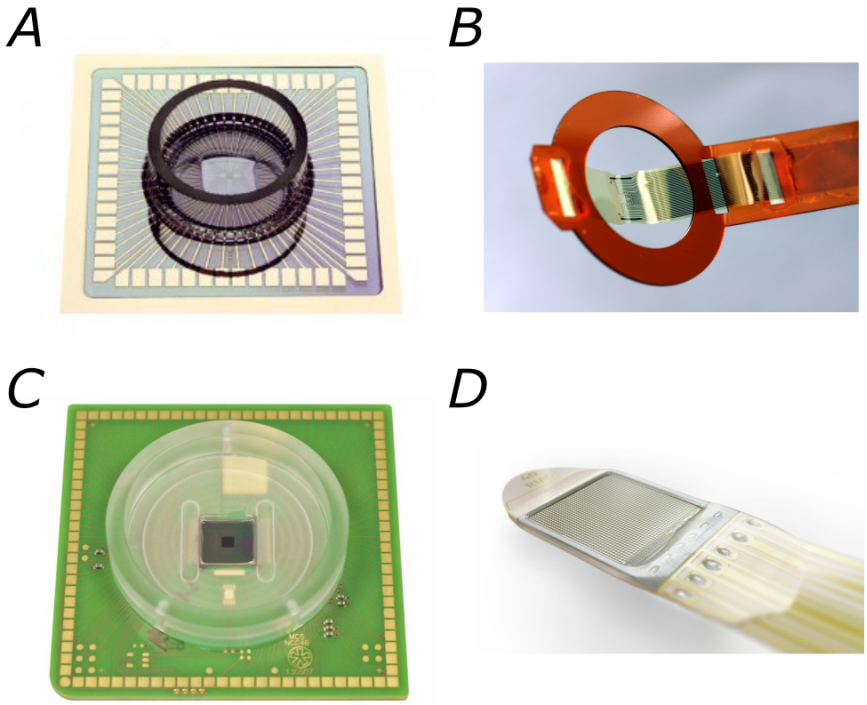

Figure 1.3: Micro-electrode array (MEA) types. (A) Passive glass MEA. A passive MEA consists of an array of conductive materials electrodes micro fabricated on an inert substrate, i.e. glass. Each electrode is connected through a headstage with metallic pins to the recording hardware. A passive MEA can contain hundreds of electrodes for millimeter square. (B) Flexible MEA (FLEX MEA). The working principle of a FLEX MEA is the same as a passive MEA, with the difference that a soft material, usually a polymeric material, is used instead of a rigid one as a substrate. The mechanical properties of the flexible substrate allow better adhesion with the tissue creating a better tissue-electrode interface and avoiding tissue damage. (C) High density CMOS MEA. CMOS MEAs use complementary-metal-oxide semiconductor (CMOS) technology for the production of the electrode array. CMOS technology allows to increase channel density to thousands of electrodes for millimeter square and to include the multiplexing electronics in the array chip. CMOS MEA uses transistor based electrodes instead of standard passive electrodes, for this reason they are commonly called "active electrodes". (D) The Multi photodiode array (MPDA) of a retina implant. Retina implants use an array of stimulating electrodes to restore light sensitivity electrically stimulating the retina. In this implant each stimulating electrode is connected to a photodiode, the photodiode adjusts the stimulating current based on the incoming light, restoring phototransduction. Credits: (A,B) Multi Channel Systems MCS GmbH, (D) Retina Implant AG.

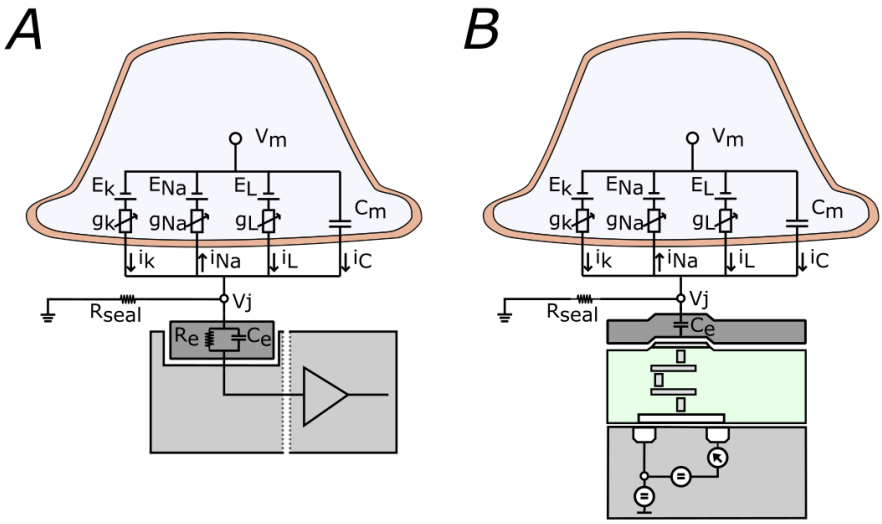

Figure 1.4: Electrode-neuron point contact model for (A) a passive electrode and (B) a CMOS electrode. In the passive MEA each electrode is connected to external electronics which amplify and digitize the signal. CMOS technology allows to include on the MEA chip the multiplexing electronics and the EOSFET sensor (shown in the drawing). With this approach it is possible to increase the channel density to subcellular resolution. Figure adapted from [23].

.

integrate the multiplexing electronics directly in the MEA chip, reducing the required connections to the headstage. Due to the different electrode design, CMOS MEAs are often referred to as "active" electrode MEAs, in contrast to "passive" electrodes for standard MEA. A CMOS MEA was used in Chapter 3 to study epiretinal sinusoidal stimulation with *ex vivo* retina tissue.

FLEXIBLE MEAS In a different technology developmental line, some MEAs were not developed to optimize the channel density, but with the goal of implementing soft materials in order to match MEA mechanical properties with the neuronal tissue, to improve long term stability for chronic devices or to improve tissue adhesion in *in vitro* solution. An example of a flexible MEA

(FLEX MEA), is shown in Figure 1.3, B. This MEA was used in the study presented in Chapter 2, in combination with the retina implant ALPHA AMS chip (Figure 1.3, D), to stimulate the retina from the photoreceptor side, while recording the RGC activity. The flexible MEA is based on a polyimide substrate with titanium nitride leads and electrodes. To enable oxygenation of the interfaced retina the polyimide foil has been perforated.

EXTRACELLULAR RECORDING - NEURON-ELECTRODE INTERFACE To understand extracellular recording, it is possible to model an exemplary situation of a single neuron attached on top of a MEA electrode. This representation is known as the point-contact model, [24–26]. The model assumes a tight seal between the neuron membrane and the electrode and describes the extracellular voltage in the junction between neuron and recording electrode as a single point. This ideal condition mimics closely the neuron-electrode interface in a dissociated cell culture recording. In real experimental conditions, with more heterogeneous nervous tissue, i.e. retina recording, this assumption may not be valid. However, the point-contact model provides a qualitatively valid framework to understand the basics of extracellular recording. A scheme of the model is shown in Figure 1.4. The neuron's membrane is represented as an equivalent electric circuit based on the Hodgkin-Huxley model [27]. The current across the membrane has an ionic and a capacitive component. The ionic current is generated by voltage-gated channels: potassium and sodium, plus a leakage current, mainly chlorine ions. Each ionic element has a specific conductance (g_x) and a reversal potential (E_x) as a function of ion gradient inside and outside that membrane. Ions' conductances are non-linear and voltage and time dependent. The capacitive current (i_c) derives from the insulating properties of the membrane. The major approximation of the model is that the medium in the cleft can

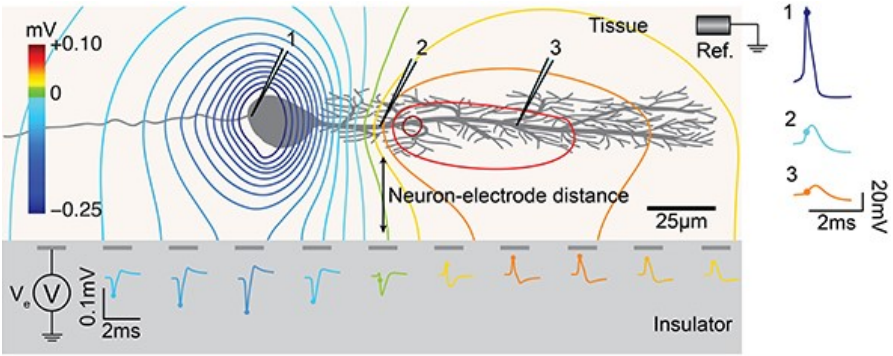

Figure 1.5: Recording waveform variability based on electrode-neuron interface. the amplitude of the recorded extracellular waveform decreases for electrodes distant from the neuron soma and axon initial segment. Also the shape and the polarity of the waveform changes depending on the neuron-electrode interface. Extracellular waveform differs and its amplitude is reduced compared to intracellular recording waveform (1). Adapted from [22].

be modelled as a sheet resistance. With this assumption, the cleft voltage (V_j), the voltage recorded by the electrode, can be computed. Using this model, it is possible to estimate the recorded action potential amplitude and waveform. Extracellular AP amplitude is significantly smaller than the intracellular one, respectively ~1-5 mVpp (peak to peak Voltage) instead of 100 mVpp. Extracellular and intracellular waveforms also differ, as the first resembles the first time-derivative of the second (Figure 1.5).

Cleft properties strongly depend on the tissue electrode interface. Signals recorded with MEAs can be therefore different from the ideal solution represented here. In case of CMOS MEAs where the electrode density reaches a subcellular resolution, due to neuron-electrode distance, the AP from the same neuron but recorded by different electrodes will have different waveforms. The amplitude decay of the signal is correlated with distance from the current source. An example of this concept is shown in Figure 1.5.

MEAS' SIGNALS ANALYSIS MEAs can record hundreds of cells, with a single neuronal AP detected by several electrodes. Conversely a single electrode may record APs from multiple neurons. For this reason, signals need to be processed to extract single neurons activity and position.
MEA data analysis pipeline can be divided in three major steps: filtering, spike detection and spike sorting. Raw electrode signal is band-pass filtered in spikes frequency range (300/500-3000/4000 Hz), to remove artefact and noise. From the filtered signal it is possible to detect spikes. The most common approach is by amplitude threshold crossing [28] (applied in Chapter 4). Finally, the spike sorting step allows to assign spikes to single neurons. The general idea of spike sorting is to use the spike waveform as a fingerprint to identify a cell. For low density MEA, where activity of one cell is detected only by one electrode, it is possible to cluster spikes using principal component analysis (PCA) [29] (applied in Chapter 2). For high density MEAs, spike sorting is much more complex and requires high computational power. For standard spike sorting approaches computational time exponentially increases with the number of channels and recording duration. To reduce sorting time, different sorting algorithms have been proposed, but with the risk of affecting sorting accuracy [30]. For example, one promising approach is the use of template matching methods [31]. For the data presented in Chapter 4 a method based on convolutive independent component analysis was used [32].

ELECTRICAL STIMULATION MEAs are often combined with other devices to study the response of retina to optical, electrical and optogenetic stimulations. Electrically stimulating the retina tissue while simultaneously recording RGC activity adds two main experimental challenges. The first one is the stimulation artifact. Voltages and currents amplitudes used for

stimulating the nervous tissue are usually much larger then the signals recorded by the MEA electrodes. As a consequence, during the stimulation and for a period of time after it, the signal recorded by the electrodes is saturated or distorted making it impossible to detect neuronal activity. The second challenge is to replicate implantation conditions while simultaneously recording and stimulating a large population of retinas' cells and maintaining as many as possible degrees of freedom in the stimulation spatial and temporal pattern. In section 1.3 we show how advances in MEA technology and especially the use of FLEX and CMOS MEA can provide a solution to these challenges.

CMOS design introduces a second advantage to passive electrodes. For passive MEAs the electrode-electrolyte interface is partially capacitive due to the double layer capacitance and partially faradic due the redox reaction between the conductive material of the electrode and the electrolyte. CMOS MEA can instead be designed to have a purely capacitive electrical stimulation, by introducing an insulator layer (dielectric material) at the electrode-electrolyte interface. Faradic electrodes can reach higher charge density, however faradic currents may be associated with the production of compounds toxic for the biological tissue. The insulating layer blocks unwanted reaction, but also limits the charge delivery, possibly preventing effective stimulation of the tissue. Reducing the insulator layer thickness and using material with high dielectric constants, is possible to mitigate this effect. In the CMOS MEA used in Chapter 3, the deposition of the insulating layer was omitted to rely exclusively on the native oxide layer increasing the capacitance of the electrode and the maximal charge density of stimulation.

1.2 PHOTORECEPTOR DEGENERATED RETINA AND VISION RESTORATION

Retina degeneration encompasses several retinal pathologies, in which, due to genetic, traumatic, or environmental reasons, there is a progressive loss of photoreceptor. Photoreceptors degeneration gradually impairs the ability of the retina to detect visual input, eventually leading to blindness. The two main pathologies associated with photoreceptor degeneration are retinitis pigmentosa (RP) and age-related macular degeneration (AMD). RP is an inherited disorder roughly affecting 1 in 4000 people [33], involving a large number of genes [34]. RP initially affects mainly rods. However even if not directly affected by mutation in late stage of the disease also cones die, causing complete visual loss. AMD is a much more common pathology, affecting millions of people, especially elderly [35–37]. AMD causes the loss of photoreceptors in the macula, impairing high acuity vision. It generally does not lead to total blindness, because of some remaining peripheral vision. Therefore, a possible treatment with retina implant is suggested only in the most severe cases. In later stages of the disease, degeneration not only affects the outer retina layer but causes a remodeling of the inner retina network. The retina network, lacking the input from photoreceptors and the healthy physiological environment, undergoes several changes. The effect of these changes is reflected in the activity of bipolar cells and consequently of RGCs, generating an aberrant activity, often in the form of rhythmic waves [38–40]. In the case of retina degeneration, we can identify two stages of the disease and two different clinical approaches. In the early stage of the disease, when the retina is still functional, it is possible to intervene to stop or delay the degeneration in order to preserve the remaining visual perception (Chapter 4). However, in the case of a complete photoreceptors' functionality loss, the

only possible approach is to recreate artificially photo-transduction (Chapter 2 and 3).

1.2.1 *Retina implants*

Until today, the only clinically approved treatments for late-stage retinitis pigmentosa are retinal implants. Retinal implants use electrical stimulation to replace the photoreceptors' function, taking advantage of the activation of the remaining inner retinal neurons. Retina implants using optic sensors, i.e. a camera or a photodiode array, detect visual stimuli and translate changes in luminance into electrical pulses to stimulate the surviving retinal neurons. The response of the retina to electrical stimulation evokes the so-called "phosphene" which is a bright, localized and transient visual percept.

STATE OF THE ART RETINA IMPLANTS Retina implants can be classified in three major categories [5]: epiretinal [41], subretinal [42] and suprachoroidal [43]. Depending on the configuration, the implant is respectively placed in front of the retina, behind it or between the choroid and the sclera (Figure 1.6). To date, three retina implants obtained the approval for clinical application, one epiretinal and two subretinal: the Argus II from Second Sight Medical Products (2011), the ALPHA AMS by Retina Implant AG (2013) and more recently the photovoltaic PRIMA implant from Pixium Vision (2017). The Argus II and ALPHA AMS had respectively 60 and 1600 electrodes and reached visual acuity, in best cases, of 20/1260 and 20/546 [14, 41]. Retina implants provided improvements in patients' life quality, especially in the ability of navigating themself, but far away from the original target of sight restoration and still under the level of legal blindness of 20/200. An *in vitro* study of electrical stimulation with an ALPHA AMS chip

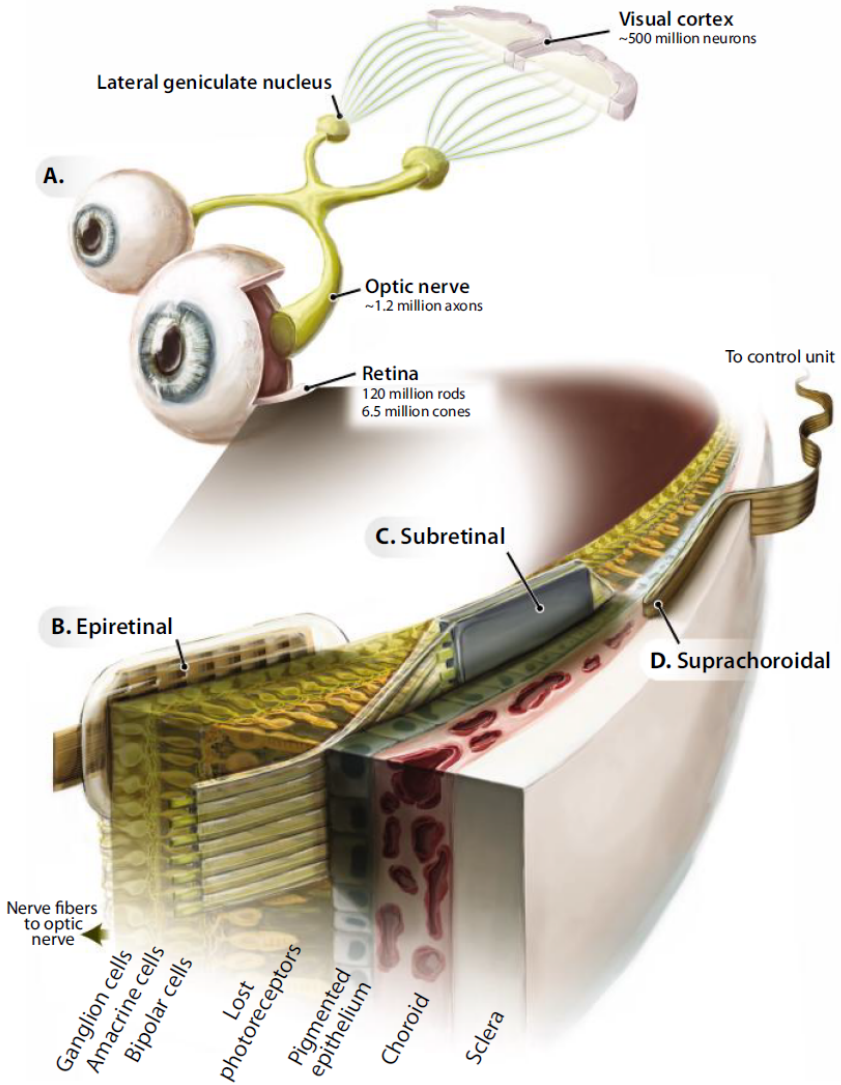

Figure 1.6: Different types of retina implants. Retina implants can be classified in three main categories based on the implantation position of the stimulating array: epiretinal, subretinal and suprachoroidal. In epiretinal configuration the array is placed inside the eye cavity in contact with the RGC layer (B). In subretinal configuration, the array is implanted between the retina and the epithelium, in contact with the photoreceptors layer (C) . In suprachoroidal configuration, it is placed between the choroid and the sclera (D). Credits: [5].

is shown in Chapter 2.

Devices' design is critical to create long-term stability. One of the major issues of the first generation of implants was power delivery and interaction with the electrode array inside the eye cavity. A cable connecting the implant inside the eye with an external support, represents a major engineering challenge, especially considering that the eye performs continuous saccades and microsaccades movements. To overcome this limitation photovoltaic devices have been proposed. Natural light intensity is too weak to activate miniaturized photovoltaic electrodes able to stimulate the retina. Hence, photovoltaic devices use external light sources to deliver power and activate the electrodes. The PRIMA implant [42], now under clinical trial, is an example of this technology. Results are promising, and possibly an improvement on the previous standard, but research is still partial, and the implant is for now exclusively for AMD patients. Another major issue of current implants is the limited field of view, usually restricted to the fovea or macula. A promising solution is the polymeric foldable photovoltaic implant, POLYRETINA [44]. The device, made of flexible materials, can be folded and injected inside the eye cavity, where returning to its original shape, creates contact with the retina. This procedure avoids complex surgical operation, and allows to implant an array of larger dimensions, covering the majority of the field of view. Development of the devices is still undergoing, and information regarding visual acuity are still missing. Other laboratories have proposed to not use a solid array to deliver stimulation, but a "liquid" prosthetics composed of photoactive nanoparticles [45]. The particles could be injected in the subretinal spaces to replace photoreceptors, solving several of the surgical and medical issues of standard devices. Proof of principle studies have been conducted on animals, however applications to humans are still distant.

OPTIMAL STIMULATION STRATEGIES Long term stability, simplicity of implantation, field of view, are critical for implant development. However, improving the degree of vision restoration still remains the main task of retina implant development, and it strictly depends on stimulation efficacy. To this regard retina implant can be characterized by four main parameters: spatial and temporal resolution, contrast, and stimulation threshold. In addition, intensive effort has been carried out to achieve cell type specificity, in order to restore some features of the retina processing.

Spatial resolution is the limit of spatial selectivity of the electrical stimuli and directly affects artificial vision acuity. It is determined by electrode sizes and densities, position of the ground electrode and electrode design but also by stimulation strategies and mechanisms. A strong limitation factor for spatial resolution of retina implants is axonal stimulation. RGC axons run across the retina to gather in the optic nerve. Localized stimulation of RGCs can activate axons of distant neurons, causing misleading precepts for the patient, in the form of halo shapes. Avoidance of axonal stimulation is crucial to obtain optimal spatial resolution by the retina implant.

Temporal resolution and cell type specificity are strongly influenced by stimulation mechanisms. Retina stimulation is called "direct" when RGCs are activated without influencing the other retinal neurons, or "network mediated" when bipolar cells, amacrine cells and photoreceptors are modulated, which in turn activate RGCs. Direct activation aims to elicit a defined spiking pattern in RGCs to possibly mimic visual response, and temporal resolution is the frequency limit at which it is possible to evoke reliable response. Network mediated approaches instead rely on the survival retina network pathways to preserve some of the features of visual response, temporal resolution is therefore defined by the timing of firing patterns generated by the stimulated network. In both cases temporal resolution is limited by

fading, that prevents generating continuous and reliable response at high frequency. Cell type specificity refers to the ability to selectively activate RF classes of RGC, for example a stimulus able to selectively activate ON RGCs. Network mediated approaches, that elaborates the signal exploiting the remaining RF networks, seem to be more suited to achieve cell type specificity compared to direct activation. However, until now no definitive cell specific stimulation strategy has been proposed, representing one of the major limitations to artificial vision.

Contrast detection refers to the ability to discriminate different light intensities by the retina.

Finally, the stimulation threshold indicates the integrated stimulation current, which is needed to reliably stimulate retinal neurons. This parameter should be as low as possible to stay within the safety limit for tissue or electrode damage, and to reduce the power needed to operate the implant.

To achieve optimal performance two strategies can be pursued. One is electrode design, the other is to optimize the stimulation strategy. Several laboratories carried out intensive work to optimize the first. For example, the effect of local returns electrodes has been investigated, demonstrating that it provides a more localized electric field, with the effect of improving spatial selectivity [46]. 3D electrodes also demonstrate to support higher spatial resolution, improving localization of the electric field and contact with the tissue [47–49]. In terms of stimulation, over the years the main strategy, using square-shaped electrical pulses, remained unchanged. Despite the progress in the field to optimize stimulus parameters, i.e. pulse duration, polarity, frequency and amplitude, pulsatile stimulation still lacks to achieve optimal performances. The use of sinusoidal stimulation waveforms is an alternative to pulsatile stimulation. Efficient sinusoidal stimulation at different frequency has been proven with patch clamp, also demonstrating

some degree of phase and frequency dependent cell type selectivity and avoidance of axonal stimulation [50, 51]. The possibility to avoid axonal stimulation was confirmed in a different study with calcium imaging, also demonstrating spatial selectivity and lower threshold compared to pulsatile stimulation [52]. However, the degree of spatial discrimination has not been reported, and the stimulation mechanism, direct vs network activation, never been fully clarified. A in deep analysis of sinusoidal stimulation will be proposed in Chapter 3.

1.2.2 *Vision restoration strategies beyond retinal implants*

Beyond retina prosthetics there a series of other promising approaches to treat retinitis pigmentosa [53]: gene therapy [54, 55], stem cell transplantation [56], chemical [57] and transcorneal electrical stimulation [58] and optogenetic stimulation [16].

OPTOGENETIC STIMULATION In case of a complete loss of photoreceptor functionality a promising alternative to retina implant is optogenetic. Optogenetic consists of inducing the expression of an artificial photo-sensitive ion channel (opsins) in the neuron membrane using a viral vector. This method allows to use light instead of electricity to stimulate the neuron. Natural light does not have the power to activate opsin therefore requiring artificial light sources. In this context, an optogenetic approach does not refer to a restoration of retina's photosensitivity, but instead to the use of an alternative stimulation mechanism. Optogenetic, differently to electrical stimulation, does not necessitate a chronic eye implant for the stimulation of retina but capitalizes on the natural optics of the eye. The main advantage of an optogenetic approach is the possibility to use cell specific viral vectors. It

has been proven that opsins can be expressed in photoreceptors, bipolar cells and RGCs, but most importantly in subclasses of bipolar cells, with the possibility to recruit specific information pathways. However, genetic therapies, especially in humans, still present technological challenges. Indeed, specific activation can be denied by retina degeneration. Furthermore, we must bear in mind ethical considerations, before optogenetic can be considered as an alternative to electrical stimulation as it is imperative to establish safe, reliable and effective methods and protocols.

VISION PRESERVATION In case of early intervention, when it is still possible to stop retinal degeneration before complete vision loss, gene therapy proved to be a powerful solution. However, while gene therapy is the ideal solution for specific pathologies, RP and AMD are multi-genetic disorders and gene therapy can target only one or few dysfunctional genes.
Retina degeneration, depending on the pathology, can occur in both young and elderly. In both cases, to avoid invasive surgery and implantation, preserving the remaining vision at the moment of diagnosis is crucial. Even in case of prosthetic implantation, preserving the retina network stays critical to exploit inner retina functionality, and to prevent aberrant activity. For this reason, several drug compounds have been tested to improve photoreceptor survival in degenerated retinas. Between these a promising group are histone deacetylases (HDAC) inhibitors. Protein deacetylation by HDACs, together with protein acetylation by histone acetyltransferases, strongly affect regulation of cellular activity, and it is involved in several diseases [59]. The role of HDAC inhibitors were first investigated in studies on retinal ischemia in degenerative diseases [60]. HDAC affects several processes of retina developments, and it has been proven that HDAC affects primary photoreceptors' death in retina degeneration [61–64]. For this reason, HDAC

inhibitors have been considered as a possible treatment for secondary cone cell death in retina degeneration. A detailed work on the effect of HDAC inhibition on retina anatomy and functionality is shown in Chapter 4.

The development of new solutions for vision restoration must go side by side with the development of laboratory and *ex vivo* techniques to provide a better platform to develop new stimulation strategies. An ideal system must be able to simultaneously record and stimulate a large population of the retinal neural network, with high spatial and temporal resolution. Therefore, before describing and discussing the main results of my work on electrical stimulation, in this section, latest advances in MEA technology and how I applied them to my studies on artificial vision will be illustrated.

1.3.1 *Flexible microelectrode array for in vitro assessment of subretinal stimulation*

In the framework of subretinal implants, to develop stimulation strategies *in vitro*, a system able to stimulate the retina tissue from the photoreceptor side while recording the RGCs activity is required. This can be achieved by combining one stimulation electrode with a recording patch clamp pipette or with MEA extracellular recordings [65–67]. Alternatives include stimulation with single electrodes and optical recording of evoked activity [57] or using a MEA as a stimulation array and recording the response with patch clamp electrodes [68]. Although these approaches provided valuable results they are often limited to one or few electrodes for stimulation or recording, or they lack the time resolution to resolve single spikes. Using a single electrode for stimulation does not allow the use of complex stimulation patterns, or to test the RGCs response to different stimulation areas. While using patch clamp for recording limits the number of recorded cells preventing access to the RGCs population activity and significantly increasing the experimental time required to collect a large number of cell responses.

A combination of two microelectrode arrays can be used to increase the number of stimulation electrodes, while simultaneously recording activity of multiple RGCs'. This has been achieved and published by the Zeck lab in 2016 and by the Palanker lab in 2018 [40, 69]. The Palanker group used a photovoltaic implant in combination with a rigid, glass-based MEA, exploiting the possibility of wirelessly powering the implant with light. While a wireless approach provides greater advantages in *in vivo* application, a photovoltaic implant does not provide the possibility to apply different stimulus waveforms, limiting its application in the studies of stimulation strategy. The solution developed by Stutzki et al. instead uses a flexible MEA placed on the epiretinal side as a readout of RGCs' activity (Figure 1.7). The FLEX MEA can be combined with any type of planar MEA in subretinal configuration for stimulation. The system allows flexibility on the stimulation waveform and spatial patterns while recording multiple RGC. In Chapter 2 I present a work where I used this configuration to characterize stimulation with the ALPHA AMS retina implant chip. I was able to stimulate the interfaced retina using an arbitrary selection of the 1600 stimulation electrodes (30 µm diameter) and record with up to 32 electrodes of the FLEX MEA. Each electrode of the implant is coupled to a photodiode that controls its stimulation charge. When light hits the photodiode, the implants translate the light into stimulation current, adjusting current amplitude proportionally to the light intensity. The FLEX MEA is made of transparent polymerics material (polyimide). This allows to activate the implant using light, mimicking as close as possible the implantation conditions. The system was used to investigate threshold charge density for subretinal stimulation and the stimulus response relationships for square pulse stimulation. The possibility to select the number of channels for stimulation allowed us to determine the

dependency of charge threshold on electrode size. Results using this study are presented in the section 1.4 and in detail in Chapter 2.

1.3.2 *Epiretinal configuration: high density CMOS MEA, a truly bidirectional neural interface*

STIMULATION ARTEFACT The first requirement to evaluate various electrical stimulation protocols is the simultaneous recording and stimulation without stimulation artefact. Electrical stimulation creates a distortion on the recorded voltage signal [22]. It is possible, with signal processing and artefact removal algorithms, to reduce this effect. However, the artefact is usually too strong to be completely removed, resulting in a post-stimulus time window in which it is impossible to detect spikes. One solution is to optimize stimulation waveform, phase and polarity to reduce artifacts [70]. However, to find the optimal stimulation strategy for retina implants the stimulation parameters are selected based on the spatio-temporal neuronal activation patterns, with the risk that optimal parameters to activate the RGC differs from the optimal parameter to avoid artefact.

Common stimulation approaches use square pulses stimulation. The high frequency components of square pulses generate artefacts which are in the frequency ranges of the neuronal spikes (~1kHz). Smooth wave stimulation instead generates artefact that can be more easily removed in post-processing steps. In Chapter 3 I used a high-density CMOS MEA with separated electronics for stimulation and recording and the possibility to choose any arbitrary stimulation waveform [71, 72]. Combining these features, I was able to investigate the effect of continuous sinusoidal stimulation on RGC activity without artefact at subcellular resolution, recording from all the 4225 channels of the CMOS MEA. Smooth wave or sinusoidal stimulation, which

does not generate significant artifacts, can be an alternative in applications outside of artificial vision.

STIMULATION AND RECORDING SPATIAL RESOLUTION Artificial visual acuity depends on the spatial resolution of the stimulation and is therefore limited by the implant's electrode size and pitch. Intensive work has been done to reduce the electrode's dimension and evaluate the retina response to micrometric electrode stimulation. For subretinal configuration, in Chapter 2 I proved and published for the first-time stimulation of photoreceptor-degenerated mouse retina with a single 30 µm electrode within safety limits. More recently other groups reported results with subretinal photovoltaic 10 µm electrodes with 55 and 40 µm pixel size [47], but they did not provide single electrode stimulation results. Successful stimulation of chicken retina using one single 10 µm electrode had been reported in 2000 [67].

In epiretinal configuration, delivering electrical stimulation while simultaneously recording adds an additional challenge, as stimulation and recording are both performed from the RGC side and usually with the same array. This requires that stimulation and recording electrodes are in close proximity or that some of the recording electrodes are used to deliver stimulation, limiting stimulus duration, the number of stimulation electrodes or the number of recorded RGCs. Neuronal networks, and retina encode information at population level [73]. Therefore, an optimal system should not only be able to stimulate the network with micrometric electrodes but also to simultaneously record the largest possible portion of the targeted network, ideally the full population involved. Stimulation with a small electrodes (10 µm diameter / 60 µm pitch) array has been shown, with the possibility of axonal tracking, but limited in stimulus duration or the stimulation electrode number [46]. A

CMOS MEA ($5 * 9$ μm^2 electrodes and a pitch of 17,5 µm) has been used by the Hierlemann lab for electrical stimulation of neuronal cell cultures, but not in retina application [70]. CMOS technology is used to increase electrode number and density, but it also allows to include in the same chip a stimulation and a recording array. In the CMOS MEA used in Chapter 3, a 4225 electrodes recording array (16 µm electrode pitch) is combined with a 1024 electrodes stimulation array (32 µm electrode pitch; stimulation electrode area: 632 μm^2) (Figure 1.7). I was able to simultaneously record, localize and stimulate hundreds of cells from a single retina sample in an area of one square millimeter. The system also allows to randomly select any of the stimulation electrodes, and to use any arbitrary stimulation waveform, providing a truly bidirectional interface with the tissue. I used this setup to test RGC responses to different electrode sizes and discrimination of spatial jitter and contrast level by stimulation with simple small shapes.

RECORDING SPATIAL RESOLUTION - AXONAL LOCALIZATION In the field of retina implant development great importance is given to the possibility to detect and localize axons. Axonal stimulation limits the spatial resolution of electrical implants and creates distorted visual percepts in patients. However, to reliably test axonal stimulation a system able to record and analyze axonal signals is required. This can be achieved with calcium imaging [52] . However, due to the limited temporal resolution of the technique, axonal stimulation could remain undetected. A more reliable solution is the use of high density MEAs [74, 75]. Axonal signals are generally too small to be detected using a single spike. It is possible however to apply spike triggered average (STA) methods, to reduce noise level and determine the axon location and propagation velocity. This has been shown by Grosberg et al in 2017 in the context of retina prosthetics, evaluating axonal activation

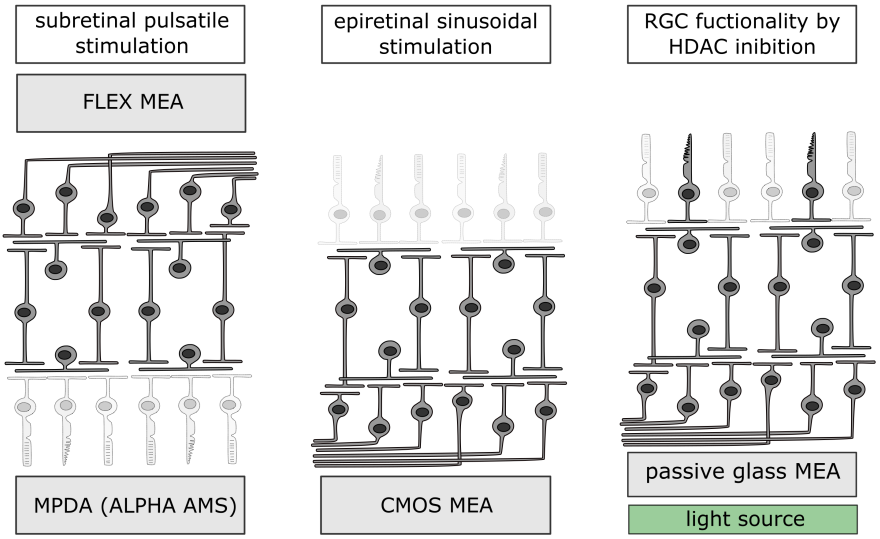

Figure 1.7: Different MEAs types and how they were applied in this work to study vision restoration. In Chapter 2 I used a FLEX MEA in combination with the retina implant ALPHA AMS to investigate subretinal electrical stimulation. In Chapter 3 with a HD CMOS MEA I characterize sinusoidal epiretinal stimulation. In Chapter 4 I used a passive MEA to test light responsiveness of treated *rd10* retina to determined efficacy of HDAC inhibitor as treatment to delay retina degeneration.

by single, small electrodes (10 µm diameter) [76]. The STA approach was applied to recording performed using the CMOS MEA described above to study axonal stimulation in sinusoidal epiretinal stimulation for various electrode sizes (Chapter 3).

1.4 PERFORMANCE OF RETINAL PROSTHETIC STIMULATION

Performance of electrical stimulation can be described by the spatial and temporal resolution of the stimulation, and by the ability to encode contrast sensitivity. In addition, charge threshold and (avoidance of) axonal stimulation must be taken in account. In Chapter 2, I evaluated these parameters for subretinal configuration with pulsatile stimulation, the most common strategy applied for retina implants. In Chapter 3, I tested epiretinal configuration with sinusoidal stimulation, as a new possible stimulation strategy. Here I summarize the results of these studies and discuss how they can be used to develop the optimal stimulation strategy for retina implants.

1.4.1 *Threshold charge density*

SUBRETINAL CONFIGURATION To improve spatial resolution of retina implant electrode size must be reduced thereby increasing electrode density. However, electrodes with a small surface area require higher charge density to effectively stimulate neurons with the risk of exceeding safety limits for tissue and electrode damage. In the work presented in Chapter 2, I evaluated the threshold charge density in photoreceptor-degenerated retina upon stimulation with individual small electrodes in subretinal configuration. I stimulated *ex vivo rd10* retina, using a single electrode (30 µm diameter, material: Iridium oxide) of the retina implant ALPHA AMS. I evaluated the stimulus response relationship of the activated RGCs firing rate, to extract the charge threshold for reliable stimulation. The threshold charge densities I obtained ranged between 100-900 $\mu C/cm^2$ for a single electrode, below the reported safety limits for iridium oxide and tissue damage. The results were mostly in line with earlier studies (table 2, Chapter 2), which were

performed on healthy retina. The large charge threshold variability reported here can be attributed to the different physical distance between electrode and stimulated cells.

More recent works indicated that lower charge threshold could be achieved by using 3D electrodes with local return. They demonstrated successful stimulation using 10∗14 µm pillars in 55 µm pixels electrodes in a photovoltaic implant [47]. The charge threshold in the study was presented as the irradiance level to activate the implant and not as current intensity, making it difficult to compare it with our result. Another theoretical study from the same group, showed how a 3D honeycomb structure could reduce the charge threshold for small electrodes [49]. For planar electrodes, charge thresholds rapidly increase reaching cellular dimension. The honeycomb 3D structure with local returns penetrates in the retina improving the electrode neuron interface and electrode field localization, reducing the charge threshold. The theoretical reported charge threshold for 20 µm pixel is 280 $\mu C/cm^2$ (10 ms pulse) for 3D honeycomb electrode, while it would exceed the safety limit for planar electrodes (9400 $\mu C/cm^2$). The results reported here are theoretical, and it is not completely clear how it will apply to *in vitro* and *in vivo* conditions. However, they suggest that for subretinal stimulation, using 3D structure and localized returns could be a possible solution to reduce electrode dimension.

Finally, to understand the threshold dependency with electrode size I evaluated the charge threshold for larger stimulation electrode areas. The threshold charge density for subretinal stimulation initially decreases and reaches saturation for electrode diameter larger than 300 µm. My results are in line with previous works by Stutzki et al. and Ho et al., demonstrating that the electric receptive field size (e-RFs) matches the visual equivalent [40, 47].

EPIRETINAL CONFIGURATION Network mediated activation is usually the major component driving RGCs activity upon subretinal stimulation. In epiretinal configuration both network mediated and direct activation are possible [68]. For network-mediated spikes in the healthy retina threshold charge densities for epiretinal and for subretinal configuration are in the same range. In the study on sinusoidal stimulation I found exclusively direct RGC activation in photoreceptor-degenerated retina whereas in wild-type retina the same sinusoidal stimulus activated the network as well (supplementary figure, Chapter 3). The estimated threshold charge density of 4 $\mu C/cm^2$ is about twenty times smaller than the previously reported for epiretinal pulsatile stimuli using electrodes of similar size and it is about ten times smaller than charge densities evaluated for subretinal pulsatile stimuli (reviewed in Chapter 2) [77]. For stimulation areas larger than 0,011 mm^2 the charge threshold remained constant. For small stimulation areas of 0,001 mm^2 instead the average charge threshold was 80 ± 40 $\mu C/cm^2$. While for even small electrode sizes, it was not possible to reach the threshold due to the limited max charge density provided by the electrode used in this study. However, this suggests that for smaller electrode size the charge threshold further increases. My findings show that direct activation charge threshold does not correlate with the v-RF size as expected for the stimulation mechanism and differently than for network mediated activation. However, it increases when the electrode size reaches cellular dimension, with the risk of exceeding safety limits [49, 78]. Our findings suggest that sinusoidal approach could be the solution to further miniaturize stimulation electrodes for epiretinal stimulation. Further studies are required to determine sinusoidal charge threshold for small (<0,011 mm^2) electrode sizes.

NON-MONOTONIC STIMULUS RESPONSE RELATION IN SUBRETINAL CONFIGURATION The recruitment of the retinal network affects the RGC's stimulus response relationship (SRRs). Traditional theory of electrical stimulation of neuronal tissue assumes that for increasing stimulation strength the evoked activity follows a sigmoidal function, with the firing rate saturating for high stimulation intensity [77]. However, non-monotonic stimulus SSRs were shown recently by us (Chapter 2) and by others [79, 80]. Non-monotonic SSRs have been referred to the activation of inhibitory retinal circuitry which suppress the activity of ganglion cells [81]. For epiretinal direct sinusoidal stimulation (Chapter 3), as expected for the different stimulation mechanism, non-monotonic SSRs were not detected.

In conclusion, both subretinal network mediated activation and epiretinal sinusoidal stimulation show a dependency of electrode size with threshold charge density. However the two differ based on the activation mechanism. For subretinal network mediated activation, the threshold decreases up to the size of the RGC electrical receptive field. While, for epiretinal sinusoidal stimulation the threshold charge density decreases up to an electrode size equivalent to the RGC size. New retina implants should implement mechanisms to adjust the electrode stimulation charge according to the electrode size and to the number of simultaneously stimulating adjacent electrodes. The concept is more emphasized in case of network mediate response in order to avoid non-monotonic responses and especially in clinical application where the calibration of stimulation parameters is more challenging, due to the implant-tissue contact variability.

1.4.2 *Spatial resolution*

The stimulation mechanism, network mediated or direct, has a strong impact in the strategy used to achieve high visual acuity. Generally, subretinal implants act via network mediated activation, while epiretinal via direct RGC stimulation. However, very often the two mechanisms are concurrent. Solutions have been developed to have exclusively network mediated responses [52, 82] or exclusively direct activation in epiretinal configuration using short pulses [83]. I reported an exclusively direct mechanism for sinusoidal epiretinal stimulation in rd10 retinas (Chapter 3).

NETWORK MEDIATED ACTIVATION Network mediated stimulation is thought to rely on the natural retina processing. Similarities between electrical receptive field (e-RF) and visual receptive field (v-RFs) size has been shown by Stutzki et al. and by me using the subretinal ALPHA AMS retina implant [40, 78] (Chapter 2). A similar study conducted using the subretinal PRIMA implant showed concordant results, also demonstrating antagonistic center-surround organization [69]. In the study presented in Chapter 2, using the ALPHA AMS implant I proved stimulation using a single 30 µmum electrode in an array with a 70 µm pitch which results in a theoretical visual acuity of 20/280 [14]. However, results from patients wearing this device indicated the best (one patient) achieved visual acuity of 20/546 while other patients reached values below 20/1260 [41]. One possible explanation of discrepancy between theoretical and patient results, is the mono-polar design of the return electrode of the implant, that causes spreading of the electric field. It has been shown how local return can improve spatial selectivity [46]. A more recent implant (PRIMA implant) implemented photovoltaic electrodes with local return electrodes. *In vivo* test of the implant measuring VEP in

rats, reported a resolution of 48 ± 11 µm to grating stimuli, corresponding to a theoretical acuity of 20/192 [47]. Results from clinical trials with a similar array with 100 µm pixels provided visual acuity ranging from 20/460 to 20/800, with an expected acuity of 20/420 [42]. This result further increases the hypothesis that retina can elaborate e-RFs in a similar way to the v-RFs, and the retina processing can be used to achieve high acuity vision. Further investigation is required to understand discrepancy between theoretical and experimental findings. One main contribution is probably the quality of the implant placing and therefore the implant-tissue interface. However other factors, such as stimulation mechanism, network processing and the degree of retina degeneration must be taken in account and further investigated.

DIRECT RGC STIMULATION Differently to network mediated stimulation, direct activation cannot rely on the available retinal processing, and spatial resolution strictly depends on the size of the stimulation activation. From the response of more than a thousand RGCS, I estimated the radius of activation with gaussian fitting for two stimulation electrode sizes, respectively 0,011 and 0,022 mm^2. Activation radii were 57.4 ± 3.3 µm and 81,6 ± 3,4 µm matching the equivalent electrode radius (56,7 µm and 85 µm). This result proves that sinusoidal stimulation is localized and only RGCs located directly above the electrodes are activated (Figure 3, Chapter 3). Previous studies on retina implants, reported that patients have difficulties in detecting small objects and shapes [41, 84] . Therefore, spatial resolution was tested as degree of discrimination between spatially displaced small object (details in Chapter 3). The stimulation protocol consisted in two identical stimuli displaced by a small spatial jitter (32, 64 and 128 µm). The accuracy in discriminating the two stimuli was tested using a logistic regression model. Two electrode sizes were tested: 0,011 and 0,022 mm^2. For the larger area

it was possible to discriminate jitter of 32 µm, while for the smaller 64 µm jitter. The results of 32 µm exceed the best reported spatial resolution for electrical stimulation of the retina [47]. Based on the estimation of theoretical visual acuity from *ex vivo* rodent spatial resolution proposed by Goetz and Palanker [14], 32 µm spatial resolution will correspond to a visual acuity of 20/130, above the limit of legal blindness (Figure 4, Chapter 3).

AVOIDANCE OF AXONAL STIMULATION Avoidance of axonal stimulation is crucial to achieve high spatial resolution. In subretinal configuration, confined and localized stimulation of the inner nuclear layers should avoid axonal stimulation. In epiretinal configuration, with axons running along the RGCs layer the problem is more challenging [76, 85, 86]. Avoidance of axonal stimulation has been demonstrated by using long stimulation pulses with calcium imaging [52]. However, due to lower resolution of the recording technique axonal stimulation could have been undetected. I tested axonal stimulation for sinusoidal stimulation with a HD CMOS MEA enabling axon tracking. I calculate cell activation for the RGCs with axons passing over stimulation electrodes. Axonal activation was not detected for the dataset tested (83 cells for a 0,011 mm^2 stimulation area and 74 cells for 0,022 mm^2) (fupplementary figure, Chapter 2).

In the experiment shown here, I applied stimuli with very low amplitudes. It is possible that the reason for avoidance of axonal stimulation relies on the low stimulation intensity. Further tests must be done to understand if axonal stimulation is present for epiretinal sinusoidal stimulation for higher charge density or larger electrode size. However, my results show a strategy for reliable RGCs activation, without axonal stimulation.

1.4.3 *Contrast discrimination*

Contrast discrimination in artificial vision is limited to few grey levels [41, 87]. Goetz et al. compared normal vision and artificial contrast discrimination upon stimulation with a subretinal photovoltaic chip [88] . To evoke a significant increase in RGC activity or in the cortex, with a photovoltaic subretinal chip, positive contrast steps larger than 50% in Michelson units were required, compared to only a few percent required with normal vision. While negative contrast steps did not evoke any change in activity. Subtle differences in the temporal spiking patterns have been inferred at lower contrast levels (12%) by Ho et al. The study highlights the importance of spike pattern for contrast threshold, in contrast to simple changes in the average RGC spiking rate. In Chapter 3, a logistic regression model was used to determine the discrimination accuracy for stimuli with different artificial contrast. Fiive object sizes were tested (between 0,005 and 0,1 mm^2) at different contrast levels. Contrast was created by stimulating with two adjacent electrode areas with different current density. Accuracy was tested in a pairwise fashion, discriminating between contrast levels and contrast 0%. For large stimulation areas it was possible to discriminate with high accuracy (0,8) 10% artificial contrast, in line with the prediction by Ho et al. for subretinal configuration [69].

1.4.4 *Temporal resolution and cell type selectivity*

To restore high degree vision, the visual cortex must be able to interpret the firing pattern evoked by electrical stimulation in the retina. Neuronal network plasticity usually allows the brain to learn and recognize new patterns. However, results from patients wearing a retina implant did not

show any improvement or learning over time [84]. This could suggest that artificial visual responses differ too much from healthy visual responses to be recognized by the brain. This deficit could arise from two main limitations of current approaches in artificial vision. First, a poor temporal resolution. Second, the lack of cell type specificity, i.e the impossibility to selectively activate ON and OFF pathway.

NETWORK MEDIATED ACTIVATION Temporal resolution commonly refers to the maximum stimulation frequency able to evoke reliable responses and it is limited by fading of the evoked percept [20, 89, 90]. However, as it is show in Chapter 2, for network mediated activation a single millisecond pulse activates a response that can last up to hundred milliseconds. Generally network mediate response is composed by short latency spike or burst generated by the direct activation of RGCs, a delayed response evoked bipolar cell stimulation and in case of healthy retina a late photoreceptor response [68]. For this reason the concept of temporal resolution for network mediated activation can be extended to the ability to generate spike patterns with a defined temporal timing and not only to the frequency limits of stimulation. Network mediated activation relies on the remaining retina signal pathway to evoke temporal patterns resembling visual response. In addition, It has been shown by different labs that different RGC types respond with different spike patterns to electrical stimulation. Im et al. have reported correlation between some features of the electric and visual response spiking patterns of ON cells, while the same correlation was not detected for OFF cell response [91]. Other groups, using a STA approach to calculate the e-RF of RGCs, reported a correspondence between ON and OFF response and stimulus polarity, also showing spatial and temporal similarities of the v- and e-RF [69, 79]. Finally, it has been shown how selecting the optimal

parameter to maximize the difference between cell types response could be a strategy to obtain selective activation [19, 92]. These results prove that the retina network is affecting the RGCs response. However, the real degree of correlation between electrical and visual response is not fully understood yet. In Chapter 2, I also tested visual and electrical response of ON and OFF cells. Even if I did not perform in depth analysis on this subject, I could confirm cell type response differences. However a clear difference was observed between visual and electrical evoked spiking patterns. It must be noted that these studies are performed with healthy retinas and photoreceptors play an important role in the network mediated response [69]. In addition it has been proved that retina degeneration affects electrical response [93]. Heterogeneous responses have been demonstrated also in degenerated retinas [40, 69], but, due to the lack of visual response, it was not possible to correlate electric response with cell type. Comparing visual and degenerated retina electrical stimulation response in the same retina is hardly possible. Future work is necessary to try to merge this gap. In this context, treatment to preserve retina functionality could gain more importance not only as a preventive solution to retina degeneration, but also as a complementary therapy to retina implant. An example of this type of treatment is discussed later in section 1.5 and shown in detail in Chapter 4.

DIRECT RGC STIMULATION Direct activation of RGC activity by one single stimulus type cannot evoke cell type specificity as expected for the network mediated response. Direct stimulation evokes spike trains following a temporal pattern correlated to the intrinsic excitability of the cell [94]. ON and OFF specificity, based on the frequency range of stimulation, was demonstrated with intracellular stimulation. However, this effect has not been detected for extracellular stimulation [95]. Therefore, temporal reso-

lution for direct stimulation relies exclusively on the ability to evoke high frequency precise firing in RGCs [83]. Pulsatile stimulation is limited in the frequency range by fading of the evoked RGC activity, which causes a desensitization of the response [94]. It has been shown in healthy retina that sinusoidal stimulation does not cause fading of the evoked activity and can provide a high degree of correlation between stimulus phase and response [50]. In the work presented in Chapter 3 on adult photoreceptor-degenerated mouse retina I demonstrated continuous sinusoidal stimulation up to 40 Hz with high reliability and no fading providing the tool to evoke precise firing patterns in RGCs.

Retinitis pigmentosa (RP) is a multi-genetic disorder causing rod photoreceptor death. Cone photoreceptors are not affected by mutations, however the non-physiological environment created by rod death affects cones that in turn progressively die. In the early stage of the disease vision is not severely affected, making it difficult for patients and medics to diagnose the pathology. Treatment to delay or prevent cone death are therefore important to preserve the remaining retina functionality and avoid complete vision loss [96]. In addition, In the previous section it is shown how exploiting the retina network is one of the strategies to restore vision via retina implant. Network degeneration can affect retina response to electrical stimulation reducing its efficacy. Therefore, preserving retina functionally could also play an important role as a complementary treatment for retina implant .

Cone death is driven by different factors, such as loss of structural and nutritional support from rods [97, 98], exposure to oxidative stress [99] and inflammation [100, 101]. In RP several different genes are involved in the photoreceptor mutation [34]. It is possible to protect cones epigenetically by regulating the genes involved in cone survival via HDAC inhibition [61–64]. In the collaborative project work presented in Chapter 4, it was first demonstrated an increased HDAC activity in degenerated mouse models (rd1 and d10), and that treatment with HDAC inhibitor Trichostatin A (TSA) afforded long-term preservation of cone photoreceptors.

One crucial aspect I was mainly contributing was to determine the functionality of the rescued cones. I tested the light response of *ex vivo* organotypic retina culture (Figure 1.7). I calculated RGCs response ratio for treated and control organotypic retina cultures. Treated retina showed a significantly stronger response for medium-high light intensities. The results show how

the rescued photoreceptors are functionally connected to the retina network, and RGCs are integrating the signal coming from a larger number of cones suggesting the efficacy of the treatment. Complementary *in vivo* behavioral tests and ERG recording conducted by other partners in the project, supported the thesis that cone survival translated into better visual response of the retina. In rd10, ERG showed improvement following the treatment compared to control. The rd10 treated ERG response however remained lower than in wild-type mice, as expected for a treatment at this stage of degeneration. An additional proof of functionality of rescued cones came from the significant improvement in visually-driven behavior.

Finally my co-authors investigated which genes and molecular pathways were affected by HDAC inhibition. The results suggest that HDAC inhibition induces neuroprotection via activation of MAPK and PI3K-Akt pathways. It is also shown how HDAC inhibition induces increased autophagy in the treated retina, with the additional positive effect in preventing cone starvation and therefore increasing cone protection.

The aim of the thesis was to investigate the efficacy of different treatment and vision restoration strategies in preventing or treating retina degeneration. I tested, in *ex vivo* retina tissue, subretinal pulsatile and epiretinal sinusoidal stimulation as stimulation strategies for retina implant. In addition, I contributed to the assessment of light responsiveness of organotypic retina culture after HDAC inhibition, to assess the efficacy of the treatment. All the studies included in the project applied the use of MEA to record or modulate RGCs' activity. Retina implants even if based on the same operational principle can differ significantly on the stimulation strategy and there is not yet a definitive answer to which is the optimal approach. Subretinal implant allows better tissue-implant interface, and possibly network mediated cell type specific stimulation. Epiretinal implants usually act via direct activation lacking network mediated heterogeneous response and are affected by axonal stimulation. However, they can provide a much easier implantation procedure and much wider field of view.

In the studies included in this work I addressed some of the current issues for both configurations. In subretinal implant, one of the challenges is the miniaturization of the electrodes to achieve higher spatial resolution without exceeding safety limits. I demonstrate, determining the threshold charge density, that stimulation of photoreceptor degenerated mouse retina with a single 30 µm electrode is possible. I also characterized electrode size dependent charge threshold and reported on non-monotonic stimulus-response relations. My results together with other studies indicate that spatial resolution can be further increased for subretinal stimulation, however new implants should implement electrode-size dependent stimulation strategy, i.e. adjusting charge threshold based on the number of adjacent activated

electrodes. For network mediated stimulation approaches, two open questions still need to be addressed. First one is the degree of correlation between visual and electrically evoked response. New studies must be performed to fully understand this topic, and develop experimental procedures to compare healthy visual response and degenerated electrical evoked activity. The second one is the possibility to achieve cell type specific stimulation. In this direction, theoretical models could be a tool to infer cell type specific stimulation waveforms [102].

Epiretinal direct stimulation cannot rely on the retina network processing and cell type selective stimulation seems precluded. The lack of retina network signal processing must be considered when developing the implant design and simulation strategy. One solution is to simplify the features of the visual stimulus to match the level of electrical stimulation information encoding [103]. Another option is to implement closed loop system to tailor the stimulus to the desired response, and develop algorithms to calculate the optimal stimulation parameters [104]. In both cases the stimulation strategy spatial and temporal resolution must be optimized to achieve full control on the spatio-temporal evoked firing patterns. We demonstrated reliable and continuous, without fading, sinusoidal stimulation up to 40 Hz, avoiding axonal stimulation. Using this strategy, we could discriminate with high accuracy spatial displacement of 32 µm and contrast level of 10% upon stimulation with simple shapes, matching and improving current standard. The results presented here and by other groups involved in the field show that future advances in retina implant could finally allow artificial vision to overcome the limit of legal blindness. However, it is also clear that without achievement, such as cell type selective activation, the goal of full sight restoration seems prevented. It is therefore important to develop alternative strategies to preserve retina functionality before implantation is needed. In

the last study included in this dissertation, we show how HDAC inhibition delay and slow done cones death in mouse models of degenerated retina. My main contribution to the work was to prove functionality and light responsiveness of rescued cones. The improved functionality of the treated retina suggests the efficacy of HDAC inhibition as a treatment for retina degeneration.

REFERENCES

[1] Otfrid Foerster. "Beiträge zur Pathophysiologie der Sehbahn und der Sehsphare." In: *Journal für Psychologie und Neurologie* (1929).

[2] G. S Brindley and W. S Lewin. "The sensations produced by electrical stimulation of the visual cortex." In: *The Journal of Physiology* (1968). DOI: https://doi.org/10.1113/jphysiol.1968.sp008519.

[3] James D Weiland, Wentai Liu, and Mark S Humayun. "Retinal Prosthesis." In: *Annual Review of Biomedical Engineering* (2005). DOI: https://doi.org/10.1146/annurev.bioeng.7.060804.100435.

[4] Eberhart Zrenner. "Will retinal implants restore vision?" In: *Science* (2002). DOI: https://doi.org/10.1126/science.1067996.

[5] Eberhart Zrenner. "Fighting Blindness with Microelectronics." In: *Science translational medicine* (2013). DOI: https://doi.org/10.1126/scitranslmed.3007399.

[6] Lan Yue, James D Weiland, Botond Roska, and Mark S Humayun. "Retinal stimulation strategies to restore vision: Fundamentals and systems." In: *Prog Retin Eye Res* (2016). DOI: https://doi.org/10.1016/j.preteyeres.2016.05.002.

[7] Eberhart Zrenner, Alfred Stett, and Reinhard Rubow. "The challenge to meet the expectations of patients, ophthalmologists and public health care systems with current retinal prostheses." In: *Investigative Ophthalmology & Visual Science* (2020).

[8] Melvyn A Goodale and A David Milnerb. "Separate visual pathways for perception and action." In: *Trends in Neuroscience* (1992). DOI: https://doi.org/10.1016/0166-2236(92)90344-8.

[9] Gurdeep S Mannu. "Retinal phototransduction." In: *journaltitle* (2014).

[10] Jose-Manuel Alonso and Yao Chen. "Receptive field." In: *Scholarpedia* (2009). DOI: doi:10.4249/scholarpedia.5393.

[11] Tom Baden, Philipp Berens, Katrin Franke, Matthias Bethge Miroslav Román Rosón, and Thomas Euler. "The functional diversity of retinal ganglion cells in the mouse." In: *Nature* (2016). DOI: https://doi.org/10.1038/nature16468.

[12] Kristin Koch, Judith McLean, MichaelBerry, Peter Sterling, Vijay Balasubramanian, and Michael A Freed. "Efficiency of Information Transmission by Retinal Ganglion Cells." In: *Current Biology* (2004). DOI: https://doi.org/10.1016/j.cub.2004.08.060.

[13] B G Cleland and W R Levick. "Brisk and sluggish concentrically organized ganglion cells in the cat's retina." In: *Jurnal of Physiology* (1974). DOI: https://doi.org/10.1113/jphysiol.1974.sp010617.

[14] Georhes Goetz and Daniel Palanker. "Electronic approaches to restoration of sight." In: *Reports on Progress in Physics* (2016). DOI: https://doi.org/10.1088/0034-4885/79/9/096701.

[15] Eric Kandel, James Schwartz, and Thomas Jessell. "Principles of Neural Science, Fourth Edition." In: (2000).

[16] Sonja Kleinlogel, Christian Vogl, Marcus Jeschke, Jakob Neef, and Tobias Moser. "Emerging Approaches for Restoration of Hearing and Vision." In: *Physiological Reviewes* (2020). DOI: https://doi.org/10.1152/physrev.00035.2019.

[17] Chang-Jin Jeon, Enrica Strettoi, and Richard H Masland. "The Major Cell Populations of the Mouse Retina." In: *Journal of Neuroscience* (1998). DOI: https://doi.org/10.1523/JNEUROSCI.18-21-08936.1998.

[18] Andrew B Watson. "A formula for human retinal ganglion cell receptive field density as a function of visual field location." In: *Journal of Vision* (2014). DOI: https://doi.org/10.1167/14.7.15.

[19] Maesoon Im, Paul Werginz, and Shelley I Fried. "Electric stimulus duration alters network-mediated responses depending on retinal ganglion cell type." In: *Journal of Neural Engineering* (2018). DOI: https://doi.org/10.1088/1741-2552/aaadc1.

[20] Maesoon Im and Shelley I Fried. "Temporal properties of network-mediated responses to repetitive stimuli are dependent upon retinal ganglion cell type." In: *Journal of Neural Engineering* (2016). DOI: https://doi.org/10.1088/1741-2560/13/2/025002.

[21] C A Thomas Jr, P A Springer, G E Loeb, Y Berwald-Netter, and L M Okun. "A miniature microelectrode array to monitor the bioelectric activity of cultured cells." In: *Experimental Cell Research* (1972). DOI: https://doi.org/10.1016/0014-4827(72)90481-8.

[22] Marie Engelene J Obien, Kosmas Deligkaris, Torsten Bullmann, Douglas J Bakkum, and Urs Frey. "Revealing neuronal function through microelectrode array recordings." In: *Frontiers in Neuroscience* (2015). DOI: https://doi.org/10.3389/fnins.2014.00423.

[23] Roland Thewes, Gabriel Bertotti, Normand Dodel, Stefan Keil, Sven Schröder, Karl-Heinz Boven, Guenter Zeck, Mufti Mahmud, and Stefano Vassanelli. "Neural tissue and brain interfacing CMOS devices - an introduction to state-of-the-art, current and future challenges." In: *IEEE International Symposium on Circuits and Systems (ISCAS)* (2016). DOI: https://doi.org/10.1109/ISCAS.2016.7538925.

[24] Jan Reinoud Buitenweg, Wim L C Rutten, and Enrico Marani. "Geometry-Based Finite-Element Modeling of the Electrical Contact Between a Cultured Neuron and a Microelectrode." In: *IEEE Transactions on Biomedical Engineering* (2003). DOI: https://doi.org/10.1109/TBME.2003.809486.

[25] Peter Fromherz. "Semiconductor chips with ion channels, nerve cells and brain slices." In: *First International IEEE EMBS Conference on Neural Engineering, 2003. Conference Proceedings.* (2003). DOI: https://doi.org/10.1109/CNE.2003.1196294.

[26] Rolf Weis and Peter Fromherz. "Frequency dependent signal transfer in neuron transistors." In: *Physical Review E* (1997). DOI: https://doi.org/10.1103/PhysRevE.55.877.

[27] A. L. Hodgkin and A. F. Huxley. "A quantitative description of membrane current and its application to conduction and excitation in nerve." In: *J Physiol.* (1952). DOI: https://doi.org/10.1113/jphysiol.1952.sp004764.

[28] R Quian Quiroga, Z Nadasdy, and Y Ben-Shaul. "Unsupervised spike detection and sorting with wavelets and superparamagnetic clustering." In: *Neural Computation* (2004). DOI: https://doi.org/10.1162/089976604774201631.

[29] R Quian Quiroga. "Spike sorting." In: *Scholarpedia* (2007). DOI: https://doi.org/10.4249/scholarpedia.3583.

[30] Alessio P Buccino, Cole L Hurwitz, Samuel Garcia, Joshua H Siegle Jeremy Magland, Roger Hurwitz, and Matthias H Hennig. "SpikeInterface, a unified framework for spike sorting." In: *eLife* (2020). DOI: https://doi.org/10.7554/eLife.61834.

[31] Pierre Yger et al. "A spike sorting toolbox for up to thousands of electrodes validated with ground truth recordings in vitro and in vivo." In: *eLife* (2018). DOI: https://doi.org/10.7554/eLife.34518.

[32] Christian Leibig, Thomas Wachtler, and Günther Zeck. "Unsupervised neural spike sorting for high-density microelectrode arrays with convolutive independent component analysis." In: *Journal of Neuroscience Methods* (2016). DOI: https://doi.org/10.1016/j.jneumeth.2016.06.006.

[33] *Retinitis Pigmentosa*. URL: https://www.nei.nih.gov/learn-about-eye-health/eye-conditions-and-diseases/retinitis-pigmentosa.

[34] *Summaries of Genes and Loci Causing Retinal Diseases*. URL: https://sph.uth.edu/Retnet/sum-dis.htm.

[35] *Age-Related Macular Degeneration Data and Statistics*. URL: https://www.nei.nih.gov/learn-about-eye-health/resources-for-health-educators/eye-health-data-and-statistics/age-related-macular-degeneration-amd-data-and-statistics.

[36] Wan Ling Wong, Xinyi Su, Xiang Li, Chui Ming G Cheung, Ronald Klein, Ching-Yu Cheng, and Tien Yin Wong. "Global prevalence of age-related macular degeneration and disease burden projection for 2020 and 2040: a systematic review and meta-analysis." In: *Lancet Glob Health* (2014). DOI: https://doi.org/10.1016/S2214-109X(13)70145-1.

[37] GBD 2015 Collaborators. "Global, regional, and national incidence, prevalence, and years lived with disability for 310 diseases and injuries, 1990–2015: a systematic analysis for the Global Burden of Disease Study 2015." In: *Lancet* (2016). DOI: https://doi.org/10.1016/S0140-6736(16)31678-6.

[38] Robert E Marc, Bryan W Jones, Carl B Watt, and Enrica Strettoi. "Neural remodeling in retinal degeneration." In: *Progress in Retinal and Eye Research* (2003). DOI: https://doi.org/10.1016/S1350-9462(03)00039-9.

[39] Francesca Mazzoni, Elena Novelli, and Enrica Strettoi. "Retinal ganglion cells survive and maintain normal dendritic morphology in a mouse model of inherited photoreceptor degeneration." In: *Journal of Neuroscience* (2008). DOI: https://doi.org/10.1523/JNEUROSCI.4968-08.2008.

[40] Henrike Stutzki, Florian Helmhold, Max Eickenscheidt, and Günther Zeck. "Subretinal electrical stimulation reveals intact network activity in the blind mouse retina." In: *Jurnal of Neurophysiology* (2016). DOI: https://doi.org/10.1152/jn.01095.2015.

[41] Katarina Stingl et al. "Subretinal Visual Implant Alpha IMS–Clinical trial interim report." In: *Vision Restoration* (2017). DOI: https://doi.org/10.1016/j.visres.2015.03.001.

[42] Daniel Palanker, Yannick Le Mera, Saddek Mohand-Said, Mahiul Muqit, and Jose A Sahel. "Photovoltaic Restoration of Central Vision in Atrophic Age-Related Macular Degeneration." In: *Ophthalmology* (2020). DOI: https://doi.org/10.1016/j.ophtha.2020.02.024.

[43] Lilach Bareket, Alejandro Barriga-Rivera, Marc Patrick Zapf, Nigel H Lovell, and Gregg J Suaning. "Progress in artificial vision through suprachoroidal retinal implants." In: *Jurnal of Neural Engeneering* (2017). DOI: https://doi.org/10.1088/1741-2552/aa6cbb.

[44] Laura Ferlauto, Marta Jole Ildelfonsa Airaghi Leccardi, Naïg Aurelia Ludmilla Chenais, Samuel Charles Antoine Gilliéron, Paola Vagni, Michele Bevilacqua, Thomas J Wolfensberger, Kevin Sivula, and Diego Ghezzi. "Design and validation of a foldable and photovoltaic wide-field epiretinal prosthesis." In: *Nature Communications* (2018). DOI: https://doi.org/10.1038/s41467-018-03386-7.

[45] José Fernando Maya-Vetencourt et al. "Subretinally injected semiconducting polymer nanoparticles rescue vision in a rat model of retinal dystrophy." In: *Nature Nanotechnology* (2020). DOI: https://doi.org/10.1038/s41565-020-0696-3.

[46] Victoria H Fan, Lauren E Grosberg, Sasidhar S Madugula, Pawel Hottowy, Wladyslaw Dabrowski, Alexander Sher, Alan M Litke, and EJ Chichilnisky. "Epiretinal stimulation with local returns enhances selectivity at cellular resolution." In: *Journal of Neural Engineering* (2019). DOI: https://doi.org/10.1088/1741-2552/aaeef1.

[47] Elton Ho Xin Lei, Thomas Flores, Henri Lorach, Tiffany Huang, Ludwig Galambos, Theodore Kamins, James Harris, Keith Mathieson, and Daniel Palanker. "Characteristics of prosthetic vision in rats with subretinal flat and pillar electrode arrays." In: *Jurnal of Neural Engeneering* (2019). DOI: https://doi.org/10.1088/1741-2552/ab34b3.

[48] Thomas Flores, Xin Lei, Tiffany Huang, Henri Lorach, Roopa Dalal, Ludwig Galambos, Theodore Kamins, Keith Mathieson, and Daniel Palanker. "Optimization of pillar electrodes in subretinal prosthesis for enhanced proximity to target neurons." In: *Jurnal of Neural Engeneering* (2018). DOI: https://doi.org/10.1088/1741-2552/aaac39.

[49] Thomas Flores, Tiffany Huang, Mohajeet Bhuckory, Elton Ho, Zhijie Chen, Roopa Dalal, Ludwig Galambos, Theodore Kamins, Keith Mathieson, and Daniel Palanker. "Honeycomb-shaped electro-neural interface enables cellular-scale pixels in subretinal prosthesis." In: *Scientific Reports* (2019). DOI: https://doi.org/10.1038/s41598-019-47082-y.

[50] Perry Twyford and Shelley Fried. "The Retinal Response to Sinusoidal Electrical Stimulation." In: *IEEE Transactions on Neural Systems and Rehabilitation Engineering* (2015). DOI: https://doi.org/10.1109/TNSRE.2015.2415811.

[51] Daniel K Freeman, Donald K Eddington, Joseph F Rizzo III, and Shelley I Fried. "Selective Activation of Neuronal Targets With Sinusoidal Electric Stimulation." In: *Jurnal of neurophysiology* (2010). DOI: https://doi.org/10.1152/jn.00551.2010.

[52] Andrew C Weitz, Devyani Nanduri, Matthew R Behrend, Alejandra Gonzalez-Calle, Robert J Greenberg, Mark S Humayun, Robert H Chow, and James D Weiland. "Improving the spatial resolution of epiretinal implants by increasing stimulus pulse duration." In: *Science Translational Medicine* (2015). DOI: https://doi.org/10.1126/scitranslmed.aac4877.

[53] *Retinitis pigmentosa clinical trials*. URL: https://clinicaltrials.gov/ct2/results?term=retinitis+pigmentosa\&Search=Search.

[54] Sean K Wang, Yunlu Xue, Parimal Rana, Christin M Hong, and Constance L Cepko. "Soluble CX3CL1 gene therapy improves cone survival and function in mouse models of retinitis pigmentosa." In: *PNAS* (2019). DOI: https://doi.org/10.1073/pnas.1901787116.

[55] Hendrik P N Scholl, Rupert W Strauss, Mandeep S Singh, Deniz Dalkara, and José-Alain Sahe Botond Roska Serge Picaud. "Emerging therapies for inherited retinal degeneration." In: *Science Translational Medicine* (2016). DOI: https://doi.org/10.1126/scitranslmed.aaf2838.

[56] Sylvia J Gasparini, Silvia Llonch, Oliver Borsch, and Marius Ader. "Transplantation of photoreceptors into the degenerative retina: Current state and future perspectives." In: *Progress in Retinal and Eye Research* (2019). DOI: https://doi.org/10.1016/j.preteyeres.2018.11.001.

[57] Wadood Haq, Johannes Dietter, Sylvia Bolz, and Eberhart Zrenner. "Feasibility study for a glutamate driven subretinal prosthesis: local subretinal application of glutamate on blind retina evoke network-mediated responses in different types of ganglion cells." In: *Jurnal of Neural Engeneering* (2018). DOI: https://doi.org/10.1088/1741-2552/aac811.

[58] Andreas Schatz, Tobias Röck, Lubka Naycheva, Gabriel Willmann, Barbara Wilhelm, Tobias Peters, Karl Ulrich Bartz-Schmidt, Eberhart Zrenner, André Messias, and Florian Gekeler. "Transcorneal Electrical Stimulation for Patients with Retinitis Pigmentosa: A Prospective, Randomized, Sham-Controlled Exploratory Study." In: *Investigative Ophthalmology & Visual Scienc* (2011). DOI: https://doi.org/10.1167/iovs.10-6932.

[59] Michael Haberland, Rusty L Montgomery, and Eric N Olson. "The many roles of histone deacetylases in development and physiology: implications for disease and therapy." In: *Nature reviwes. Genetics* (2009). DOI: https://doi.org/10.1038/nrg2485.

[60] Craig E Crosson, Santhosh K Mani, Shahid Husain, Oday Alsarraf, and Donald R Menick. "Inhibition of Histone Deacetylase Protects the Retina from Ischemic Injurys." In: *Investigative Ophthalmology & Visual Science* (2010). DOI: https://doi.org/10.1167/iovs.09-4538.

[61] Dragana Trifunović et al. “HDAC inhibition in the cpfl1 mouse protects degenerating cone photoreceptors in vivo.” In: *Human Molecular Genetics* (2016). DOI: https://doi.org/10.1093/hmg/ddw275.

[62] Dragana Trifunović et al. “Primary Rod and Cone Degeneration Is Prevented by HDAC Inhibition.” In: *Advances in Experimental Medicine and Biology* (2018). DOI: https://doi.org/10.1007/978-3-319-75402-4_45.

[63] J Sancho-Pelluz adn M V Alavi, A Sahaboglu, S Kustermann, P Farinelli, S Azadi, T van Veen, F J Romero, F Paquet-Durand, and P Ekström. “Excessive HDAC activation is critical for neurodegeneration in the rd1 mouse.” In: *Cell Death & Disease* (2010). DOI: https://doi.org/10.1038/cddis.2010.4.

[64] Bo Chen and Constance L Cepko. “HDAC4 regulates neuronal survival in normal and diseased retinas.” In: *Science* (2009). DOI: https://doi.org/10.1126/science.1166226.

[65] David Boinagrov, Susanne Pangratz-Fuehrer, Georges Goetz, and Daniel Palanker. “Selectivity of direct and network-mediated stimulation of the retinal ganglion cells with epi-, sub- and intraretinal electrodes.” In: *Jurnal of Neural Engeneering* (2014). DOI: https://doi.org/10.1088/1741-2560/11/2/026008.

[66] Ralph J Jensen and Joseph F Rizzo III. “Thresholds for activation of rabbit retinal ganglion cells with a subretinal electrode.” In: *Experimental Eye Research* (2006). DOI: https://doi.org/10.1016/j.exer.2006.01.012.

[67] Alfred Stett, Wolfgang Barth, Stefan Weiss, Hugo Haemmerle, and Eberhart Zrenner. “Electrical multisite stimulation of the isolated chicken retina.” In: *Vision Research* (2000). DOI: https://doi.org/10.1016/S0042-6989(00)00005-5.

[68] Max Eickenscheidt, Martin Jenkner, Roland Thewes, Peter Fromherz, and Günther Zeck. “Electrical stimulation of retinal neurons in epiretinal and subretinal configuration using a multicapacitor array.” In:

Jurnal of Neurophysiology (2012). DOI: https://doi.org/10.1152/jn.00909.2011.

[69] Elton Ho, Richard Smith, Georges Goetz, Xin Lei, Theodore I Kamins Ludwig Galambos, James Harris, Keith Mathieson, Daniel Palanker, and Alexander Sher. "Spatiotemporal characteristics of retinal response to network-mediated photovoltaic stimulation." In: *Jurnal of Neurophysiology* (2018). DOI: https://doi.org/10.1152/jn.00872.2016.

[70] Silvia Ronchi, Michele Fiscella, Camilla Marchetti, Vijay Viswam, Urs Frey Jan Müller, and Andreas Hierlemann. "Single-Cell Electrical Stimulation Using CMOS-Based High-Density Microelectrode Arrays." In: *Frontiers in Neuroscience* (2019). DOI: https://doi.org/10.3389/fnins.2019.00208.

[71] Gabriel Bertotti et al. "A CMOS-based sensor array for in-vitro neural tissue interfacing with 4225 recording sites and 1024 stimulation sites." In: *2014 IEEE Biomedical Circuits and Systems Conference (BioCAS) Proceedings* (2014). DOI: https://doi.org/10.1109/BioCAS.2014.6981723.

[72] Larissa Höfling, Jonathan Oesterle, Philipp Berens, and Günther Zeck. "Probing and predicting ganglion cell responses to smooth electrical stimulation in healthy and blind mouse retina." In: *Scientific Reports* (2020). DOI: https://doi.org/10.1038/s41598-020-61899-y.

[73] Greg Schwartz, Jakob Macke, Dario Amodei, Hanlin Tang, and Michael J Berry II. "Low error discrimination using a correlated population code." In: *Jurnal of Neurophysiology* (2012). DOI: https://doi.org/10.1152/jn.00564.2011.

[74] Günther Zeck adn Armin Lambacher and Peter Fromherz. "Axonal Transmission in the Retina Introduces a Small Dispersion of Relative Timing in the Ganglion Cell Population Response." In: *PLOS ONE* (2011). DOI: https://doi.org/10.1371/journal.pone.0020810.

[75] Douglas J Bakkum, Urs Frey, Milos Radivojevic, Thomas L Russell, Jan Müller, Michele Fiscella, Hirokazu Takahashi, and Andreas Hierlemann. "Tracking axonal action potential propagation on a high-density microelectrode array across hundreds of sites." In: *Nature Communications* (2013). DOI: https://doi.org/10.1038/ncomms3181.

[76] Lauren E Grosberg et al. "Activation of ganglion cells and axon bundles using epiretinal electrical stimulation." In: *Jurnal of Neurophysiology* (2017). DOI: https://doi.org/10.1152/jn.00750.2016.

[77] Chris Sekirnjak, Pawel Hottowy, Alexander Sher, Wladyslaw Dabrowski, A M Litke, and E J Chichilnisky. "Electrical stimulation of mammalian retinal ganglion cells with multielectrode arrays." In: *Jurnal of Neurophysiology* (2006). DOI: https://doi.org/10.1152/jn.01168.2005.

[78] Andrea Corna, Thoralf Herrmann, and Günther Zeck. "Electrode-size dependent thresholds in subretinal neuroprosthetic stimulation." In: *Journal of Neural Engineering* (2018). DOI: https://doi.org/10.1088/1741-2552/aac1c8.

[79] Archana Jalligampala, Sudarshan Sekhar, Eberhart Zrenner, and Daniel L Rathbun. "Optimal voltage stimulation parameters for network-mediated responses in wild type and rd10 mouse retinal ganglion cells." In: *Journal of Neural Engineering* (2017). DOI: https://doi.org/10.1088/1741-2552/14/2/026004.

[80] Kevin Meng, Andreas Fellner, Frank Rattay, Diego Ghezzi, Hamish Meffin, Michael R Ibbotson, and Tatiana Kameneva. "Upper stimulation threshold for retinal ganglion cell activation." In: *Journal of Neural Engineering* (2018). DOI: https://doi.org/10.1088/1741-2552/aabb7d.

[81] Richard H Masland. "The fundamental plan of the retina." In: *Nature Neuroscience* (2001). DOI: https://doi.org/10.1038/nn0901-877.

[82] Naïg Aurelia Ludmilla Chenais, Marta Jole Ildelfonsa Airaghi Leccardi, and Diego Ghezzi. "Capacitive-like photovoltaic epiretinal stimulation enhances and narrows the network-mediated activity of retinal ganglion cells by recruiting the lateral inhibitory network." In: *Jurnal of Neural Engeneering* (2019). DOI: https://doi.org/10.1088/1741-2552/ab3913.

[83] Lauren H Jepson, Pawel Hottowy, Geoffrey A Weiner, Wladyslaw Dabrowski, Alan M Litke, and E J Chichilnisky. "High-fidelity reproduction of spatiotemporal visual signals for retinal prosthesis." In: *Neuron* (2014). DOI: https://doi.org/10.1016/j.neuron.2014.04.044.

[84] Lyndon da Cruz et al. "Five-year safety and performance results from the Argus II Retinal Prosthesis System clinical trial." In: *Ophthalmology* (2017). DOI: https://doi.org/10.1016/j.ophtha.2016.06.049.

[85] Michael Beyeler, Devyani Nanduri, James D Weiland, Ariel Rokem, Geoffrey M Boynton, and Ione Fine. "A model of ganglion axon pathways accounts for percepts elicited by retinal implants." In: *Scientific Reports* (2019). DOI: https://doi.org/10.1038/s41598-019-45416-4.

[86] Max Eickenscheidt and Günther Zeck. "Action potentials in retinal ganglion cells are initiated at the site of maximal curvature of the extracellular potential." In: *Journal of Neural Engineering* (2014). DOI: https://doi.org/10.1088/1741-2560/11/3/036006.

[87] Henri Lorach et al. "Photovoltaic restoration of sight with high visual acuity." In: *Nature Medicine* (2015). DOI: https://doi.org/10.1038/nm.3851.

[88] Georges Goetz, Richard Smith, Xin Lei, Ludwig Galambos, Theodore Kamins, Keith Mathieson, Alexander Sher, and Daniel Palanker. "Contrast Sensitivity With a Subretinal Prosthesis and Implications for Efficient Delivery of Visual Information." In: *Investigative Ophthalmology & Visual Science* (2015). DOI: https://doi.org/10.1167/iovs.15-17566.

[89] Steven T Walston, Robert H Chow, and James D Weiland. "Direct measurement of bipolar cell responses to electrical stimulation in wholemount mouse retina." In: *Jurnal of Neural Engineering* (2018). DOI: https://doi.org/10.1088/1741-2552/aab4ed.

[90] Ralph J Jensen and Joseph F Rizzo III. "Responses of ganglion cells to repetitive electrical stimulation of the retina." In: *Jurnal of Neural Engineering* (2007). DOI: https://doi.org/10.1088/1741-2560/4/1/S01.

[91] Maesoon Im and Shelley I Fried. "Indirect activation elicits strong correlations between light and electrical responses in ON but not OFF retinal ganglion cells." In: *Journal of Physiology* (2015). DOI: https://doi.org/10.1113/JP270606.

[92] David Tsai, John W Morley, Gregg J Suaning, and Nigel H Lovell. "Survey of electrically evoked responses in the retina - stimulus preferences and oscillation among neurons." In: *Scientific Reports* (2017). DOI: https://doi.org/10.1038/s41598-017-14357-1.

[93] Jae-Ik Lee, Shelley I Fried, and Maesoon Im. "Network-mediated responses of ON ganglion cells to electric stimulation become less consistent across trials during retinal degenerations." In: *2017 39th Annual International Conference of the IEEE Engineering in Medicine and Biology Society (EMBC)* (2017). DOI: https://doi.org/10.1109/EMBC.2017.8037271.

[94] Alex E Hadjinicolaou, Shaun L Cloherty, Yu-Shan Hung, Tatiana Kameneva, and Michael R Ibbotson. "Frequency Responses of Rat Retinal Ganglion Cells." In: *PLOS ONE* (2016). DOI: https://doi.org/10.1371/journal.pone.0157676.

[95] Rebecca Kotsakidis, Hamish Meffin, Michael R Ibbotson, and Tatiana Kameneva. "In vitro assessment of the differences in retinal ganglion cell responses to intra- and extracellular electrical stimulation." In: *Jurnal of Neural Engineering* (2018). DOI: https://doi.org/10.1088/1741-2552/aac2f7.

[96] Susanne F Koch and Stephen H Tsang. "Success of Gene Therapy in Late-Stage Treatment." In: *Advances in experimental medicine and biology* (2018). DOI: https://doi.org/10.1007/978-3-319-75402-4_13.

[97] Claudio Punzo, Karl Kornacker, and Constance L Cepko. "Stimulation of the insulin/mTOR pathway delays cone death in a mouse model of retinitis pigmentosa." In: *Nature Neuroscience* (2008). DOI: https://doi.org/10.1038/nn.2234.

[98] Thierry Léveillard et al. "Identification and characterization of rod-derived cone viability factor." In: *Nature genetics* (2004). DOI: https://doi.org/10.1038/ng1386.

[99] Keiichi Komeima, Brian S Rogers, Lili Lu, and Peter A Campochiaro. "Antioxidants reduce cone cell death in a model of retinitis pigmentosa." In: *PNAS* (2006). DOI: https://doi.org/10.1073/pnas.0604056103.

[100] Sean K Wang, Yunlu Xue, Parimal Rana, Christin M Hong, and Constance L Cepko. "Soluble CX3CL1 gene therapy improves cone survival and function in mouse models of retinitis pigmentosa." In: *PNAS* (2019). DOI: https://doi.org/10.1073/pnas.1901787116.

[101] Ishaq A Viringipurampeer, Andrew L Metcalfe, Abu E Bashar, Olena Sivak, Anat Yanai, Zeinabsadat Mohammadi, Orson L Moritz, Cheryl Y Gregory-Evans, and Kevin Gregory-Evans. "NLRP3 inflammasome activation drives bystander cone photoreceptor cell death in a P23H rhodopsin model of retinal degeneration." In: *Human Molecular Genetics* (2016). DOI: https://doi.org/10.1093/hmg/ddw029.

[102] Jonathan Oesterle, Christian Behrens, Cornelius Schröder, Thoralf Hermann, Thomas Euler, Katrin Franke, Robert G Smith, Günther Zeck, and Philipp Berens. "Bayesian inference for biophysical neuron models enables stimulus optimization for retinal neuroprosthetics." In: *eLife* (2020). DOI: https://doi.org/10.7554/eLife.54997.

[103] Melani Sanchez-Garcia, Ruben Martinez-Cantin, and Jose J Guerrero. "Semantic and structural image segmentation for prosthetic vision." In: *PLOS ONE* (2020). DOI: https://doi.org/10.1371/journal.pone.0227677.

[104] Nishal P Shah ans Sasidhar Madugula, Lauren Grosberg, Gonzalo Mena, Pulkit Tandon, Pawel Hottowy, Alexander Sher, Alan Litke, Subhasish Mitra, and EJ Chichilnisky. "Optimization of Electrical Stimulation for a High-Fidelity Artificial Retina." In: *2019 9th International IEEE/EMBS Conference on Neural Engineering (NER)* (2020). DOI: https://doi.org/10.1109/NER.2019.8716987.

LIST OF INCLUDED PAPERS AND MAUSCRIPTS

Electrode-size dependent thresholds in subretinal neuroprosthetic stimulation

Andrea Corna, Thoralf Hermann and Günther Zeck

Published: Journal of Neural Engineering, June 2018.

https://doi.org/10.1088/1741-2552/aac1c8

Discrimination of simple objects decoded from the output of retinal ganglion cells upon sinusoidal electrical stimulation

Andrea Corna, Poornima Ramesh, Florian Jetter, Meng-Jung Lee, Jakob H Macke and Günther Zeck

Manuscript: January 2021

HDAC inhibition ameliorates cone survival in retinitis pigmentosa mice

Marijana Samardzija[1], Andrea Corna[1], Raquel Gomez-Sintes[1], Mohamed Ali Jarboui, Angela Armento , Jerome E. Roger, Eleni Petridou, Wadood Haq, Francois Paquet-Durand, Eberhart Zrenner, Pedro de la Villa, Günther Zeck, Christian Grimm, Patricia Boya, Marius Ueffing and Dragana Trifunović

Published: Cell Death & Differentiation, November 2020.

https://doi.org/10.1038/s41418-020-00653-3

1 Shared first author

2 ELECTRODE-SIZE DEPENDENT THRESHOLDS IN SUBRETINAL NEUROPROSTHETIC STIMULATION

AUTHORS Andrea Corna, Thoralf Hermann and Günther Zeck

PUBLISHED Journal of Neural Engineering, June 2018.
https://doi.org/10.1088/1741-2552/aac1c8

The project was entirely developed by the research group of Prof. Dr. Guenther Zeck (GZ, TH, AC). The study was designed by GZ, TH, and me. The goal of the study was the characterization of subretinal electric stimulation with the Alpha AMS chip R3 retina implant (Retina Implant AG). To perform the experiment the Alpha AMS chip R3 was used to stimulate *ex vivo* retina. Recording of retinal ganglion cell activity was performed with a custom flexible Micro-electrode array. TH and GZ established the experimental setup.
I contributed to the process of data collection, data analysis and manuscript writing. In more detail I performed the majority of the electrophysiological recordings and the analysis of acquired data using custom Python scripts, in part already exiting in the lab (spike-sorting) and in part designed and implemented by myself (signal processing for raw electrophysiological data, post-processing of sorted spikes, and data visualization). Together with GZ, I contributed to the writing of the manuscript.

IOP Publishing Journal of Neural Engineering
J. Neural Eng. **15** (2018) 045003 (11pp) https://doi.org/10.1088/1741-2552/aac1c8

Electrode-size dependent thresholds in subretinal neuroprosthetic stimulation

Andrea Corna[1,2,3], Thoralf Herrmann and Günther Zeck[1]

Neurophysics, Natural and Medical Science Institute, Reutlingen, Germany
[1] Natural and Medical Sciences Institute, Markwiesenstrasse 55, 72770 Reutlingen, Germany
[2] Graduate School of Neural Information Processing/International Max Planck Research School, Tübingen, Germany
[3] Institute for Ophthalmic Research, University of Tübingen, Tübingen, Germany

E-mail: guenther.zeck@nmi.de

Received 15 February 2018, revised 24 April 2018
Accepted for publication 2 May 2018
Published 6 June 2018

Abstract

Objective. Retinal prostheses have shown promising results in restoring some visual perception to blind patients but successful identification of objects of different size remains a challenge. Here we investigated electrode-size specific stimulation thresholds and their variability for subretinal electrical stimulation. Our findings indicate the range of charge densities required to achieve identification of small objects and the object—size-specific scaling of stimulation threshold. *Approach*. Using biphasic voltage—limited current stimuli provided by a light-sensitive microchip, we determined threshold charge densities for stimulation with variable electrode sizes. The stimulated activation of the retinal network was identified by recording the spiking of retinal ganglion cells in photoreceptor-degenerated mouse rd10 retinas. Stimulation thresholds were determined for cells with saturating stimulus response relationships (SRRs) but not for cells characterized by monotonically increasing or decreasing SRRs. *Main results.* Stimulation thresholds estimated in rd10 retinas ranged between 100–900 μC cm^{-2} for stimulation with small electrodes (30 μm diameter). Threshold charge density decreased with increasing electrode size and plateaued at 20 μC cm^{-2} for an electrode diameter larger than 300 μm. This trend of decreasing threshold down to a plateau value was confirmed in wild-type mouse retina suggesting an underlying physiological source. *Significance.* Our results suggest the following guidelines for retinal prosthetics employing biphasic current pulses. The encoding of small objects may be achieved through the activation of a confined set of different retinal ganglion cells, with individual stimulation thresholds spanning a wide range of charge densities. The encoding of increasing object sizes may be achieved by decreasing stimulation charge density.

Keywords: electrical stimulation, photoreceptor-degenerated retina, stimulation threshold, retina prosthetics

(Some figures may appear in colour only in the online journal)

Introduction

Blind patients who use retinal implants encounter different objects in their everyday environment [1–3]. To encode an object those electrodes of the implant covering the corresponding visual field need to stimulate a restricted set of retinal neurons and eventually evoke an object-specific retinal output activity. The encoding of different object sizes may be optimized if the object-specific stimulus threshold is known. This open question of stimulus-specific thresholds is addressed in the following work.

Although the stimulation of retinal cells and of retinal circuits has been extensively studied using different electrodes [4–10], it remains unclear how the stimulation threshold scales with electrode size. Previous studies did not investigate small (<100 μm) and large (>500 μm) electrodes simultaneously while recording the stimulated response of one ganglion cell; furthermore, these studies investigated different animal

species and evaluation methods thus preventing a direct comparison. An earlier review by Sekirnjak *et al* [11], which focused on epiretinal stimulation, did not find a correlation between electrode size and stimulation threshold expressed as charge density or as current density.

For electrical pulses the stimulation threshold had been introduced as the minimal stimulation current (or charge) required to depolarize the transmembrane voltage up to a value where ion channels open and lead to an action potential [12]. Because the resting transmembrane voltage exhibits normally distributed fluctuations [13] the transmembrane threshold voltage may be estimated from a cumulative distribution. Given that transmembrane voltages are not accessible in extracellular recordings the evoked spiking is usually considered a valid proxy. For retinal neurons and circuits comprising synaptically connected neurons, the most common approach for estimating the stimulation threshold has been to relate the stimulus strength to the evoked retinal ganglion cell (RGC) spiking using a Boltzmann function [6, 11, 14]. The threshold—estimated as the half maximal effective stimulus—is well defined for certain conditions. However, in the complex retinal networks it is unclear if stronger stimuli activate only excitatory neurons up to a saturation level or if inhibitory neurons are activated as well leading to complex stimulus response relationships [15–17].

Under physiological conditions the retinal output is modulated by illuminating photoreceptors which converge via bipolar cells onto the retinal ganglion cell under consideration. A modulation of the light intensity translates to a modulation of the ganglion cell spiking until a saturation value [18]. Conversely, the spiking in a retinal ganglion cell increases if objects of increasing size are presented. The modulation of the firing rate saturates roughly at the spatial scale of the retinal ganglion cell's dendritic field and decays for larger stimuli [19]. For artificial stimulation of retinal circuits in photoreceptor-degenerated retina it is important to understand to what degree the classical concept of stimulation threshold applies and how the induced activity compares to the physiological behavior of healthy retinal circuits.

In this study we therefore investigate electrode-size dependent stimulation of the photoreceptor-degenerated rd10 mouse retina in subretinal configuration. For identified ganglion cells we determine the electrode-size specific threshold charge density. Comparison of different cells in one retina and across retinae provides information about the threshold variability. Given that—for certain stimulus conditions—subretinal and epiretinal stimulation is mirror-symmetric [6] the results obtained here may translate to other configurations. The consideration of electrode-size specific thresholds and their variability may improve future retinal implants.

Methods

Preparation of the retina and interfacing with the stimulation microchip

The experimental procedures were carried out in compliance with the institutional guidelines of the NMI (Regierungspräsidium Tübingen). The preparation of the retina was based on earlier reports [20, 21]. Adult (>P60) rd10 and adult wildtype (C57BL/6J) mice of either sex were dark-adapted for 1 h, anesthetized and euthanized by cervical dislocation. The enucleated eye was hemisected under dim red light and the retina peeled of the sclera. Retinal portions (~$2 \times 2\,\mathrm{mm}^2$, figure 1(A)) were cut under a dissecting microscope, transferred to the chip chamber and placed on the microchip with the outer nuclear cell layer in close contact with the electrodes (subretinal configuration). Prior to the experiment, the electrode surface was gently cleaned with detergent (Tickopur R36, 5%, 80 °C, Stamm/Berlin, Germany) and rinsed with distilled water. The chip surface was coated with ~500 μl (1 mg ml^{-1}) poly-L-lysine (P1399, MW 150–300 kDa, Sigma, Germany) to facilitate adhesion of the retina. The coating does not affect electrical stimulation as localized activation of retinal neurons has been reported in previous work using the same adhesion protocol [20, 22]. The microchips were rinsed prior to positioning of the retina with Ames' medium (A 1420, Sigma, Germany). The chip with the attached retina was mounted on a custom-made circuit board attached to an upright microscope (BWX 51W, Olympus) and continuously perfused with oxygenated Ames' solution (flow rate: 2–4 ml min^{-1}, temperature: 32 °C–35 °C).

Electrical stimulation and strength-duration relation

The microchip Alpha AMS R3 used here for electrical stimulation comprises 1600 pixels arranged in 40 rows and 40 columns at equidistant positions (spacing: 70 μm, figure 1(A)) thereby covering a total area of $2.8 \times 2.8\,\mathrm{mm}^2$ [23, 24]. Each pixel embodies a microphotodiode, amplification electronics and one stimulation electrode (diameter: 30 μm) made of sputtered iridium oxide. Individual photodiodes were activated using an OLED monitor (eMagin Corp., Bellevue, WA, USA) which illuminated the back focal plane of a 4 × microscope objective (PlanC 4×/0.10). The light intensity (65 mW m^{-2}) and the illuminance (25 lux, background < 1 lux) at the retinal surface was measured using a photometer (P-2000, Gigahertz-Optik GmbH, Germany). All electrical stimulation experiments were performed at a fixed light level. Changes of the stimulation current were obtained using an adjustable global reference current ('gain parameter' figures 1(B) and (C)).

In this study stimulation using the following electrode fields was investigated: 1 × 1, 2 × 2, 4 × 4, 8 × 8, 10 × 10, 16 × 16 and 20 × 20. For each electrode and for each stimulation amplitude the stimulus was repeated twenty times (stimulation frequency: 0.5 Hz). Stimuli with different amplitudes were presented in a pseudo-random way. The change in photocurrent was transferred to user-defined current stimuli, which are voltage-limited to ±1.2 V. Here, the anodic current pulse (2 ms duration) was preceded by a cathodic pulse of the same duration, without any inter-phase interval.

Extracellular action potentials were recorded from retinal ganglion cells as described previously [20]. Briefly, a custom-build, transparent, perforated and flexible microelectrode array (flex MEA, NMI TT GmbH, Reutlingen) based

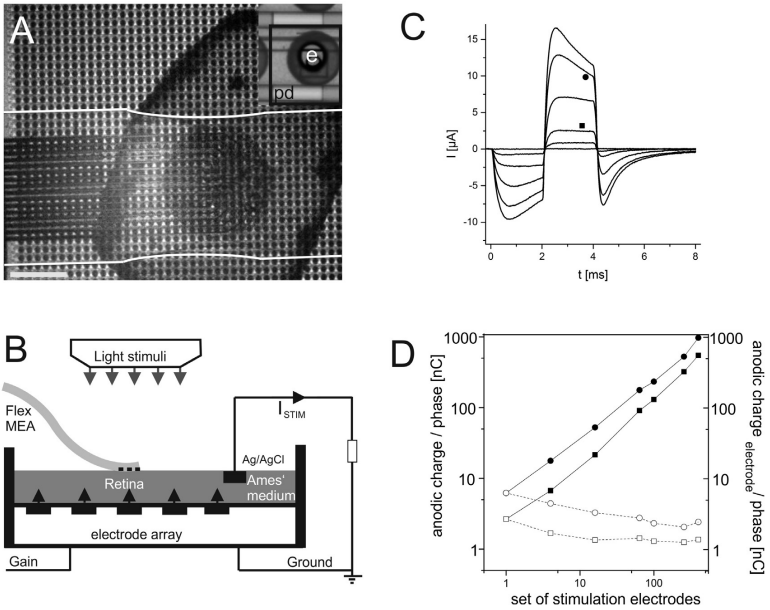

Figure 1. Experimental setup and stimulation currents. (A) Microphotograph showing an interfaced retinal portion on the subretinal microchip. The retinal output is recorded by a flexible and transparent electrode array (white line marking the flex-array border has been added for visualization). Scale bar: 500 μm. The inset shows one an enlarged stimulation pixel (*e*: stimulation electrode, *pd*: photodiode) Pixel size: 70 $\times$ 70 μm^2. (B) Schematic setup including the measurement of the stimulation current as described in the main text. The stimulation strength was adjusted using a global reference current ('Gain'). (C) Stimulation currents obtained by increasing the gain parameter. Current traces obtained for stimulation using four electrodes (a set of 2 $\times$ 2 adjacent electrodes) and six different gain settings. Positive values represent the current flowing into the Ag/AgCl electrode (B). The negative current at the termination of the 4 ms pulse is most likely caused by the capacitive current due to resetting the stimulation voltage to ground potential. Square and circular symbols refer to the gain settings shown in (D). (D) The stimulation charge delivered during the anodic phase scaled linearly with the number of electrodes (filled symbols) Data points were obtained for two different 'gain' settings and increasing electrode area (circular symbol: high gain; rectangular symbol: low gain, see also (C)). The stimulation charge per electrode decreased slightly for increasing electrode number (open symbols). Note that the data point for stimulation with one electrodes is identical for the two conditions.

on polyimide and comprising 16 electrodes was lowered onto the ganglion cell layer using a micromanipulator (MPC 200, Sutter Instruments). The perforations in the polyimide foil allow for oxygenation of the retina and thus for stable recordings over several hours. Here the flex MEA was connected to preamplifiers (Multi Channel Systems MCS GmbH, Reutlingen) and the recording was performed using MC Rack software. The recording sampling rate was 50 kHz with an amplifier input range of $\pm$400 mV. In order to extract the stimulus-evoked spiking, an analysis process including trigger alignment, artifact subtraction, spike detection and clustering of the isolated extracellular waveforms was applied. The trigger used as a reference of exact timing of electrical stimulation onset was detected from the internal clock signal of the stimulation microchip, which was recorded simultaneously using the MEA amplifier. Illumination onset was logged from the OLED-driving PCs trigger output. Based on this information the stimulation epochs were identified in the raw data, extracted and aligned. The median of all electrode signals was derived for every point in time and subtracted from individual electrode signals to remove common mode noise and to reduce stimulation artifacts. The first eight milliseconds following stimulus onset (four of which represent the stimulus duration) were excluded from spike sorting. We cannot exclude direct activation of ganglion cell spiking during the four millisecond long stimulus. However, previous work has shown that the thresholds for direct activation in subretinal configuration are considerably higher than thresholds for network activation [4]. For stimulation using 1 or 2 $\times$ 2 electrode fields we were able to remove the artefact up to the end of the stimulus. The occasional spikes recorded in this short time interval (4–8 ms following stimulus onset) do not change the evaluated stimulus response relationships (SRRs). For stimulation using larger electrode configurations (i.e. 10 $\times$ 10 electrodes) we cannot exclude spikes missed in the first milliseconds. However, as shown in figure 2 the majority of stimulated spikes occurs about 20 ms after stimulus termination. Residual stimulation artifacts were modeled by moving polynomial regression

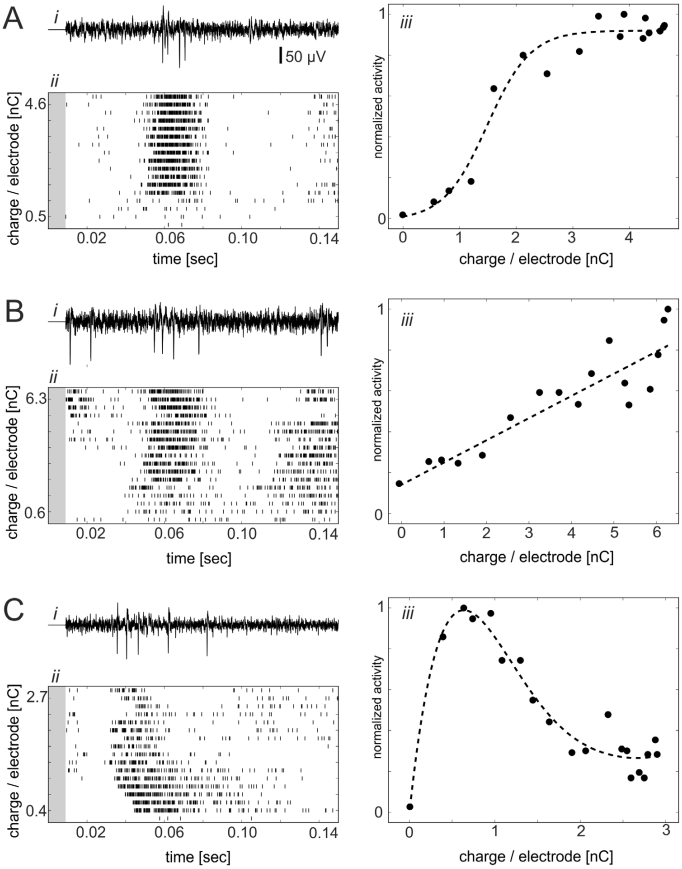

Figure 2. Three types of stimulus response relationship (SRR) obtained for subretinal stimulation. (A) Saturating SRRs after stimulation with a set of 4 × 4 electrodes. (B) Monotonic increasing SRR after stimulation with one single electrode. (C) Non-monotonic SRR after stimulation with a set of 10 × 10 electrodes. (Ai)–(Ci): high-pass filtered voltage traces recorded after one electrical stimulus. Stimulus marked by arrows. (Aii)–(Cii) Rasterplots showing the induced spiking to stimuli of different strength (quantified as stimulation charge during the anodic phase). Note, that in each row all spikes from 20 consecutive presentations are shown. The different stimulation strength were presented in a pseudo-random order. Gray region marks the first 8 ms from stimulus onset. (Aiii)–(Ciii) Saturating, monotonic and non-monotonic SRR.

(5th order on 401 points) and subtracted from the data [25]. Spike detection was performed by threshold crossing using a multiple of the median absolute deviation on each electrode as threshold (5 ∗ sigma) to compensate for high cell activity. In order to counteract sampling offsets, detected spike times were realigned to the energy center of the respective waveform. Spike waveforms were clustered by the expectation maximization algorithm [26] and separated clusters were assigned to single RGCs.

For the estimation of the stimulus-induced response, we identified RGC spikes occurring in the time window of 8–100 ms after stimulus onset. A longer time window would suffer interference from the spontaneous background activity of rd10 RGCs. Evaluation in a shorter time window (<50 ms) might miss some of the stimulated spikes (figure 2). To obtain the stimulation threshold the spike rates were fitted against stimulation charge using a sigmoidal function (Boltzmann equation, OriginLab). Stimulation threshold was defined as the value evoking 50% of the (cell-specific) maximal spike number. We did not consider the current or current density as stimulus measure because the current shape was not constant during the stimulus application (figure 1(C)). Instead we used the stimulation charge delivered during the anodic stimulation phase (figure 1(D)).

Measurement of the stimulation current

A single Ag/AgCl pellet (E201ML, Science Products) was used as counter electrode and located approximately 1 cm above the stimulation array. The stimulation current was calculated from the voltage drop across a serial 10 Ω resistor in series with the Ag/AgCl electrode [22]. The voltage drop was amplified using a commercial voltage amplifier (DLPVA, Femto Messtechnik GmbH, Berlin, Germany). Current traces for one fixed number of stimulation electrodes (here four electrodes) and increasing gain parameter are shown in figure 1(C). Positive values represent the transretinal current flowing into the Ag/AgCl electrode. Similar traces were obtained for the other electrode configurations investigated in this work (1×1, 4×4, 8×8, 10×10, 20×20). The stimuli shown in figure 1(C) were used to determine the stimulation threshold for one given electrode configuration. The scaling of the stimulation charge with electrode number is shown in figure 1(D) for two arbitrary settings of the gain parameter. The anodic stimulation charge increased linearly with electrode number ($R^2 > 0.9$). The charge per electrode during the anodic phase decayed slightly if a larger electrode field was illuminated (figure 1(D)). Both the total current of the stimulation chip and maximum electrode voltage are limited, which results in a decrease of the current per electrode when the number of illuminated and stimulating pixels was increased. The data presented in figure 1(D) were used in stimulation experiments to confirm that the correct number of pixels were illuminated.

Results

Stimulus response relations in photoreceptor-degenerated mouse retinas

It has commonly been assumed that retinal neurons increase their activity for increasing stimulation strength up to a saturation level [6, 11, 14]. Such stimulus-response relationships (SRRs) were fitted to sigmoidal relationships. However, new reports demonstrate that certain retinal circuits show a non-monotonic stimulus-response relationship upon stimulation in suprachoroidal [17] or epiretinal configuration [15]. In figure 2 we present three types of SRRs encountered here upon subretinal stimulation: (a) the well-known saturating SRR (figure 2(A)) (b) the monotonic increasing SRR (figure 2(B)) and (c) the non-monotonic SRR (figure 2(C)) showing a strong decrease of the firing rate for increasing charge densities. For stimulation with small electrodes (30 μm diameter) the majority of SRRs (73.7%, 28 out of 38 RGCs) showed a saturating behaviour figure 2(A) and 3(A). A smaller percentage of cells showed monotonic SRR (23.7%, figure 2(B)) whereas only one RGC with non-monotonic SRRs was identified. For stimulation with medium-sizes electrode fields (4×4 electrodes covering an area of ~280×280 μm^2) and for stimulation with large electrode fields (10×10 electrodes covering a stimulation area of 700×700 μm^2) the percentage of non-monotonic SRRs increased considerably (28%) while monotonic SRRs were never identified. The number of each SRR-type for the selected electrode configurations is given in table 1. The data listed in table 1 comprise all experiments, although not all experiments investigated all three stimulus conditions.

In the following we quantified thresholds only for ganglion cells with saturating SRR. This allows comparing our results with previously published work.

Variability of threshold charge density within and across retinae

The identification of small visual objects depends on the ability of a retinal implant to evoke activity above threshold using a small electrode in a confined retinal network and finally to modulate the spiking in a few ganglion cells without any crosstalk. Using one of the 1600 available electrodes (see also figure 1), we stimulated *ex vivo* rd10 retina by illuminating the micro-photodiode coupled to this electrode. A typical recording of the evoked spiking is shown in figure 2. By increasing the stimulus amplitude more action potentials were evoked in a time window up to 100 ms. The increase of the average firing rate was approximated by a sigmoidal function with the 50% value representing the stimulus threshold. Stimulation with a single electrode (30 μm diameter) increased spiking in several RGCs. We typically identified three RGCs with saturating SRR per retina, other cells showed monotonic increasing SRR (figure 3(A)).

The estimated threshold charge ranged between 0.7–6.3 nC/electrode which corresponds to a charge density range between 0.1–0.9 mC cm^{-2} ($n = 28$ RGCs). There was a weak negative correlation between stimulation threshold and spontaneous activity of the stimulated RGCs (linear fit, $R^2 = 0.4$). The mean threshold charge density was 0.44 mC cm^{-2} with a standard deviation of 0.22 mC cm^{-2}. It is worth noting that a large variability was found within individual retinae (two-fold change, figure 3(A)). The threshold variability for stimulation with one electrode can be attributed to the different physical distance between electrode and stimulated cells. We therefore evaluated thresholds using larger stimulation field, namely a set comprising 4×4 neighbouring electrodes and a set comprising 10×10 neighbouring electrodes (figures 3(B) and (C)). The estimated threshold charges ranged between 0.4–3.8 nC/electrode (4×4 electrode field, $n = 20$ RGCs) and 0.1–2 nC/electrode (10×10 electrode field, $n = 20$ RGCs). The mean threshold charge density calculated for the two electrode configurations were: 31 μC $cm^{-2} \pm 20$ μC cm^{-2} (4×4 electrode field) and 18 μC $cm^{-2} \pm 13$ μC cm^{-2} (10×10 electrode field (figure 3(C)). The mean charge density for stimulation with small electrodes is significantly different from the other two conditions ($p = 0.001$, Mann–Whitney-U test). Although the mean threshold charge densities for stimulation with 4×4 and 10×10 electrodes were significantly different ($p = 0.025$, Mann–Whitney-U test) there was a strong overlap for the threshold charge densities of individual cells. The charge density of each saturating SRR is displayed in figure 3(D) to better visualize their variability. Here, the threshold charge is plotted against threshold charge density for each evaluated SRR. By definition the data must lie on the same line whose slope is determined by the electrode area.

Table 1. Stimulus-Response relationships for retinal ganglion cells in rd10 retinae. The three types correspond to the data presented in figure 2.

SRR type/electrode set	Saturating SRR	Monotonic SRR	Non-monotonic SRR
Small electrode field: (1 × 1)	28	9	1
Medium electrode field: (4 × 4)	20	0	8
Large electrode field: (10 × 10)	20	0	8

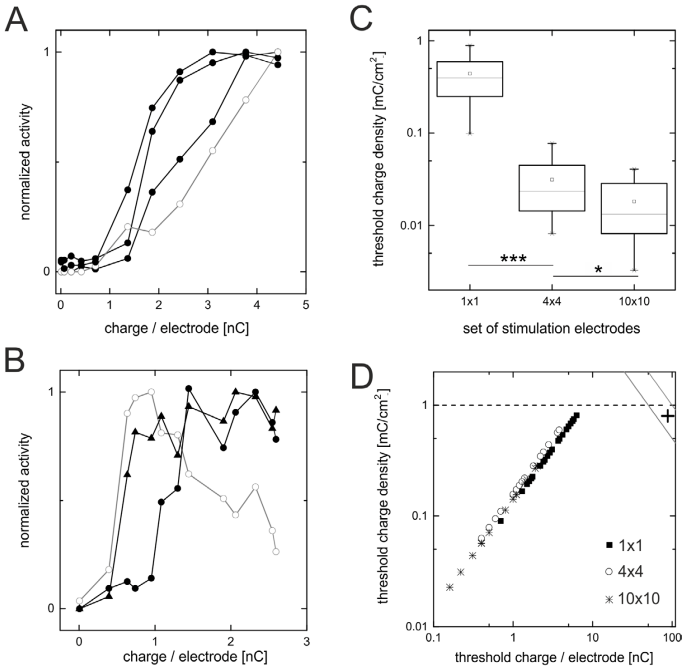

Figure 3. Threshold variability for stimulation with electrodes of different size. (A) Normalized SRRs for four RGCs in the same retina. Three SRRs of three RGCs are saturating (black symbols) while the forth example is monotonically increasing (grey symbols). Stimulation performed with one electrode (30 μm diameter). (B) Normalized SRRs obtained for three RGCs upon stimulation with a 10 × 10 array of electrodes. Two SRRs are saturating (black symbols) while the third SRR show a strong non-monotonic decrease in activity (grey symbols). (C) Box plots showing the mean threshold charge densities for stimulation with one electrode (n = 28 RGCs) a set of 4 × 4 electrodes (n = 20) and a set of 10 × 10 electrodes (n = 20). The boundaries of the box indicate the 25th percentile and the 75th percentile. Whiskers above and below the box indicate the 90th and 10th percentile. The line within the box represents the median value whereas the symbol (open symbol) denotes the mean value. Statistical significance is indicated (∗∗∗: $p < 0.001$; ∗: $p < 0.05$). (D) Individual threshold charge density plotted against charge per electrode. Each symbol represents one evaluated saturating SRR. The individual symbols representing the threshold charges are slightly shifted to avoid overlap. Included is the safety limit of iridium oxide (dashed line at 1 mC cm^{-2}), two neural-injury limits (gray lines in the upper right) obtained from cortical data and the predicted value for electroporation for 2 ms stimulus duration ('+' symbol in the upper right). See main text for details on these three limits.

Included in figure 3(D) is the lowest reported charge injection limit of iridium oxide (1 mC cm^{-2}) [27, 28]. The graph also comprises the limits for neural injury from cortical stimulation (log Q/A = k − log Q; with k = 1.7 and k = 2.0), where Q is the stimulation charge, A the electrode area and k constant values extracted from empirical data. For k = 2 neural injury has been observed in cortical stimulation experiments, whereas the second value k = 1.7 marks the transition region to observed damage [29]. In addition we display the limit of retinal electroporation derived in [30] for 2 ms long stimuli. The estimated threshold charge densities were all below the reported limits. These three limits will be discussed below. In the following we investigate in greater detail how the threshold charge density changes with electrode size.

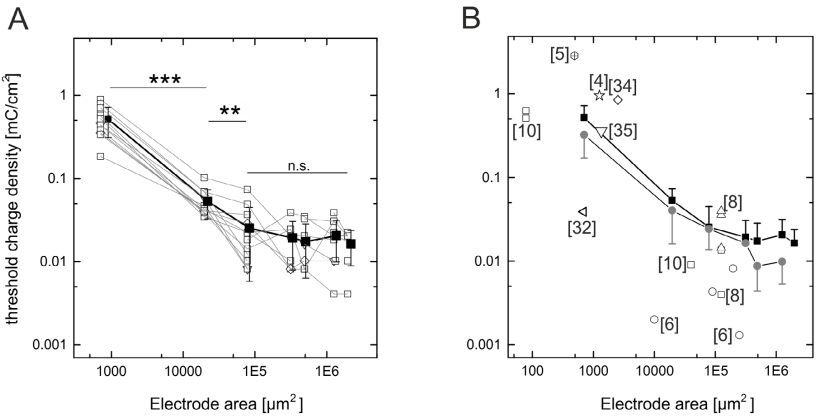

Figure 4. Threshold charge density decreases with electrode size and saturates for electrode fields larger than 78 400 μm^2 (equivalent diameter: 320 μm). (A) Threshold charge densities evaluated in rd10 retina. Gray lines connect the data obtained for individual RGCs (n = 12) Filled symbol mark mean value, error bars denote standard deviation (Filled symbols were slightly offset in *x*-direction to avoid overlap). Statistical significance is indicated (***: $p < 0.001$; **: $p < 0.01$; n.s.: no significant difference). (B) Comparison of the mean threshold charge densities in rd10 retina (black, filled symbols) with healthy, wild-type retina (gray, filled symbols) and with previously published threshold charge densities (open symbols). The numbers in square brackets refer to the cited publications. All data extracted from published work are listed in table 2.

Table 2. Literature review of the reported threshold charge densities.

Study	Electrode size (μm^2)	Threshold charge density (mC cm^{-2})	Species	Pulse polarity/ duration (ms)
[10, 31]	78.5	0.5/0.625	Chicken	Biphasic/0.5
[5]	491	2.85	Rabbit	Biphasic/2
[32]	707	0.039	Rabbit	Biphasic/10
[7]	196 343	0.008	Rabbit	Monophasic/2
[33]	2500	0.84	Rabbit	Monophasic/4
[6]	10 000/250 000	0.0013/0.0043	Rabbit	Monophasic/1
[4]	1257	0.95	Rat	Monophasic/4
[34]	1350	0.355	Mouse (wild-type)	Biphasic/2
[35]	125 600	0.013	Mouse (wild-type)	Biphasic/1
[8]	125 600	0.039	Mouse(wild-type)	Biphasic/1
[8]	125 600	0.0039	Mouse (rd1)	Biphasic/1
[35]	125 600	0.036	Mouse (rd1)	Biphasic/1
[36]	125 600	0.014	Rat (P23H)	Biphasic/1
This work	706/19 600/ 78 400/0.31 E6/ 0.49 E6/1.25 E6/ 2.18 E6	0.51/0.05/ 0.025/0.02 0.017/0.021 0.017	Mouse (rd10)	Biphasic/2
This work	706/19 600/ 78 400/0.31 E6/ 0.49 E6/1.25 E6 /	0.32/0.054/ 0.024/0.016 0.009/0.01	Mouse (wild-type)	Biphasic/2

Electrode-size dependent threshold charge density for single RGCs

We recorded a total of 12 RGCs with saturating SRRs which were stimulated with at least five different electrode configurations. The individual thresholds are shown in figure 4(A). For individual cells and for the mean threshold charge density we observed a remarkable trend: the threshold charge density decreased for increasing electrode size and reached a constant value when the electrodes covered a retinal area of 280 × 280 μm^2 (78 400 μm^2). The mean threshold charge densities for different electrode configurations are listed in table 2. Statistical comparison between the individual stimulus configurations revealed that the mean threshold charge densities for electrode areas larger than 78 400 μm^2 (equivalent diameter: 320 μm) are not significantly different ($p > 0.05$). This result may contrast to the statistical evaluation shown in figure 3(C).

However, for the mean thresholds shown in figure 3(C) values from different recordings were pooled. The mean threshold charge densities for small electrodes were significantly different from the average thresholds obtained for large electrodes. The significance level is indicated in figure 4(A).

As noted for stimulation with individual electrodes we found a large variability of individual stimulation thresholds. Threshold charge densities ranged between 8–73 μC cm^{-2} for stimulation using a set of 4 $\times$ 4 electrodes (78 400 μm^2) and between 4–40 μC cm^{-2} for stimulation using a set of 16 $\times$ 16 electrodes (125 000 μm^2).

Electrode-size dependent threshold charge density in healthy retina

Although not the major focus of this work we evaluated stimulation thresholds in healthy, wild-type mouse retinae. We identified ten RGCs with saturating SRR upon stimulation with a 30 μm electrode. The mean threshold charge density was 0.36 mC cm^{-2} with a standard deviation of 0.15 mC cm^{-2} (figure 4(B)). This mean threshold charge density was only slightly smaller than the mean threshold charge density obtained for rd10 retinas and not significantly different ($p = 0.27$, Mann–Whitney-U test). The threshold charge density for wild-type RGCs was investigated for six different electrode sizes. The trend of decreasing charge density followed by a plateau value was detected here as well (figure 4(B)) for RGCs with a saturating SRR. The average threshold values for all electrode fields are listed in table 2. Non-saturating SRRs were detected for stimulation with large electrode fields (10 $\times$ 10) in RGCs of wild-type retinae (data not shown).

Finally, threshold charge densities were estimated from previously published work. In table 2 we summarize the reported data. These data were obtained from different animal species and using slightly different stimulus parameters (see last column in table 2). This might explain the large spread of the threshold values (figure 4(B), open symbols). Although the published thresholds are in line with our data it would not have been possible to infer the trend inferred from our measurements.

The electrical stimulation of healthy retina provided the opportunity to investigate the physiological response as well. In an additional control experiment we presented light flashes at a repetition rate of 1 Hz onto the interfaced retina having the stimulating microchip switched off. This experiment allowed us to determine the physiological response polarity of the electrically recorded RGC. The recordings for two example RGCs are shown in figure 5. For the ON RGC, which increases the spike rate upon incremental light stimuli (figure 5(A)) the following electrical stimulation pattern was detected. Within few millisecond after the electrical stimulus we detected a brief burst of spikes followed by a prolonged inhibition of spiking (figure 5(B)). The second RGC (figure 5(C)), which was inhibited by the presented light flashes, showed one brief burst of spikes upon the electrical stimulus (figure 5(D)). The activity patterns following electrical stimulation in both RGCs are different when compared to the stimulated activity in the rabbit retina [6, 37], which showed multiple clearly separated spike bursts. The ON electrical response in OFF RGCs however is in line with a previous report from rat retina [38]. A thorough investigation of the biological and cellular origin is beyond the aim of this study.

The light activity shown in figure 5 was recorded after the termination of the electrical stimulation. It thus demonstrates that the experimental configuration used here ('sandwich') does not perturb the retinal physiology.

Discussion

The encoding of objects of different size by retinal prostheses requires robust spiking upon stimulation with a corresponding electrode size. Stimulation thresholds are an indicator for the required stimulation strength. Here we identified the threshold range for stimulation with electrodes ranging between 30 μm in diameter up to an electrode field covering a retinal area larger than one square-millimetre. The quantification was performed for RGCs showing a saturating stimulus response relation (SRR). We identified a similar percentage of saturating SRRs upon stimulation with small electrodes (73.7%) as upon stimulation with large electrode fields (71.4%, see table 1). For stimulation with large electrode fields we observed non-saturating RGCs (28.6%). With one exception, non-saturating SRRs were not detected upon stimulation with one electrode.

Our report on different SRRs (figure 2 and table 1) are in line with recent studies reporting such behaviour upon stimulation in suprachoroidal [17] or stimulation in epiretinal configuration [15]. In the three studies, including ours, only spikes with a delay of more than eight milliseconds after stimulus presentation and thus SRRs induced by the stimulated retinal network were considered. Inhibition evoked by stimulation of the retinal network using strong stimuli could originate from stimulation of inhibitory retinal neurons [39] which in turn supress the activity of ganglion cells. Alternatively, non-monotonic SRRs could originate from a reduction in excitability of bipolar cells caused by a reversal of calcium flow. The second hypothesis, which has been suggested in a recent theoretical work [16], does not depend on stimulus size but rather on stimulus strength. Given that non-monotonic SRRs were detected for large electrode sizes (table 1) and rather low stimulation charge densities (figure 2(C)) the hypothesized activation of inhibitory retinal circuits better explains our results.

Stimulation with electrodes as small as 30 μm separated by 70 μm (center-to-center distance) will be sufficient to evoke a spatial resolution of ~0.3° [40]. To the best of our knowledge our work for the first time reports threshold values in photoreceptor-degenerated retina upon stimulation with individual small electrodes (compare table 2). Threshold values of an infrared-sensitive photovoltaic subretinal implant have been reported, however only with respect to the infrared light intensity and not the stimulation current or charge [41]. The threshold charge densities reported here are in the range of values reported previously for subretinal stimulation in healthy retinas [4–6, 10, 31, 33]. For stimulation in epiretinal configuration successful stimulation with even smaller electrodes

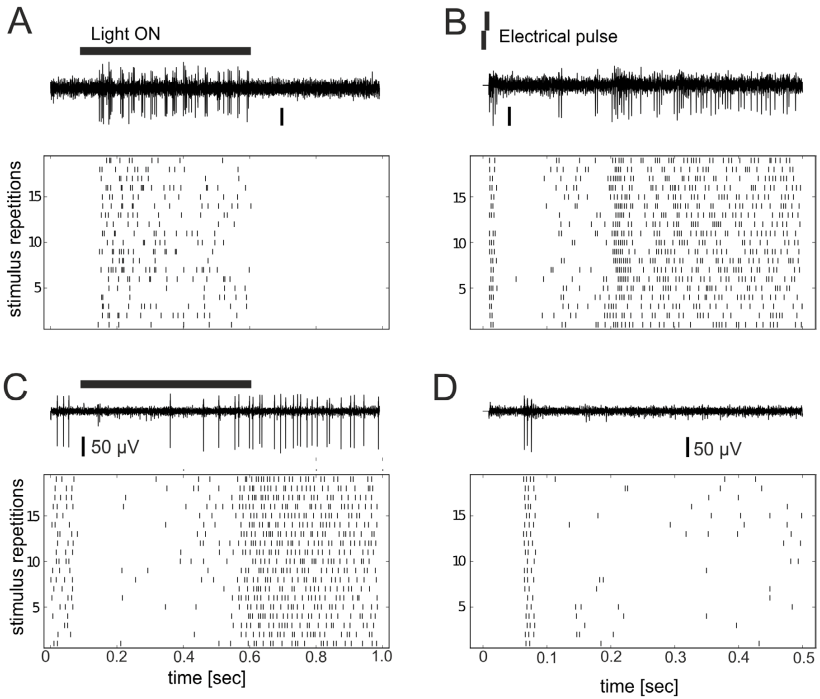

Figure 5. Light responses and electrical responses in the healthy retina. (A) Light stimulated activity recorded from an RGC in C57Bl/6 retina. Upper panel: high pass filtered electrode signal showing the light-induced activity induced by an incremental light stimulus (500 ms duration). Lower panel: raster plots showing 20 repetitions of the same stimulus presentation. (B) Electrically induced activity of the cell shown in (A). A first brief burst of spikes was followed by a strong inhibition of the spiking. (C) Light stimulated activity recorded from a second RGC cell in C57/Bl6 retina responding with a decrease in activity upon light onset. (D) Electrical response of the RGC shown in (C). This RGC was strongly activated with a time delay of about 50 milliseconds following the electrical stimulus.

may be feasible [11, 42]. However, when comparing stimulation thresholds one carefully needs to distinguish between direct activation of RGCs and network–mediated spikes [4, 6]. For network-mediated spikes in the healthy retina threshold charge densities for epiretinal and for subretinal configuration are in the same range [4, 6].

All our estimated threshold values are below the reported safety limits for iridium oxide of 1 mC cm^{-2} or 3 mC cm^{-2} respectively [27, 28]. The threshold charge densities obtained here may be compared to values inducing tissue damage [29, 30].We note that the neural injury limits presented in figure 1(D) were extrapolated from cortical data which used a minimal stimulus charge of 1 μC. These neural injury limits may need to be reconsidered in future work. Furthermore, as worked out in the study of Butterwick *et al* [30] the thresholds for cell electroporation strongly depend on pulse duration. Considering the phase duration of 2 ms, a threshold current density of 0.7 A cm^{-2} (equivalent to 1.4 mC cm^{-2}) had been estimated [30]. All the stimulation thresholds reported here are below this value (figure 1(D)). A smaller threshold for tissue damage (0.44 mC cm^{-2}) had been estimated by Cohen *et al* [43] for epiretinal configuration using rabbit retina. Future studies potentially using retina with properties closer to humans will resolve the reported discrepancy.

The observed trend of decreasing stimulation threshold with electrode size may be explained by the concept of the retinal ganglion cell's receptive field [19]. In the healthy retina photoreceptor signals converge onto bipolar cells which themselves send converging input onto one retinal ganglion cell [19]. In the photoreceptor-degenerated retina the receptive field concept appears to remain valid as evaluated from electrical stimulus protocols [20, 38, 41]. The spatial extent of the electrical receptive fields in mouse and rat retina is about 300 μm in diameter (~70 000 μm^2) when evaluated with stimulation electrodes closely (<1 μm [45];) interfaced to the *ex vivo* retina [20, 38, 41]. In our experiments stimulation with electrodes larger than 79 000 μm^2—which roughly equals the receptive field of a retinal ganglion cell—does not change the threshold charge per electrode. One likely explanation is that stimulated bipolar cells outside the receptive field do not converge onto the RGC under consideration and thus do not influence the identified ganglion cell spiking. Similarly,

stimulation of only a subset of bipolar cells requires stronger stimuli to depolarize the recorded RGC above threshold. The trend of decreasing and then saturating threshold charge densities may be translated to the design of retinal implants or their stimulation strategy. The stimulation charge may be adjusted according to the number of simultaneously stimulating adjacent electrodes, as suggested by the trend reported in figure 4(A).

Stimulation thresholds for rd10 and for wild-type retinae were not significantly different here. This finding contrasts with earlier reports on significant threshold differences between photoreceptor-degenerated rd1 retina and healthy C57/Bl6 retina [8, 35]. However, a recent study [44] identified only a weakly elevated threshold in rd10, which strongly depended on the level of spontaneous activity. Lower stimulation thresholds for highly active RGCs were observed here as well. In the study by Cho *et al* [44] as well as in our work a large variance of stimulation thresholds was identified. This large variance may be attributed to inhomogeneity of the retinal resistivity [45] and to cell-type specific threshold variations [46]. We suggest that the threshold variance rather than mean values need to be considered when optimizing retinal implants.

Conclusion

Stimulation thresholds for biphasic pulsatile waveforms scale with electrode size in subretinal configuration. For stimulation with small electrodes, retinal implants must cover a wide range of stimulation charge densities (0.1–0.9 mC cm^{-2}). Simultaneous stimulation with many electrodes and strong stimuli (>1 nC/electrode) inhibits the retinal network (non-monotonic SRR in 28% of the RGCs). Therefore a constant stimulation charge density irrespective of the size of the stimulated retinal network may lead to identification of small but not of large objects. To circumvent this effect our study suggests that retinal implants may adjust the stimulation charge density depending on the object size to be encoded.

Acknowledgments

This work was partially supported by the German Research Foundation (DFG): SFB 1233, Robust Vision: Inference Principles and Neural Mechanisms, TP 14 to AC and GZ. The authors acknowledge two Alpha AMS R3 microchips obtained from Retina Implant AG, Reutlingen. We thank Dr Gerhard Heusel (NMI TT GmbH, Reutlingen) for providing customized flexible MEAs.

ORCID iDs

Günther Zeck https://orcid.org/0000-0003-3998-9883

References

[1] Zrenner E *et al* 2011 Subretinal electronic chips allow blind patients to read letters and combine them to words *Proc. R. Soc.* B **278** 1489–97
[2] Luo Y H and da Cruz L 2015 The argus II retinal prosthesis system *Prog. Retin. Eye Res.* **50** 89–107
[3] Ayton L N *et al* 2014 First-in-human trial of a novel suprachoroidal retinal prosthesis *PLoS One* **9** e115239
[4] Boinagrov D *et al* 2014 Selectivity of direct and network-mediated stimulation of the retinal ganglion cells with epi-, sub- and intraretinal electrodes *J. Neural Eng.* **11** 026008
[5] Tsai D *et al* 2009 Direct activation and temporal response properties of rabbit retinal ganglion cells following subretinal stimulation *J. Neurophysiol.* **102** 2982–93
[6] Eickenscheidt M *et al* 2012 Electrical stimulation of retinal neurons in epiretinal and subretinal configuration using a multicapacitor array *J. Neurophysiol.* **107** 2742–55
[7] Jensen R J and Rizzo J F 2005 Thresholds for activation of rabbit retinal ganglion cells with a subretinal electrode *Exp. Eye Res.* **83** 367–73
[8] Jensen R J and Rizzo J F 3rd 2009 Activation of ganglion cells in wild-type and rd1 mouse retinas with monophasic and biphasic current pulses *J. Neural Eng.* **6** 035004
[9] Jensen R J, Ziv O R and Rizzo J F 2007 Responses of rabbit retinal ganglion cells to electrical stimulation with an epiretinal electrode *J. Neural Eng.* **2** S16–21
[10] Stett A *et al* 2000 Electrical multisite stimulation of the isolated chicken retina *Vis. Res.* **40** 1785–95
[11] Sekirnjak C *et al* 2006 Electrical stimulation of mammalian retinal ganglion cells with multielectrode arrays *J. Neurophysiol.* **95** 3311–27
[12] Plonsey R and Barr R C 2007 *Bioelectricity: a Quantitative Approach* 3rd edn (Berlin: Springer)
[13] Tuckwell H C and Walsh J B 1983 Random currents through nerve membranes 1. uniform poisson or white noise current in 1 dimensional cables *Biol. Cybern.* **49** 99–110
[14] Samba R, Herrmann T and Zeck G 2015 PEDOT-CNT coated electrodes stimulate retinal neurons at low voltage amplitudes and low charge densities *J. Neural Eng.* **12** 016014
[15] Jalligampala A *et al* 2017 Optimal voltage stimulation parameters for network-mediated responses in wild type and rd10 mouse retinal ganglion cells *J. Neural Eng.* **14** 026004
[16] Werginz P and Rattay F 2016 The impact of calcium current reversal on neurotransmitter release in the electrically stimulated retina *J. Neural Eng.* **13** 046013
[17] Barriga-Rivera A *et al* 2017 High-amplitude electrical stimulation can reduce elicited neuronal activity in visual prosthesis *Sci. Rep.* **7** 42682
[18] Sakmann B and Creutzfeldt O D 1969 Scotopic and mesopic light adaptation in the cat's retina *Pflügers Arch.* **313** 168–85
[19] Rodieck R W 1998 *The First Steps in Seeing* (Sunderland, Massachusetts: Sinauer Associates, Inc.)
[20] Stutzki H *et al* 2016 Subretinal electrical stimulation reveals intact network activity in the blind mouse retina *J. Neurophysiol.* **116** 1684–93
[21] Menzler J, Channappa L and Zeck G 2014 Rhythmic ganglion cella ctivity in bleached and blind adult mouse retina *PLoS One* **9** e106047
[22] Eickenscheidt M and Zeck G 2014 Action potentials in retinal ganglion cells are initiated at the site of maximal curvature of the extracellular potential *J. Neural Eng.* **11** 036006

[23] Rothermel A *et al* 2009 A CMOS chip with active pixel array and specific test features for subretinal implantation *IEEE J. Solid-State Circuits* **44** 290–300
[24] Daschner R *et al* 2018 Functionality and performance of the subretinal implant chip Alpha AMS *Sens. Mater.* **30** 179–92
[25] Savitzky A and Golay M J E 1964 Smoothing and differentiation of data by simplified least squares procedures *Anal. Chem.* **36** 1627–39
[26] Kadir S N, Goodman D F and Harris K D 2014 High-dimensional cluster analysis with the masked EM algorithm *Neural Comput.* **26** 2379–94
[27] Cogan S F *et al* 2009 Sputtered iridium oxide films for neural stimulation electrodes *J. Biomed. Mater. Res.* B **89** 353–61
[28] Beebe X and Rose T 1988 Charge injection limits of activated iridium oxide electrodes with 0.2 ms pulses in bicarbonate buffered saline (neurological stimulation application) *IEEE Trans. Biomed. Eng.* **35** 494–5
[29] Shannon R V 1992 A model of safe levels for electrical stimulation *IEEE Trans. Biomed. Eng.* **39** 424–6
[30] Butterwick A *et al* 2007 Tissue damage by pulsed electrical stimulation *IEEE Trans. Biomed. Eng.* **54** 2261–7
[31] Stett A, Mai A and Herrmann T 2007 Retinal charge sensitivity and spatial discrimination obtainable by subretinal implants: key lessons learned from isolated chicken retina *J. Neural Eng.* **4** S7–16
[32] Yang Y T *et al* 2011 Responses of rabbit retinal ganglion cells to subretinal electrical stimulation using a silicon-based microphotodiode array *Invest. Ophthalmol. Vis. Sci.* **52** 9353–61
[33] Im M and Fried S I 2015 Spatial properties of network-mediated response of retinal ganglion cells to electric stimulation *2015 7th Int. IEEE/EMBS Conf. on Neural Engineering (NER)* (IEEE) (https://doi.org/10.1109/NER.2015.7146608)
[34] SimS L *et al* 2014 Simultaneous recording of mouse retinal ganglion cells during epiretinal or subretinal stimulation *Vis. Res.* **101** 41–50
[35] Jensen R J and Rizzo J F 3rd 2008 Activation of retinal ganglion cells in wild-type and rd1 mice through electrical stimulation of the retinal neural network *Vis. Res.* **48** 1562–8
[36] Jensen R J and Rizzo J F 3rd 2011 Effects of GABA receptor antagonists on thresholds of P23H rat retinal ganglion cells to electrical stimulation of the retina *J. Neural Eng.* **8** 035002
[37] Im M and Fried S I 2015 Indirect activation elicits strong correlations between light and electrical responses in ON but not OFF retinal ganglion cells *J. Physiol.* **593** 3577–96
[38] Ho E *et al* 2018 Spatio-temporal characteristics of retinal response to network-mediated photovoltaic stimulation *J. Neurophysiol.* **119** 389–400
[39] Masland R H 2001 The fundamental plan of the retina *Nat. Neurosci.* **4** 877–86
[40] Eckhorn R *et al* 2006 Visual resolution with retinal implants estimated from recordings in cat visual cortex *Vis. Res.* **46** 2675–90
[41] Lorach H *et al* 2015 Photovoltaic restoration of sight with high visual acuity *Nat. Med.* **21** 476–82
[42] Jepson L H *et al* 2013 Focal electrical stimulation of major ganglion cell types in the primate retina for the design of visual prostheses *J. Neurosci.* **33** 7194–205
[43] Cohen E *et al* 2011 Optical coherence tomography imaging of retinal damage in real time under a stimulus electrode *J. Neural Eng.* **8** 056017
[44] Cho A *et al* 2016 Changes in ganglion cell physiology during retinal degeneration influence excitability by prosthetic electrodes *J. Neural Eng.* **13** 025001
[45] Zeitler R, Fromherz P and Zeck G 2011 Extracellular voltage noise probes the interface between retina and silicon chip *Appl. Phys. Lett.* **99** 263702
[46] Fried S I *et al* 20009 Axonal sodium-channel bands shape the response to electric stimulation in retinal ganglion cells *J. Neurophysiol.* **101** 1972–87

3 DISCRIMINATION OF SIMPLE OBJECTS DECODED FROM THE OUTPUT OF RETINAL GANGLION CELLS UPON SINUSOIDAL ELECTRICAL STIMULATION

AUTHORS Andrea Corna, Poornima Ramesh, Florian Jetter, Meng-Jung Lee, Jakob H Macke and Günther Zeck

MANUSCRIPT January 2021

The framework of this project was a collaboration between the research group of Prof. Dr. Guenther Zeck (GZ, AC, FJ, M-JL) and the research group of Prof. Dr. Jakob H Macke (JHM, PR). The study was initiated and designed by FJ, GZ and myself, with the contribution of JHM and PR.
The electrophysiological CMOS MEAs recordings of *ex vivo* mouse retina were performed by myself, FJ and M-JL. A few primate retinas were recorded by M-JL. Data analysis was done by myself together with FJ, and, for the part regarding the logistic regression model, by PR, with input from JHM. Data visualization was done by myself, with the help of GZ, FJ and PR. All authors helped with the writing and scientific discussion.

Abstract: Most neuroprosthetics implants employ pulsatile square-wave electrical stimuli, which are significantly different from physiological intra-neuronal communication. In case of retina neuroprosthetics such stimuli fail to provide sufficient specificity for reliably object discrimination in implanted blind patients. Here, we report that application of sinusoidal electrical stimuli to *ex vivo* retina of photoreceptor-degenerated mouse, of healthy mouse or of primate instantaneously and reliably modulates the activity of retinal ganglion cells (RGCs) in spatially confined areas at low stimulation threshold. Spatially confined objects were formed by an arbitrary combination of 1024 stimulation electrodes. RGCs located above the stimulation electrodes were activated within each stimulus phase (25 or 40 Hz) at threshold charge densities of 40 nC per mm^2 and phase. Classification of overlapping but spatially displaced objects (1° separation) was achieved by distinct spiking activity of selected RGCs. A classifier (regularized logistic regression) discriminated spatially displaced objects (size: 5.5° or 3.5°) with high accuracy (90% or 62%). Stimulation with low artificial contrast (10%) encoded by different stimulus amplitudes generated RGC activity, which was classified with an accuracy of 80% for large objects (5.5 °). We conclude that time-continuous smooth-wave stimulation provides robust, localized neuronal activation ex vivo which may enable future artificial vision at high temporal, spatial and contrast resolution.

Introduction:

Avoidance of obstacles or discrimination of nearby objects represents one of the major needs of blind patients. Object discrimination and recognition tasks are routinely performed after blind patients receive a prosthetic implant [1]. Although in several cases remarkable results were obtained, in the best cases achieving reading acuity (for Retinitis Pigmentosa patients: [2], for AMD patients: [3]), statistical evaluation of vision restoration provides a mixed picture. Major challenges remain, including fading of evoked precepts [4, 5] low spatial resolution which does not overcome legal blindness [6] and a reduced contrast perception [7].

To resolve these challenges two main strategies need to be pursued. The first is improving electrode design. The second is optimizing pulsatile stimulation or finding an alternative to it. To improve spatial resolution, 3D electrodes and localized return electrodes, have been suggested [8, 10]. Spatially selective stimulation is achieved by confining the electric field and improving electrode-neuron interface. However, these solutions were tested exclusively in subretinal configuration, and their efficacy in epiretinal stimulation is yet to be proven. Contrast resolution achieved by pulsatile implants in blind patients is limited to few grey levels [7, 11]. Recent approaches aimed to overcome square-wave pulses inferred the mean effective stimulus from spike-triggered averaging white-noise current input [12, 13] but obtained very short, almost pulsatile waveforms. Another alternative is sinusoidal stimulation. With such stimuli a more confined retinal activation was shown as compared to pulsed stimuli [14] as well as reliable activation estimated at single cell level [15]. However, a quantitative evaluation of continuous sinusoidal stimulation to study the level of spatial and contrast resolution obtained from the readout of a large population (~1000) of retinal ganglion cells is missing.

Evaluation of different stimulation strategies at single spike resolution in large neuronal populations has not been demonstrated, mainly because of the artefact evoked by electrical stimuli. Recording of large populations of retinal ganglion cells (RGCs) was shown by Ho et al. in subretinal configuration using a combination of two micro-electrode arrays [16] but with blanking several milliseconds

following each stimulus pulse. In epiretinal configuration single-cell resolved recording and axon tracking has been achieved for sub-millisecond pulsatile stimuli only [17]. Alternatively, electrical stimulation has been combined with calcium imaging of retinal ganglion cell activity, however with poor temporal resolution [14].

We here report on the spatial and temporal performance achieved with sinusoidal stimuli in ex vivo retina mainly of adult photoreceptor-degenerated mouse retina. Control experiments were performed on the retinae of healthy mice and primates. The experiments made use of a high-density CMOS-based microelectrode array [18], which comprises a dense stimulation electrode array and a second, interleaved recording array. By simultaneously stimulating and electrically imaging up to hundreds identified RGCs, we tested the efficiency of epiretinal stimulation in terms of reliability, charge threshold and long term stability. We addressed the problem of quantifying spatial resolution and artificial contrast discrimination, at the population level using a logistic regression model. Our data show, to our knowledge for the first time, that electrically stimulated objects separated by 32 µm, and contrast levels of 10%, can be classified with high fidelity.

Methods:

Preparation of the retina and extracellular recording using Complementary metal-oxide-semiconductor based microelectrode arrays (CMOS-MEA):

Retina preparation was performed using adult (older post-natal day 60) B6.CXB1-Pde6brd10/J (*rd10*) and C57BL/6J (*wild-type*) mice of either sex as described previously [19]. Different recordings were collected from different retinas or from different positions of the same retina. In case multiple positions were recorded from the same retina, a distance larger than the calculated radius of activation was kept between the different positions. All experimental protocols were approved by the Regierungspräsidium Tübingen according to German federal laws on animal welfare.

Prior to the experiment, the surface of the CMOS MEA was gently cleaned with detergent (Tickopur R60, 5%, Stamm/Berlin, 80°C), rinsed with bi-distilled water and treated for 30 s with a plasma cleaner (Harrick Plasma). The hydrophilic chip surface was coated with ~500 µl (1 mg/ml) poly-L-lysine (P1399, MW 150–300 kDa, Sigma, Germany) to facilitate adhesion of the retina. Retinal portions (~4 mm^2) were transferred to the chip chamber and placed with RGCs in close contact with the electrodes (Figure 1C). The CMOS MEAs were rinsed prior to positioning of the retina and continuously perfused (flow rate 2–4 ml/min, temperature 34 - 36°C) with carbogenated Ames medium (A1420, Sigma). The chip comprising the attached retina was mounted on the amplifier placed on a motorized x-y stage (CONEX CC, Newport) in an upright microscope (BWX 51W, Olympus).

To evaluate the effects of network activity on evoked response, we performed control experiment using a 100 uM DNQX (Tocris Cat. No. 2312) and 20 uM AP5 (Tocris Cat. No. 3693) in addition to the standard Ames medium in order to block synaptic inputs to RGCs. Recording where performed after 30 minutes of continuous perfusion to guarantee the complete application of the drug,

A CMOS-MEA comprising 4225 recording electrodes, with an electrode pitch of 16 µm (65×65 lattice, total area: 1×1 mm^2) and 1024 stimulation electrodes was used (Figure 1B/1C) (CMOS-MEA5000-System, Multi Channel Systems MCS GmbH). Recordings were performed at 20 kHz using CMOS-MEA Control software (Multi Channel Systems MCS GmbH). Signal was band-pass filtered at 1-3.5 kHz to remove artefacts of electrical stimulation. In some cases, a larger band for the filter was used (300-4000 Hz) in combination with an artefact reduction method (offset correction and baseline subtraction) (Figure 1D). Spike sorting was performed to detect single cell firing, using the implementation of an ICA-based algorithm [20] in the CMOS-MEA-Tools software (Multi Channel Systems MCS GmbH) that allows tracking of the axons using average electrical images obtained by Spike Triggered Averaging (STA) based method (Figure 1A).

Electrical stimulation using CMOS-based MEA:

We applied sinusoidal stimuli of two different frequencies and of different amplitudes with different electrode size areas using selected electrodes of the CMOS-MEA. Applying voltages to the stimulation electrodes evokes capacitive currents in the electrolyte. The stimulation current density is proportional to the time derivative of the electrode voltage and scales with the specific electrode capacitance C: istim = c*dV/dt (1). For sufficiently large stimulation currents, a high specific capacitance is required. So-called high K oxides provide a specific capacitance of 1 – 2 µF/cm2, depending on the oxide thickness and material, with a stimulation voltage up to 3V [18]. However, to increase the specific capacitance we omitted here the sputtered oxide used in previous studies [21] and relied on the native oxide of the top titanium nitride electrode [22].

The stimulation current was measured as described previously [19] (Figure 1D). Briefly, a single Ag/AgCl pellet (E201ML, Science Products) was used as a counter electrode and located in the electrolyte above the CMOS MEA. The stimulation current was calculated from the voltage drop across a serial 10 Ω resistor in series with the Ag/AgCl electrode. The voltage drop was amplified using a commercial voltage amplifier (DLPVA, Femto Messtechnik GmbH, Berlin, Germany) and recorded using the analog channel of the interface board of the CMOS MEA 5000. Stimulation charge and charge density was calculated during the anodic phase. The total charge during a full sinusoidal stimulation period was zero.

For both, the spatial and contrast discrimination tasks, the retina was stimulated for 100 ms with a 40 Hz sinus with 500 milliseconds breaks between stimuli (Figure 1B). For spatial discrimination two stimuli were alternated between each other for 50 times. In the contrast discrimination task, for one contrast level, stimulation was applied at different intensities from two adjacent stimulation areas. The difference of current intensity between the two areas defined the artificial contrast by the equation: artificial contrast = (intensity 1 – intensity 2) / (intensity 1 + intensity 2). Each contrast level was repeated 40 times.

Analysis:

Data analysis was performed using custom analysis written in Python. Distance of the cell from the stimulation area was calculated from the center of the electrode stimulation area. Reliability was calculated evaluating the response of a cell to sinus cycles and defined as follows: a cell was identified as responding to a cycle, when firing at least once during the cycle. A cell responding to every cycle will have reliability of 1. The total reliability of a cell during a recording/stimulation protocol is calculated as the mean of reliability of single repetitions. To take in account spontaneous activity, we also evaluated the relative cell response as: cell response = (spikes during stimulation - spikes during spontaneous activity) / (spikes during stimulation + spikes during spontaneous activity).

Evaluation of activation radius was obtained fitting a one dimensional Gaussian distribution to the cell response versus the distance from electrode center. For the evaluation of cell response of jitter task a symmetrical two dimensional Gaussian was used.

Logistic Regression model

Logistic regression model: To check whether RGC responses reliably reflected differences in stimuli for the spatial and contrast discrimination tasks, we used a logistic regression (LR) model [23]. LR describes the probability of one of two possible events (denoted by y=0 or y=1), given some factors *x*. . For example, with the spatial discrimination task, we would use the logistic regression model to predict whether the stimulus was at the first position ($y = 0$) or at the second position ($y = 1$), given the RGC responses. For RGC responses x, under the logistic regression model, we write down the probability of the stimulus-identity $p(y \mid x)$ as follows:

$$z = w \cdot x + b$$

$$r = \frac{e^{-z}}{1 + e^{-z}}$$

$$p(y \mid x) = r^{y} (1 - r)^{1 - y},$$

where w is a vector of regression parameters, b is a bias parameter, and x a vector consisting of the spike count for each neuron. The activation variable z (the vector product of w and x) is passed

through a sigmoid function to obtain the model-predicted probability r of the stimulus having identity 1. The values of w correspond to the strength of contribution of each neuron in decoding the stimulus identity i.e. how strongly each neuron's response influence $p(y \mid x)$. We can learn these w of the LR model by maximising an objective function: the log probability $log\ p(y \mid x)$with respect to w, for the set of responses$x$ obtained experimentally and the corresponding stimulus identity y,

$$w^* = argmax_w \frac{1}{2N} \sum_{i=1}^{N} \quad y_i\ log\ r_i\ +\ (1\ -\ y_i)\ log\ (1\ -\ r_i)$$

where $N$is the number of times the experiment was repeated. The objective function was maximised to find w using the scipy optimisation package [24].

For the spatial discrimination task, we showed $N = 50$ repetitions of two alternating stimuli at different positions on the stimulation grid. We denoted position 1 as $y = 0$ and position 2 as $y = 1$. For each stimulus and repeat, we constructed x by counting the total number of spikes fired by each recorded neuron between stimulus onset and offset i.e in each 100ms window while the stimulus was presented, resulting in $2N$ =100 vectors x, each of which had a length equal to the number of neurons recorded. We then trained the logistic regression model on x and the corresponding y values, by computing the log probability $log\ p(y|x)$ and maximising it with respect to the parameters w.

For the contrast discrimination task, we showed $N = 40$repetitions of stimuli of 7 different contrast levels. The contrast levels were 0%, 10%, 20%, 30%, 40%, 50% and 100%. We defined 6 different logistic regression models -- in each model, the first stimulus ($y = 0$) was always the 0% contrast, while the second stimulus ($y = 1$) varied from 10% to 100% -- in other words, the discrimination task always involved differentiating a non-zero contrast stimulus from the zero-contrast stimulus. As with the spatial discrimination task, for each of the 7 stimuli and each repeat, we constructed response vectors x by counting spikes fired by all recorded neurons during stimulus presentation. We thus had 280 different response vectors, and 80 per logistic regression model. Once again, we trained the 6

logistic regression models on the corresponding x, y pairs by maximising the log probability of y given x.

While training the logistic regression models, we performed a random 80-20 split of the data repetitions into a training set and a test set. The training data was used to learn the regression parameters w. The test dataset, which the model did not have access to during training, was used to calculate the prediction accuracy of the model. The random split was repeated 5 times; the models were fit anew for each split and the results were averaged across these 5 splits.

Regularisation and cross-validation:

In order to prevent the regression weights w from varying too much from neuron to neuron, we imposed a smoothing L2 penalty [25] i.e. we modified the objective function to include the squared norm of w i.e. $\lambda|w|^2$, and maximised this new objective function with respect to w. This ensured that the elements of w did not vary too much between different neurons. The hyperparameter λ controlled the strength of the smoothing penalty.

We optimised λ by performing a grid search with 5-fold cross-validation. We first defined a grid of 30 λvalues ranging from 0.1 to 100 at uniform intervals in log-space. For each value of λ, we randomly split the repetitions in the data into 5 folds, where each fold contained 80% of the repetitions as the training set and 20% as validation set Note that this 5-fold splitting occurred on the training data input to the model i.e. 80% of all available experimental data. With this value of λ from the grid, we cycled through the 5 folds, fit the model on the training set and computed the objective function on the validation set. This cross-validated objective function was averaged across the 5 folds. The λ with the highest value of the cross-validated objective function was chosen, and used for all further analysis with the model.

Accuracy score: We calculated the predictive accuracy of the trained models for both discrimination tasks on the test data (20% of all experimental data). The accuracy score is defined as follows:

$$accuracy = \frac{p(\hat{y}=1|\, y=1) + p(\hat{y}=0|\, y=0)}{p(y=1) + p(y=0)},$$

where $\hat{y}$ is the model prediction. In practice, this score is calculated as $\frac{number\ of\ correct\ model\ predictions}{total\ number\ of\ model\ predictions}$.

Thus, this value is bounded between 0 and 1. An accuracy score of 1 indicates that the model perfectly predicts the stimulus identity given responses. A score below 0.5 indicates that the model cannot decode stimulus identity from the responses, and that simply guessing the stimulus identity at random would give us better performance than the model.

Accuracy with a reduced neural population: We next wanted to check how robust the decoding performance was i.e. how many neurons from the population were actually required to get maximal test accuracy. In order to do this, we repeated the analysis described above, but using responses only from a fraction of the neural population recorded. We first sorted the neurons in descending order of their absolute value in regression parameter w. Note that this value indicates the contribution of a particular neuron's responses to the decoding performance in the training data for the logistic regression model. We then used the responses of only a fraction of the neurons with the highest regression values to fit new logistic regression models, and calculated the test accuracy of these models. The population fractions used were 1%, 10%, 20%, 40%, 50% and 75%.

Results

Here we propose and demonstrate an efficient strategy of discriminating spatial and contrast differences of simple objects using the stimulated retinal activity. We base our approach on the following three hypotheses: (i) retinal cells or networks in photoreceptor degenerated retinas are modulated reliably (without fading) by continuous sinusoidal electrical stimuli; (ii) the modulation of the spiking of retinal neurons decreases strongly with distance from the stimulating electrode and (iii) the readout of ganglion cells subpopulations from different stimuli enables discrimination of spatial displacement and contrast. Results supporting these hypotheses and how they are combined into an efficient decoding scheme are presented in this section.

A prerequisite in the development and evaluation of any stimulation strategy is the simultaneous recording of the evoked activity, ideally without stimulation artefacts [26]. Here we took advantage of a CMOS-based microelectrode array [18] with spatially interleaved 1024 stimulation electrodes (stimulation electrode pitch: 32µm, electrode area: 632 µm2; equivalent diameter: 28.3 µm) and 4225 electrodes (Fig. 1).

Application of sinusoidal stimuli to the selected electrodes modulates the interfaced retinal network (Figure 1D) and leads to rhythmic ganglion cell activity. To identify the appropriate "stimulation range" of the interfaced retina different stimulation amplitudes were applied (Figure 1D). Typical stimulation currents applied by the CMOS MEA range between 1 - 6 µA (See Method section). Notably, because of the low electrode capacitance (35 pF / electrode) the stimulation current does not change if retina is interfaced to the electrode array, in contrast to the majority of electrical stimulation approaches [19]. The electrical characterization of the capacitive electrodes (frequency behavior, linearity with stimulus amplitude and with stimulation area) is presented in the supplement (Supp. Figure 1)

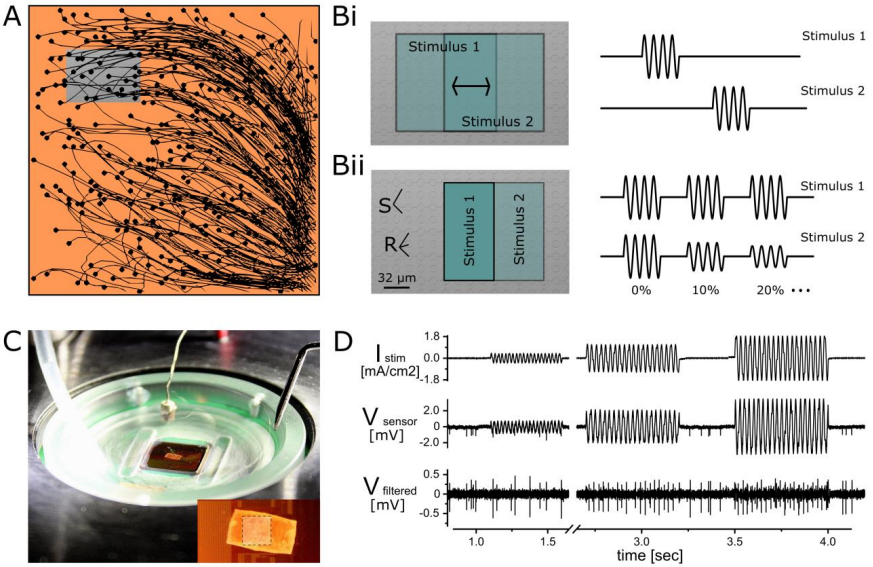

Figure 1: Experimental Setup and stimulation protocols. A) CMOS electrical imaging, showing identified positions for the RGC somas (circle) and axons (line) detected for a representative retina sample within the 1x1mm^2 electrode array. Details of the grey area are shown in B. B) schematic of the spatial (Bi) and contrast (Bii) discrimination task. Left, in grey (see A), a SEM image showing details of the CMOS MEA array with stimulation (S) and recording (R) electrodes. Bi) Spatial discrimination task: two partially overlapping stimulation areas, stimulus 1 and 2, are selected and activated alternately with the same stimulation strength for 50 repetitions. The discrimination task consists of response discrimination to stimulus 1 versus stimulus 2 Bii) Contrast discrimination task: two adjacent stimulation areas, stimulus 1 and 2, are selected and activated simultaneously with different stimulation strength to create a single contrast level for 40 repetitions. The contrast discrimination task consists of response discrimination between different contrast levels. C) Experimental setup showing the CMOS MEA with interfaced retina in a culture chamber, perfused by a heated inlet. In addition, the outlet of the perfusion system and the Ag/AgCl reference electrode are visible. The insert shows the interfaced ex vivo retina and the electrode array (1 mm2. dashed outline). D) top: Sinusoidal stimulation current density for three different amplitudes and 40Hz frequency. Middle: raw recording from one of the 4225 recording electrodes, with stimulation artefact. Bottom: Signal after filtering/artefact removal, demonstrating spontaneous and stimulus-induced spikes.

Reliable activation of retinal networks by low-amplitude sinusoidal stimuli

The recording presented in Figure 1D suggests that application of sinusoidal stimuli leads to reliable RGC spiking. In the following, we test the hypothesis of reliable spiking for stimulation protocols applied to rd10 retina.

HD MEA recording allows us to precisely detect RGC soma and axon locations upon spike triggered averaging of multiple electrical images [27]. We recorded and analysed in the same retina two prototypical cases: an RGC close to the center of the stimulation electrode (Figure 2A, cell 1) and an RGC outside the electrode but with its axon crossing the electrodes (Figure 2A, cell 2). In Figure 2 (B-C-D) we show the evoked activity for these two exemplary cells upon stimulation with increasing electrode areas. To enable a better comparison to previous studies we calculated an equivalent electrode diameter: 56.7 µm, 113.5 µm; 170 µm (Figure 2A). The normalized reliability parameter quantifies if at least one spike is evoked per stimulation phase (see description in Method section). For cell 1, located above the stimulation electrodes, stimulation with a small electrode area (equivalent diameter: 56.7 µm) proved to be ineffective up to the charge density of 150 nC/mm2 (equivalent to: 0.6 nC). For larger stimulation areas (0.01 mm^2, 0.023 mm^2) we observe that stimulation with low amplitude evokes few spikes. Increasing the charge density to 150 nC/mm^2 leads to a reliability close to 1, which corresponds to one spike detected in every stimulus phase (Fig.2B – C). For cell 2, with the soma located far away and the axon passing over the stimulation electrodes, there is no effect for localized stimulation. To confirm the general excitability of this RGC we demonstrate activation using a large electrode (0.65 mm^2) covering the RGC and its presynaptic circuit. For these two cells we also calculated the stimulus-induced firing rate. The firing rate is used to determine the threshold charge density, defined as the increase of the spontaneous activity by 30% (figure 2D).

From the example cells shown in Fig.2A we proceed to the entire RGC population (n = 102) identified in this retina and select RCGs located directly over the stimulation electrodes (n = 6). For these RGCs cells we calculated reliability and threshold charge density for different stimulation areas (Figure 2 E). The reliability and the threshold charge density approaches a narrow range (r:0.8-1, threshold:10 – 30 nC/mm^2, equivalent to 0.2 – 0.6 nC) for electrodes larger than 0.02 mm^2.

Retina degeneration causes a remodelling of the inner retina network in the mice blind model rd10, compared to the healthy retina in wild type. It is not clear yet to which degree this modification affects the response to electrical stimulation [28]. Moreover, for clinical applications, it is very valuable to evaluate if results obtained in rodent retina are confirmed in other models, such as non-human primate. We therefore evaluated stimulation thresholds and response reliability for healthy mouse (n = 47/43 RGCs at 25/40 Hz identified in 3 retinas, C57Bl6/J), non-human primate retina (n = 36 RGCs identified in 2 retinas) and RGCs in adult rd10 (n = 77/76 RGCs at 25/40 Hz RGCs, n= 2 retinas) for two different stimulation frequency (Figure 2F). No statistical difference ('Mann–Whitney U test') was found among the different conditions except when comparing RGCs in wild-type retina stimulated at 25 Hz with RGCs in rd10 (40 Hz). Here the p-values for average reliability and threshold were 0.026 and 0.013 respectively. In summary, the low stimulation threshold and high reliability appears to translate between different species.

Finally, stable reliable activation over minutes and hours is crucial for application of a stimulation strategy in an implant. We continuously stimulated retina tissue and recorded activity at specific time points to evaluate reliability in rd10 and in primate retina. Ganglion cells in *rd10* retina showed high spiking reliability without spiking dropouts for a stimulation charge density of 150 nC/mm^2. Similar results were found in primate retina (Figure 2G). Previous work has shown that pulsatile stimuli (duration: 2 ms) cannot reliably modulate RGC activity in the healthy retina [4, 29] and fail to provide continuous visual percepts to blind patients [7, 30]. In summary, the results presented here confirm our first hypothesis of reliable modulation of the retinal networks and cells located above the stimulation electrodes by sinusoidal stimuli.

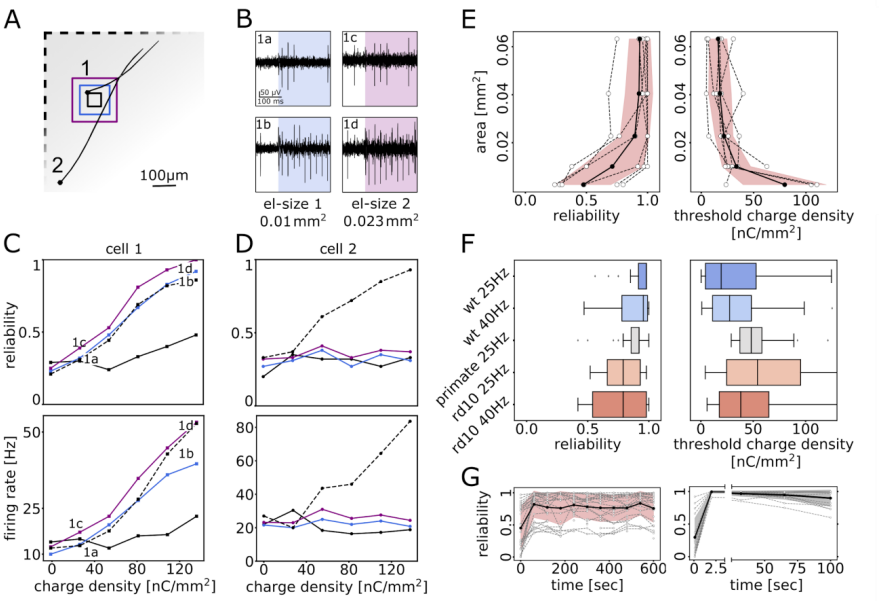

Figure 2: Reliability and charge threshold. A) STA identified soma and axon for two model RGCs with soma placed over stimulation electrodes (cell 1) or soma distant and axon passing over stimulation electrodes (cell 2). Colored square indicates 4 different stimulation areas, central black square: 0.0025 mm^2, blue: 0.01 mm^2, purple: 0.023 mm^2, edge black square: 0.65 mm^2 (full-field). B) Response of cell 1 at two different areas (blue and purple) shown in figure A and two different intensities (panels 1a & 1c obtained for stimulation with 29 nC/mm^2; panels 1b&1d obtained for stimulation with 146 nC/mm^2). (C and D) reliability and firing rate for cell 1 and cell 2 in response to the 4 stimulation areas shown in figure A, for 6 different stimulation intensity levels. Cell 1 shows a weak response to the smaller area, while it correlates very well for larger areas. Cell 2 responds only to full field stimulation. The labels 1a - 1d refer to the traces shown in (B). E) Reliability and charge threshold versus stimulation area size for RGC placed over the stimulation electrodes for a single retina. F) between species difference for reliability and threshold charge density. Data pooled from different retinas. I and G) long term reliability for rd10 (left) and primate (right).

Spatially confined modulation of retinal networks and stimulation mechanism

Based on the results presented in Figure 2, two stimulation strategies may be pursued: (i) stimulation at the stimulation threshold (~ 40 nC/mm^2) or (ii) stimulation using that amplitude (150 nC / mm^2) which leads to very high spiking reliability. We favour the second strategy here, as this ensures that fast changes in stimulation amplitude are immediately translated in modulation of the firing rate while

staying in the range for safe stimulation. For this stimulation amplitude we evaluated the spatial selectivity of two different stimulation electrodes areas: 0.01 mm^2 and 0.023 mm^2 (Figure 2A: blue and purple electrode; Figure 3A).

The high spontaneous activity encountered in photoreceptor-degenerated retinas (rd10) makes it difficult to use the reliability index and firing rate to measure spatial selectivity over the total RGC population. Instead, we evaluated the stimulated RGC response, defined as an increase of firing rate normalized on spontaneous activity (see methods for details).

In order to estimate the spatial selectivity of sinusoidal stimulation we evaluated the relative activation for a large population of RGCs. Even with CMOS-MEAs the identification of RGCs within 1 mm^2 is limited to hundreds of cells, which underestimates the true number of RGCs within this area. We therefore pooled multiple recordings (n = 6-8), after alignment of the position on the center of the stimulation area. We reached a cell density of over 900 cells/mm^2 [31] in rd10 retina (Fig. 3A) based on recordings from the adult mouse (age: postnatal day 115 - 139). From now on, we will refer to these artificial samples as "merged retina".

The spatial selectivity of sinusoidal stimulation for the "merged *rd10* retina" is shown in Fig.3B. Cell response decreases rapidly outside the stimulation area (marked by white dashed line). We estimated the radius of activation around the stimulus centre as the sigma of a gaussian fit to the cell's response. For the two electrode sizes investigated here the calculated activation radii were 57.4±3.3 µm and 81.6±3.4 µm respectively. These values are close to the electrode /object size (equivalent radius: 56.7 µm and 85 µm). The spatial selectivity is also found in individual retinae (Fig. 3C), although the estimation of the radius of activation was not possible because of the reduced number of cells.

To further investigate spatial selectivity and the stimulation mechanism we repeated the same analysis on WT retina. Our results show a substantial difference of RGC activation in WT retina as compared to rd10. The activation of RGCs outside the electrode area indicates the recruitment of the RGC network not identified in *rd10* retina. Therefore, in WT retina, stimulation may involve the retinal

network presynaptic to the RGC. To prove this hypothesis, we applied ionotropic glutamate receptor blockers (DNQX + AP5), which block the excitatory input to the RGCs. The results obtained for WT retina (mouse age: P100) after drug application resembled the results in rd10 with a radius of activation of 73.2±10.9 µm. There was no difference in RGC activation in rd10 before and after drug application (75.4±6.6 and 80.5±5.8 µm respectively) (Supp. Figure 2).

The stimulation results for the "merged retina" (Figure 3) comprise more than a thousand cells (0.01 mm^2: 1294 cells; 0.023 mm^2: 1409 cells). Out of these cells, only a few cells distant from the stimulation electrodes showed a high cell response.

Electrical imaging of the axon path allowed us to identify all RGCs with axons passing over the stimulation electrodes (el-size 1: n = 83, el-size 2, n = 74; suppl. Figure 3). We could not detect a significant change of firing rate (stimulus charge density: 150 nC/mm^2) in any of these RGCs.

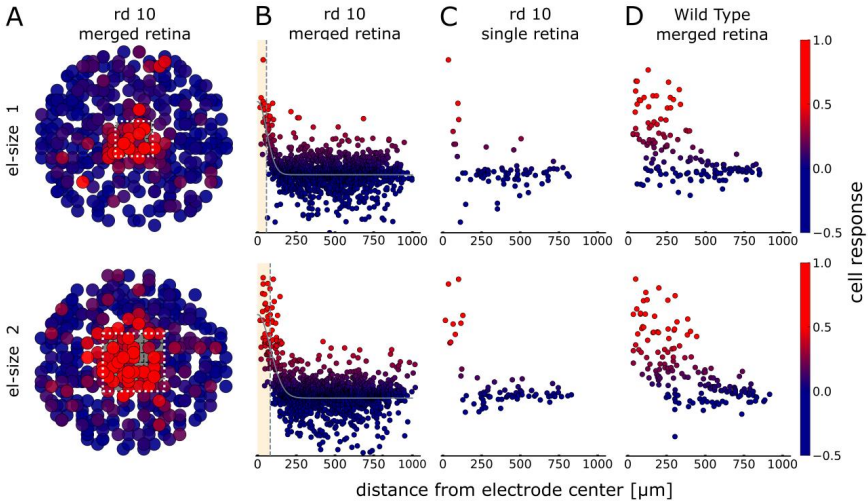

Figure 3: Spatial resolution. A) Spatial distribution, in a radius of 350 µm around stimulation centre, of RGC response to sinusoidal stimulation for two different areas (white dashes square) for the merged rd10 sample. B) RGC response of all the detected cells versus distance from the centre of the stimulation electrodes for WT and rd10.

Discrimination of spatially displaced objects

Once we established the spatial selectivity of sinusoidal stimulation we proceeded to test how this translates into encoding of spatial information. It has been reported in clinical trials, that retina implants failed to encode small shapes [7, 32]. We therefore opted for a protocol to investigate discrimination of distinct response patterns with very localized stimuli. We performed a spatial displacement protocol described in Figure 1B, (details in methods section). We selected two subsets of stimulation electrodes, each forming two equal shapes, displaced by a defined spatial jitter. Alternating the two stimuli for 50 repetitions, we tested the ability to discriminate the two stimuli based on the RGC population response. We used this protocol to test two sizes of stimulation areas, 0.01 mm^2 and 0.023 mm^2, and different displacements, 32 µm and 64 µm displacements for the first area and 32, 64, 128 µm for the second.

Area [mm^2] jitter[µm]	Δx	σ1	σ2	Accuracy (merged)	Accuracy (mean)	Accuracy (min)	Accuracy (max)
0.01	29.8±5.9	53.9±3.2	52.7±3.2	0,62	0,66	0,55	0,83
32							
0.01	59.2±6.0	55.7±3.1	62.2±3.1	0,7	0,73	0,6	0,83
64							
0.023	18.7±5.6	76.6±2.9	70.6±2.9	0,9	0,69	0,59	0,86
32							
0.023	50.3±6.4	77.2±3.3	77.2±3.3	1	0,87	0,73	0,99
64							
0.023	120.4±4.7	76.3±2.6	79.1±2.6	1	0,99	0,97	1
128							

Table 1: Results of spatial discrimination for different electrode size (Area) and spatial jittes. Δx = distance between gaussian fit centers of stimulus 1 and 2. σ1, σ2 = σ of gaussian fir for stimulus 1 and 2. Accuracy = discrimination accuracy between stimulus 1 and 2 calculated with the logistic regression model for the merged sample (merged) and the mean (mean), the worst (min) and best (max) accuracy for single recording.

We evaluated the accuracy of discriminating the response to the two stimuli, first fitting the response with a two-dimensional symmetrical Gaussian distribution (Figure 4A). A summary of the gaussian fit parameters, i.e. estimated distance (Δx) from distribution center along jitter axis and sigma for the two stimuli is shown in Table 1. In figure 4B, the one-dimensional section of the fit along the jitter axis is shown. From the plot in Figure 4B, it is clear that the response for all the stimulation areas and jitter are strongly overlapping. Thus, the model cannot accurately discriminate between the two stimulus conditions from the RGC responses. Our conclusion is that independent models are not the correct method to evaluate a neural network response to stimulation, and that it is necessary to use a population approach [33].

Hence, here we propose to use a logistic regression model to discriminate between RGCs response to stimulation. In this model, we treat the two stimuli as binary events i.e. 0 for the first stimulus and 1 for the second stimulus. We train the model to predict the probability of each event (or stimulus identity), given the responses of the RGC population. We then compute the accuracy of the model predictions on a test dataset that was not shown to the model during training (see Methods section for details). Results for test sets are shown in figure 4B and Table 1. For the 64 µm jitter, we were able to discriminate with high accuracy for both electrode sizes. El-size 1 (0,01 mm^2): 0.7 / 0.73 (merged/mean of single retinas) and el-size 2 (0.023 mm^2): 1 / 0.87. For the smaller jitter, 32 µm, only stimulation with the larger size provided good results: 0.9/ 0.69. The logistic regression parameter for each cell correlated well with the difference in firing rates between the two stimulus conditions (Supp. Figure 4). The discrimination performance was highly variable across different retina samples. The best sample had a test accuracy of over 0.8 for all stimulation areas and jitter conditions. However, there were samples that had very poor performance for smaller stimulation areas, and smaller jitters.

Finally, we investigate how the number of neurons affected the accuracy. We calculated the accuracy for different subsets of the population, selecting the fraction of neurons with the highest logistic

regression parameter values. For most samples, we found that only 20-40% of the neurons with highest parameter values were needed in order to reach the accuracy of the full population. This effect was consistent across all protocols and samples. The logistic regression parameter is positively correlated with the difference in firing rate between the two stimulus conditions, and the difference in firing rate is in turn negatively correlated with the cell's distance from the stimulation electrodes (see Figure 3 B and C). Hence, this indicates that the fraction of the neural population located closest to stimulating electrodes is the most predictive of the stimulus identity. For the sake of clarity, we show here the results for 3 exemplary stimulations (Figure 4D).

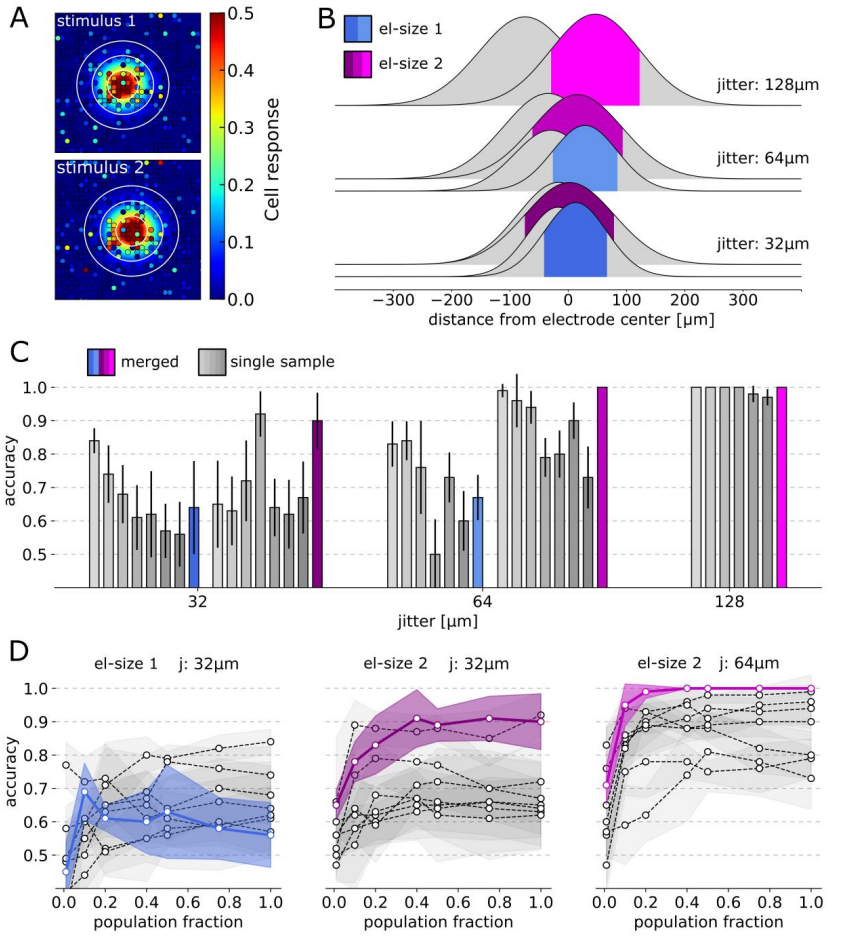

Figure 4: Discrimination of spatially shifted objects. A) Two dimensional gaussian fit to cell response for two stimulated objects (0,01 mm^2) with a local displacement of 32 µm. White circles marke the 1,2 and 3 sigma contours. B) Section of the gaussian fit along the jitter axis, for different object sizes and spatial displacements (jitter). A strong spatial overlap is detected. stimulation areas and jitters, showing the overlap of the response to the two stimulations. (: blue: el-size 0.01 mm2; purple: 0.023 mm^2: C) discrimination accuracy for the jitter task (coloured bar: merged sample, grey: single retina). D) Subpopulation fraction accuracy for three exemplary test-sets. E) Difference of reliability multiplied by cell response between two stimuli for each neuron used in the model sorted by Bayesian weight. From left to right the weight on descending order. The colour of the marker indicates the normalized weight of the neuron. Left, in blue, an example of a retina sample with low accuracy (0.01 mm^2 stimulation area), right in purple an example of good accuracy (0.023 mm^2).

Discrimination of artificial contrast

We performed a similar experiment and analysis as shown in Fig.4 to determine the discrimination accuracy for stimuli with different artificial contrast. Details of the stimulation protocol are provided in the methods section. Briefly, we tested five object sizes (0.005 – 0.046 mm^2) and 7 contrast levels (0%, 10%, 20%, 30%, 40%, 50%, 100%). We tested the discrimination accuracy in a pairwise fashion, comparing the cell response of homogenous objects (0% contrast) to stimulated objects with the remaining six contrast levels. Evaluation using the logistic regression model reveals the following results (Fig. 5): (i) Discrimination accuracy increases with contrast and reaches (in most conditions) a plateau at 40-50% contrast; (ii) Discrimination accuracy improves with object size. Once again, the discrimination accuracy varies considerably across different retinal samples. The best discrimination performance at the lowest contrast tested (10%) is obtained for the largest object size with 80% accuracy. This result translates to a discrimination of total stimulation charge of 0.5 nC for electrode sizes of 0.023 mm^2.

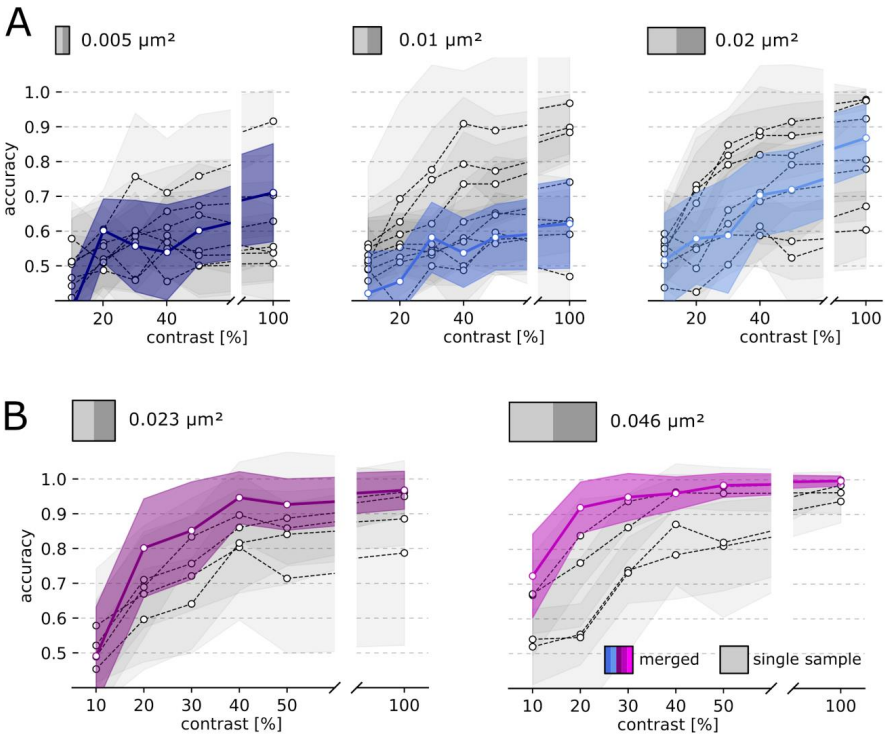

Figure 5: Discrimination of artificial contrast. (Details of the experimental protocol are shown in method and Figure 1). We tested 5 electrode size areas for 6 contrast levels (10,20,30,40,50 and 100%). Electrode size and shape is shown on top of each subplot (grey box). Half of the electrode area (light grey) was kept at fixed stimulation amplitude, while the stimulation amplitude of the second half (dark grey) was progressively lowered to create the different artificial contrast levels. Discrimination task was performed in a pairwise fashion: accuracy refers to discrimination between the six different contrast levels and 0% contrast. Coloured lines show accuracy for the merged sample while grey lines for single recordings.

Discussion

In this study, we demonstrated that sinusoidal continuous stimulation enables robust and spatially selective activation of retinal ganglion cells. Our approach, performed in epiretinal configuration, avoids axonal stimulation and enables discrimination of electrically stimulated objects displaced by as little as 32 µm (1° visual angle).

Before discussing the hurdles of artificial stimulation which can be overcome by sinusoidal stimulation, we briefly highlight the technology that enables artificial stimulation. Simultaneous electrical stimulation and recording of neuronal activity is a challenging task due to the so-called stimulation artefact. A solution of this problem is offered by high-density microelectrode arrays, with electrode distances in the order of ~ 10 – 20 µm [18, 34]. Using CMOS-based high density MEAs [35], electrical imaging of stimulated axonal activity in neuronal cell cultures using short stimulus pulses (< 100 µs) was reported. Electrical stimulation with single electrodes followed by electrophysiological imaging of axonal activation has been reported for ex vivo primate retina [17] but restricted in terms of stimulus shape and electrode distance (60 µm). The CMOS-based MEA presented here employs two separate but intermingled electrode arrays one for stimulation and one for recording. It enables the selection of arbitrary stimulation areas and the application of arbitrary stimulus waveforms, eventually leading to a truly bidirectional electrical interfacing.

The presented sinusoidal stimulation approach overcomes the following obstacles in artificial stimulation. First, we were able to avoid fading or desensitisation of the evoked ganglion activity as reported previously for pulsatile stimulation [4, 36], despite using a stimulation frequency (40 Hz) which is well above the flicker fusion frequency for the mouse retina. Reduced desensitization of retinal ganglion cell spiking to sinusoidal stimuli has been reported in healthy rat [37] or rabbit retinal ganglion cells [38], which is in line with our results presented for RGCs in rd10 retina. Second, we used very low current amplitudes (0.2 µA at 40 Hz for 0.01 mm^2 electrode area; and 0.4 µA at 40 Hz for 0.023 mm^2) to activate RGCs. The threshold charge density of 40 nC /mm^2 is about twenty times smaller than previously reported for epiretinal pulsatile stimuli (reviewed by [39])

using electrodes of similar size and about ten times smaller than charge densities evaluated for subretinal pulsatile stimuli (reviewed in [19]) and far below electrode or tissue damage thresholds. The total stimulation charge of ~ 1 nC required to reliably activate RGCs is in the same range of previously reported values for pulsatile millisecond-long stimuli [40, 41]. This indicates that RGCs are capable of integrating the stimulation over several milliseconds.

Third, we avoided the well-known problem of axonal stimulation in epiretinal configuration [17, 42, 43]. This result (Fig. 2A, Suppl. Figure 3) may contradict previous studies including our own work, where action potential initiation at the edge of the stimulation epiretinal electrode was demonstrated [43]. However, all previous studies used short square pulses, which instantaneously built up a strong "activating function" [44]. For smooth stimulus waveforms as used here, the activating function is small. The avoidance of axonal stimulation using long pulses has been shown using calcium imaging of RGC activity [14], although that technique does not allow resolution of individual axonal action potentials. We cannot exclude the possibility that sinusoidal stimulation with larger amplitude or stimulation area could evoke axonal stimulation.

Finally, we compare the results of spatial and contrast discrimination (Fig.4) to previous work. Spatial resolution based on grating stimuli has been estimated for subretinal stimulation of photoreceptor-degenerated rat retina to 48 µm [45], a value limited by the resolution of the stimulation array used there. The estimate was based on cortical visually evoked potentials, which does not allow us to infer the underlying retinal activity. The discrimination of 32 µm spatial shift of overlapping objects as obtained here (Fig. 4) would correspond in a human eye to a spatial resolution of 20/130, i.e. above legal blindness. Future in vivo studies need to confirm this hypothesis. For large objects (6°) a contrast discrimination of 10% could be achieved with an accuracy of 80 %. This value is superior to previous reports in blind rats [46] and in humans [5] but in the same range as inferred from the spike-time pattern of stimulated single RGC activity [47].

The high discrimination obtained here relies on logistic regression, a model which considers those cells, which change their response upon stimulation. Remarkably, the discrimination accuracy

varied considerably among experiments, even comprising different retinal portions from the same eye. Recently, it has been noted that the retinal degeneration reduces the consistency of retinal ganglion cell responses [48]. However, that effect was mediated by network activation, whereas here we clearly show a direct activation of RGCs in rd10. If the direct activation of RGCs in photoreceptor-degenerated retinas translates to the human retina, the reorganization of the presynaptic network [49] may play a minor role for artificial vision. The large variability of prediction accuracy could be due to the relatively small number of stimulated or recorded cells which encode stimulus identity in each retina.

The discrimination performance of changes in object position or object contrast was very good for large objects but poor for small objects. We assign this result to the low number of activated cells for small stimulus shapes. However, another contribution to this difference could be that a smaller stimulation area is associated with a weaker cell response and to a lower reliability (Figure 3B and Figure 2E). Increasing the charge density, especially considering the low charge threshold used here, could be the solution to improving the efficacy of stimulation for a small area. This suggests that an electrode size dependent charge threshold, could be a solution not only in subretinal (cit. Corna 2018) but also in epiretinal implants.

Conclusion:

With the presented approach, we discriminate with high accuracy RGC response to epiretinal sinusoidal stimulation with two spatially displaced objects or contrast within large objects.

From the technological point of view, stimulation of more objects of variable shape and sizes can be investigated using the CMOS-MEA, given the degree of freedom in selecting the stimulation spatial and temporal pattern provided by the array used here.

While we were able to remove several obstacles of artificial stimulation, many challenges such as cell-resolved bidirectional interfacing [50, 51] and cell-class specific stimulation [52] remain to be solved.

Supplementary:

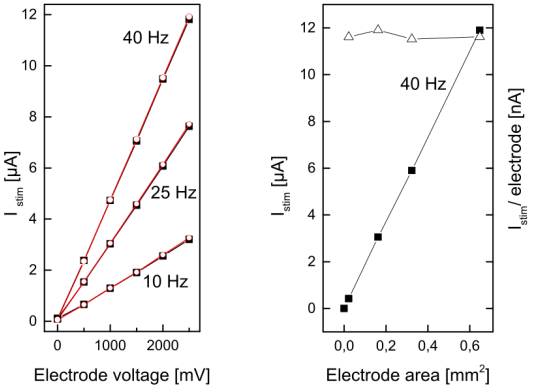

Supplementary Figure 1: Electrical characterization of the capacitive electrodes. Left: stimulation currents for applied voltage at different frequencies, with retina tissue (black lines) and without (red lines). Right: stimulation current (black markers) and stimulation current divided by electrode number (withe markers) for different electrode size.

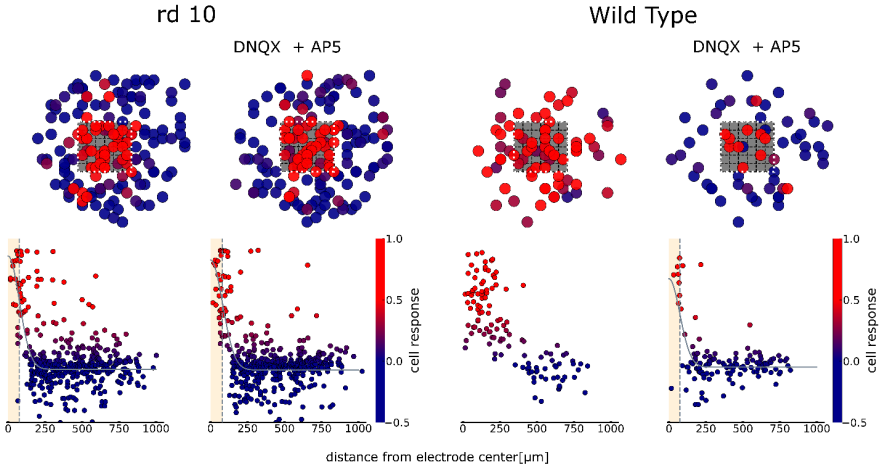

Supplementary Figure 2: differences between healthy and degenerated retina. Rd10 stimulation mechanism is direct, therefore there is no change in response after applying a synaptic blocker (DNQX +AP5). In WT, there is also a "network mediated" component that is blocked after drug application.

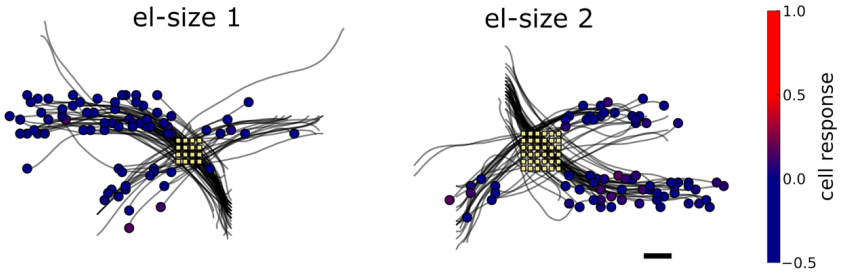

Supplementary Figure 3: Axonal stimulation. For the merged samples of figure 3, we calculated cell response for neurons with axon passing over the stimulation electrode. No axonal stimulation was detected. Scale bar 100µm.

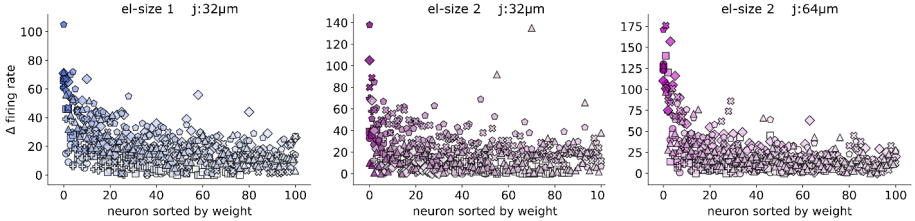

Supplementary Figure 4: Delta firing rate versus neurons sorted by weight, for the first 100 neurons. Color-coded the normalized weight.

References:

1. Edwards, T.L., et al., *Assessment of the Electronic Retinal Implant Alpha AMS in Restoring Vision to Blind Patients with End-Stage Retinitis Pigmentosa.* Ophthalmology, 2018.
2. Zrenner, E., et al., *Subretinal electronic chips allow blind patients to read letters and combine them to words.* Proceedings of the Royal Society B: Biological Sciences, 2011.
3. Palanker, D.V., et al., *Photovoltaic Restoration of Sight in Atrophic Age-Related Macular Degeneration: one-year follow-up.* Investigative Ophthalmology & Visual Science, 2020.
4. Jensen, R.J., et al., *Responses of ganglion cells to repetitive electrical stimulation of the retina.* J Neural Eng, 2007.
5. Stingl, K., et al., *Subretinal visual Implant Alpha IMS - Clinical trial interim report.* Vision Res, 2015.
6. Goetz, G.A., et al., *Electronic approaches to restoration of sight.* Rep Prog Phys, 2016.
7. Stingl, K., et al., *Interim Results of a Multicenter Trial with the New Electronic Subretinal Implant Alpha AMS in 15 Patients Blind from Inherited Retinal Degenerations.* Front Neurosci, 2017.
8. Flores, T., et al., *Honeycomb-shaped electro-neural interface enables cellular-scale pixels in subretinal prosthesis.* Scientific Reports, 2019.
9. Spencer, T.C., et al., *Spatial Restriction of Neural Activation Using Focused Multipolar Stimulation With a Retinal Prosthesis.* Investigative Ophthalmology & Visual Science, 2016.
10. Flores, T., et al., *Optimization of pillar electrodes in subretinal prosthesis for enhanced proximity to target neurons.* Journal of Neural Engineering, 2018.
11. Lorach, H., et al., *Photovoltaic restoration of sight with high visual acuity.* Nature Medicine, 2015.
12. Höfling, L., et al., *Probing and predicting ganglion cell responses to smooth electrical stimulation in healthy and blind mouse retina.* Scientific reports, 2020.
13. Rathbun, D.L., et al., *Spike-triggered average electrical stimuli as input filters for bionic vision perspective.* Journal of Neural Engineering, 2018.
14. Weitz, A.C., et al., *Improving the spatial resolution of epiretinal implants by increasing stimulus pulse duration.* Sci Transl Med, 2015.
15. Freeman, D.K., et al., *Selective Activation of Neuronal Targets With Sinusoidal Electric Stimulation.* Journal of Neurophysiology, 2010.
16. Ho, E., et al., *Spatiotemporal characteristics of retinal response to network-mediated photovoltaic stimulation.* Jurnal of neurophysiology, 2018.
17. Grosberg, L.E., et al., *Activation of ganglion cells and axon bundles using epiretinal electrical stimulation.* Jurnal of neurophysiology, 2017.
18. Bertotti, G., et al., *A CMOS-based sensor array for in-vitro neural tissue interfacing with 4225 recording sites and 1024 stimulation sites*, in *Biomedical Circuits and Systems Conference (BioCAS), 2014 IEEE*. 2014, IEEE. p. 304-307.
19. Corna, A., et al., *Electrode-size dependent thresholds in subretinal neuroprosthetic stimulation.* Journal of neural engineering, 2018.
20. Leibig, C., et al., *Unsupervised neural spike sorting for high-density microelectrode arrays with convolutive independent component analysis.* Journal of Neuroscience Methods, 2016.
21. Eickenscheidt, M., et al., *Electrical stimulation of retinal neurons in epiretinal and subretinalconfiguration using a multicapacitor array.* Jurnal of neurophysiology, 2012.

22. Dollt, M., et al., *Low-Temperature Atomic Layer Deposited Oxide on Titanium Nitride Electrodes Enables Culture and Physiological Recording of Electrogenic Cells.* Frontier in Neuroscience, 2020.
23. McCullagh, P., et al., *Generalized Linear Models (2nd ed.).* 1989.
24. Virtanen, P., et al., *SciPy 1.0: fundamental algorithms for scientific computing in Python* Nature methods, 2020.
25. Cessie, S.L., et al., *Ridge Estimators in Logistic Regression.* Journal of the Royal Statistical Society. Series C (Applied Statistics) 1992.
26. Hierlemann, A., *Direct interfacing of neurons to highly integrated microsystems*, in *Micro Electro Mechanical Systems (MEMS), 2017 IEEE 30th International Conference on*. 2017, IEEE. p. 199-204.
27. Stutzki, H., et al., *Inflammatory stimulation preserves physiological properties of retinal ganglion cells after optic nerve injury* Frontiers in Cellular Neuroscience, 2014.
28. Cho, A., et al., *Changes in ganglion cell physiology during retinal degeneration influence excitability by prosthetic electrodes.* Journal of Neural Engineering, 2016.
29. Freeman, D.K., et al., *Multiple components of ganglion cell desensitization in response to prosthetic stimulation.* Jurnal of Neural Engineering, 2011.
30. Fornos, A.P., et al., *Dynamics of Visual Perception Upon Electrical Stimulation of the Retina* Investigative Ophthalmology & Visual Science, 2010.
31. Jeon, C.-J., et al., *The Major Cell Populations of the Mouse Retina.* Journal of Neuroscience, 1998.
32. Cruz, L.d., et al., *Five-year safety and performance results from the Argus II Retinal Prosthesis System clinical trial.* Ophthalmology, 2016.
33. Schwartz, G., et al., *Low error discrimination using a correlated population code.* Jurnal of neurophysiology, 2012.
34. Yuan, X., et al., *Versatile live-cell activity analysis platform for characterization of neuronal dynamics at single-cell and network level.* Nature Communications 2020.
35. Ronchi, S., et al., *Single-Cell Electrical Stimulation Using CMOS-Based High-Density Microelectrode Arrays.* Frontiers in Neuroscience, 2019.
36. Fornos, A.P., et al., *Temporal Properties of Visual Perception on Electrical Stimulation of the Retina* Investigative Ophthalmology & Visual Science May, 2012.
37. Kotsakidis, R., et al., *In vitro assessment of the differences in retinal ganglion cell responses to intra- and extracellular electrical stimulation.* J Neural Eng, 2018.
38. Twyford, P., et al., *The Retinal Response to Sinusoidal Electrical Stimulation.* IEEE Transactions on Neural Systems and Rehabilitation Engineering, 2015.
39. Sekirnjak, C., et al., *Electrical stimulation of mammalian retinal ganglion cells with multielectrode arrays.* Journal of Neurophysiology, 2006.
40. Samba, R., et al., *PEDOT–CNT coated electrodes stimulate retinal neurons at low voltage amplitudes and low charge densities.* Journal of Neural Engineering, 2015.
41. Stett, A., et al., *Electrical multisite stimulation of the isolated chicken retina.* Vision Research, 2000.
42. Beyeler, M., et al., *A model of ganglion axon pathways accounts for percepts elicited by retinal implants.* Scientific Reports, 2019.
43. Eickenscheidt, M., et al., *Action potentials in retinal ganglion cells are initiated at the site of maximal curvature of the extracellular potential.* J Neural Eng, 2014.
44. Rattay, F., *The basic mechanism for the electrical stimulation of the nervous system.* Neuroscience, 1999.
45. Ho, E., et al., *Characteristics of prosthetic vision in rats with subretinal flat and pillar electrode arrays.* Journal of Neural Engineering, 2019.

46. Goetz, G., et al., *Contrast Sensitivity With a Subretinal Prosthesis and Implications for Efficient Delivery of Visual Information* Investigative Ophthalmology & Visual Science, 2015.
47. Ho, E., et al., *Temporal structure in spiking patterns of ganglion cells defines perceptual thresholds in rodents with subretinal prosthesis.* Scientific reports, 2018.
48. Yoon, Y.J., et al., *Retinal Degeneration Reduces Consistency of Network-Mediated Responses Arising in Ganglion Cells to Electric Stimulation.* IEEE Transactions on Neural Systems and Rehabilitation Engineering, 2020.
49. Marc, R.E., et al., *Neural remodeling in retinal degeneration* Progress in Retinal and Eye Research, 2003.
50. Zeck, G., et al., *Noninvasive neuroelectronic interfacing with synaptically connected snail neurons immobilized on a semiconductor chip.* PNAS, 2001.
51. Shah, N.P., et al., *Computational challenges and opportunities for a bi-directional artificial retina.* Journal of Neural Engineering, 2020.
52. Oesterle, J., et al., *Bayesian inference for biophysical neuron models enables stimulus optimization for retinal neuroprosthetics.* eLife, 2020.

4 HDAC INHIBITION AMELIORATES CONE SURVIVAL IN RETINITIS PIGMENTOSA MICE

AUTHORS Marijana Samardzija[1], Andrea Corna[1], Raquel Gomez-Sintes[1], Mohamed Ali Jarboui, Angela Armento , Jerome E. Roger, Eleni Petridou, Wadood Haq, Francois Paquet-Durand, Eberhart Zrenner, Pedro de la Villa, Günther Zeck, Christian Grimm, Patricia Boya, Marius Ueffing and Dragana Trifunović

PUBLISHED Cell Death & Differentiation, November 2020.
https://doi.org/10.1038/s41418-020-00653-3

The work is result of a collaboration of different research group, coordinated by Dr. Trifunović (DT). DT designed the study. Preparation and treatment of retinal explant cultures were performed by DT and histology and in situ activity assay by DT and EP. *In vivo* treatment was performed by MS, CG and DT. All the parts dealing with open field behavioral test and ERG recording were carried out by the group of PB (RG-S, PV and PB). DT performed whole transcriptome sequencing and MJ, JR and DT analyzed the data. AA performed qPCR. All authors helped with the writing of the manuscript and scientific discussion. All parts dealing with the MEA electrophysiological investigation of organotypic retina cultures were carried out by me with the help of GZ and DT Together with GZ and DT, and the contribution of EZ, I developed experimental protocol to evaluate the effects of HDAC inhibition

1 Shared first author

on functional light response. DT provided the tissue. I performed the MEA recoding including all the steps of data analysis and visualization.

Cell Death & Differentiation
https://doi.org/10.1038/s41418-020-00653-3

Cell Death & Differentiation

ARTICLE

HDAC inhibition ameliorates cone survival in retinitis pigmentosa mice

Marijana Samardzija[1] · Andrea Corna[2,3,4] · Raquel Gomez-Sintes[5] · Mohamed Ali Jarboui[3] · Angela Armento[3] · Jerome E. Roger[6] · Eleni Petridou[3,8] · Wadood Haq[3] · Francois Paquet-Durand[3] · Eberhart Zrenner[3] · Pedro de la Villa[7] · Günther Zeck[2] · Christian Grimm[1] · Patricia Boya[5] · Marius Ueffing[3] · Dragana Trifunović[3]

Received: 19 June 2020 / Revised: 12 October 2020 / Accepted: 15 October 2020

Abstract

Cone photoreceptor cell death in inherited retinal diseases, such as Retinitis Pigmentosa (RP), leads to the loss of high acuity and color vision and, ultimately to blindness. In RP, a vast number of mutations perturb the structure and function of rod photoreceptors, while cones remain initially unaffected. Extensive rod loss in advanced stages of the disease triggers cone death by a mechanism that is still largely unknown. Here, we show that secondary cone cell death in animal models for RP is associated with increased activity of histone deacetylates (HDACs). A single intravitreal injection of an HDAC inhibitor at late stages of the disease, when the majority of rods have already degenerated, was sufficient to delay cone death and support long-term cone survival in two mouse models for RP, affected by mutations in the phosphodiesterase 6b gene. Moreover, the surviving cones remained light-sensitive, leading to an improvement in visual function. RNA-seq analysis of protected cones demonstrated that HDAC inhibition initiated multi-level protection via regulation of different pro-survival pathways, including MAPK, PI3K-Akt, and autophagy. This study suggests a unique opportunity for targeted pharmacological protection of secondary dying cones by HDAC inhibition and creates hope to maintain vision in RP patients even in advanced disease stages.

Introduction

In Retinitis Pigmentosa (RP), the leading cause of inherited blindness, mutations in more than 90 genes affect the survival and/or function of rod photoreceptors or retinal pigment epithelium cells (RPE) (http://www.sph.uth.tmc.edu/Retnet/home.htm). One of the particularities of RP is that despite being mutation-unaffected, cone photoreceptors die secondarily once most rods are lost [1]. In humans, loss of rods initially has only minor consequences for vision, and the majority of patients are

These authors contributed equally: Marijana Samardzija, Andrea Corna, Raquel Gomez-Sintes

Edited by E. Baehrecke

Supplementary information The online version of this article (https://doi.org/10.1038/s41418-020-00653-3) contains supplementary material, which is available to authorized users.

✉ Dragana Trifunović
dragana.trifunovic@uni-tuebingen.de

[1] Lab for Retinal Cell Biology, Department of Ophthalmology, University of Zürich, Zürich, Switzerland

[2] Department of Neurophysics, NMI Natural and Medical Sciences Institute at the University of Tübingen, Reutlingen, Germany

[3] Institute for Ophthalmic Research, Eberhard Karls Universität Tübingen, Tübingen, Germany

[4] Graduate School of Neural Information Processing/International Max Planck Research School, Tübingen, Germany

[5] Department of Cellular and Molecular Biology, Centro de Investigaciones Biológicas Margarita Salas, CSIC, Madrid, Spain

[6] Paris-Saclay Institute of Neuroscience, CERTO-Retina France, CNRS, Univ Paris Sud, Université Paris-Saclay, Saint-Aubin, France

[7] Universidad de Alcala de Henares, Madrid, Spain

[8] Present address: Institute of Neuronal Cell Biology, Technische Universität München, München, Germany

unaware of their condition until they start experiencing a prominent reduction in the central visual field, acuity, or color discrimination, due to the loss of cones. Hence, in a clinical setting, it is highly pertinent to develop therapies to treat advanced stages of RP, when the majority of rods have already degenerated, and cone degeneration has set in [2].

Despite the importance of cones for human vision, studies on therapeutic options to prevent their loss at advanced stages of RP are disproportionally low [1, 3–6] due to the intercellular relationship between rod and cone photoreceptors in human and mouse retina, where cones represent less than 5% of all photoreceptors [7]. Moreover, current knowledge suggests that the massive loss of rods in late RP creates a "point of no return", after which cone cell death is unstoppable [2, 8], as cones are suffering from the loss of structural and nutritional support from rods [1, 9], exposure to oxidative stress [4], and inflammation [3, 6]. Although alleviating each of these processes individually has the potential to preserve cones to some extent [1, 3, 5, 10], an ideal therapeutic option should provide multi-level protection of cones in the rod-depleted retina. One way to achieve this could be by an epigenetically driven simultaneous regulation of several genes involved in diverse pro-survival responses.

Histone deacetylases (HDACs) are regulators of the chromatin structure, and changes in their activity affect transcription of a number of genes [11]. Tightly packed chromatin, following the HDAC-governed removal of acetyl groups from histones, is generally associated with transcriptional silencing, albeit this largely depends on the type and "health" status of cells [12]. Aberrant HDAC activity is causatively linked to various diseases ranging from cancer, to neurodegenerative diseases [12, 13]. We and others have previously shown that epigenetic regulation, via HDAC inhibition, can protect primary degenerating photoreceptors in inherited retinal dystrophies caused by mutations in different genes [14–17]. Consequently, more than 90 clinical trials involving HDAC regulators stress HDAC inhibition as a promising therapeutic approach for various diseases, including retinal dystrophies [12, 18].

Here, we investigated the involvement of HDACs in secondary cone degeneration in mouse models of RP. We found an increased HDAC activity present in both mutation-affected rods and in secondary dying cones. A single intravitreal injection of the HDAC inhibitor Trichostatin A (TSA) afforded long-term preservation of cone photoreceptors. Transcriptional changes associated with cone survival comprised regulation of distinct pro-survival mechanisms, including autophagy, MAPK, and PI3K/Akt regulation. Thus, therapies based on HDAC inhibition can offer a unique possibility to attenuate the loss of photoreceptors independent of the stage of degeneration.

Materials and methods

Animals

The C3H *rd1/rd1 (rd1)*, C57BL/6J x C3H *HR2.1:TN-XL x rd1 (rd1$^{TN\text{-}XL}$)*, C57BL/6J *rd10/rd10 (rd10)*, and C57BL/6J wild-type (wt) mice were housed under standard light conditions, had free access to food and water, and were used irrespective of gender. *rd1$^{TN\text{-}XL}$* mice express the TN-XL (Ca^{2+} biosensor) selectively in cone photoreceptors under the control of the human red opsin promoter (HR2.1) [19, 20]. The presence of TN-XL biosensor does not alter the *rd1* phenotype, while it enables direct visualization of cone photoreceptors by fluorescence microscopy [20]. All procedures were performed in accordance with the ARVO statement for the Use of Animals in Ophthalmic and Vision Research, the regulations of the Tuebingen University committee on animal protection, Germany, veterinary authorities of Kanton Zurich, Switzerland and the ethics committees of the CSIC and the Comunidad de Madrid.

Intravitreal injections

Single intravitreal injections were performed at postnatal day (PN) 19 in *rd1$^{TN\text{-}XL}$* and PN42 in *rd10* mice, as previously described [14]. Mice were anesthetized subcutaneously with a mixture of ketamine (85 mg/kg) and xylazine (4 mg/kg). One eye was injected with 0.5 µl of a 100 nM TSA (catalog T8552, Sigma-Aldrich, St. Louis, MO) in 0.0001% DMSO, while the contralateral eye was sham-injected with 0.0001% DMSO and served as a control. Assuming the intraocular volume of mouse eye to be 5 µl [21], this procedure resulted in a final intraocular concentration of 10 nM TSA. For the open field behavioral test, *rd10* littermates were TSA- or sham-injected bilaterally at PN42.

Retinal explant cultures

Organotypic retinal cultures from *rd1$^{TN\text{-}XL}$* animals, including the retinal pigment epithelium (RPE) were prepared under sterile conditions as previously described [14, 15]. PN19 or PN21 *rd1$^{TN\text{-}XL}$* animals were sacrificed, the eyes enucleated and pretreated with 0.12% proteinase K (ICN Biomedicals Inc.) for 15 min at 37 °C in HBSS (Invitrogen Inc.). Proteinase K activity was blocked by the addition of 10% fetal bovine serum, followed by rinsing in HBSS. Next, the cornea, lens, sclera, and choroid were removed, while the RPE remained attached to the retina. The explant was cut into a clover-leaf shape and transferred to a culture membrane insert (Corning Life Sciences) with the RPE facing the membrane. The membrane inserts were placed into six-well culture plates with Neurobasal-A

medium (catalog 10888022) supplemented with 2% B27 (catalog 0080085-SA), 1% N2 (catalog 17502048), and L-glutamine (0.8 mM, catalog 25030032) (all from Invitrogen Inc.), and incubated at 37 °C in a humidified 5% CO2 incubator. The culture medium was changed every 2 days during the 7 days culturing period. Retinal explants were treated with 10 nM TSA, 1 µM Panobinostat (catalog S1030, Selleckchem), 20 µM LY294002 (catalog S1105, Selleckchem), and 10 µM U0126-EtOH (catalog S1102, Selleckchem) diluted in Neurobasal-A culture medium. For the PI3K-Akt and MAPK inhibition experiments, cultures were treated with TSA, LY294002, U0126, TSA + LY294002, and TSA + U0126 only for 2 days followed by the culture medium without compounds for additional 5 days. For controls, the same amounts of DMSO were diluted in the culture medium. Culturing was stopped after 7 days by 2 h fixation in 4% PFA, cryoprotected with graded sucrose solutions containing 10, 20, and 30% sucrose and then embedded in tissue freezing medium (Leica Microsystems Nussloch GmbH).

Quantification of cone survival

The quantification of cones was performed by manually counting the number of TN-XL labeled cones (using the Zen event counter) on at least two retinal cross-sections cut along the dorsoventral axis, at the level of the optic nerve. Retinal cross-sections were used to quantify cone photoreceptors as the TN-XL biosensor is present throughout the cone photoreceptor, except the outer segment (IS) [19]. The presence of the biosensor in the cell body, axon and IS, hampers a clear separation of individual cell bodies from the IS and/or axon on flat-mount preparations at the late stages of *rd1*$^{TN\text{-}XL}$ degeneration, where cones align horizontally to the INL due to the lack of structural support from rods (SI Appendix, Fig. S1A.) Retinal cross-sections with labeled nuclei enabled distinction between different parts of the cones and facilitated the counting of their cell bodies. Colabeling of *rd1*$^{TN\text{-}XL}$ cones with a cone-specific antibody, cone arrestin (CAR), showed full overlap between two fluorescent signals confirming the specificity of TN-XL labeling both in degenerating and protected cones (SI Appendix, Fig. S2). Cones were quantified on multiple images projection (MIP) obtained from 9–15 optical sections taken with 20x magnification at four positions in the retina: ventral and dorsal central retina (corresponding to −10° and 10° of eccentricity from the optic nerve, respectively) and ventral and dorsal peripheral positions at −80° and 80° degrees (SI Appendix, Fig. S1). For the quantification of cone survival in *rd10* retinas, cones were labeled with an antibody against cone arrestin. Spider diagrams show the number of cones per 100 µm of the outer nuclear layer (ONL) length at each position, presented as mean values ± SEM.

Histology

For retinal cross-sectioning, the eyes were marked nasally, and eyecups (after cornea, iris, lens, and vitreous removal) were fixed in 4% paraformaldehyde for 2 h at room temperature. Following graded sucrose cryoprotection eyes were embedded in optimal cutting temperature compound (Tissue-Tek), cut into 12 µm sections, and mounted with Vectashield medium containing 4',6-diamidino-2-phenylindole (DAPI, Vector). For retinal flat mounts, retinas without RPE were fixed for 30 min, cut into a cloverleaf shape, and mounted with Vectashield with the photoreceptors facing up. To analyze retinal morphology, eyes were fixed in 2.5% glutaraldehyde, cut at the optic nerve level, followed by 1% osmium tetroxide treatment post-fixation and ethanol dehydration, according to a previously described protocol [22]. After embedding in Epon 812, 0.5 µm thick sections were counterstained with toluidine blue. Immunostaining was performed on retinal cryosections by incubating with primary antibodies against rabbit cone arrestin (1:1000; catalog AB15282, Merck Chemicals GmbH), mouse anti-rhodopsin (1:400, catalog MAB 5316, Chemicon), LC3B (1:100, catalog NB-100-220, Novus) and LAMP1 (1:100, clone 1D4B, DSHB) at 4 °C overnight. Alexa Fluor 488, 568, or 647-conjugated antibodies were used as secondary antibodies. Images were captured using Z-stacks on a Zeiss Axio Imager Z1 ApoTome Microscope using 20x air, 40x oil, or 100x oil objectives. For the quantification of the LC3 and LAMP1 puncta in cones, 4 images per retina for in vivo treatment and 8 images per explant were assessed in each confocal plane obtained by the Leica TCS SP5 Confocal Microscope. Colocalizing puncta were counted using the counter plugin of Image J. The number of colocalizing puncta was divided by the number of cones in the whole z-stack.

HDAC in situ activity assay

HDAC activity assays were performed on 12 µm thick cryosections of 4% PFA- fixed eyes following immunostaining against cone arrestin/rhodopsin as previously described [14]. Briefly, retina sections were exposed to 200 µM Fluor de Lys-SIRT2 deacetylase substrate (Biomol) with 500 µM NAD + (Biomol) in assay buffer (50 mM Tris/HCl, 137 mM NaCl; 2.7 mM KCl; 1 mM MgCl2; pH 8.0) for 3 h at room temperature. Following methanol fixation at -20 °C for 20 min, a developer solution (1x Biomol; KI105) containing 2 µM TSA and 2 mM nicotinamide in assay buffer was applied to generate the signal. Due to the presence of a background staining in negative controls, only cells with prominent nuclear staining were considered as HDAC positive [14].

MEA recording

Retina explant cultures attached to the membrane were transferred from the incubation chamber to a 256-electrode MEA (Multi channel systems MCS GmbH, Reutlingen, Germany) with the ganglion cell side facing the electrodes. A custom-made grid was placed over the retina to improve the contact between electrodes and the tissue and the stability of the recording. Cultures were perfused throughout the experiment with oxygenated Ames' medium (A1420, Sigma-Aldrich) and heated to 36 °C. The electrode spacing was 200 µm, with the total recordings area of ~3.2 × 3.2 mm^2. Twenty repetitions of 350 ms long light-flashes of increasing intensity (8.6 e12, 5.3 e13, 3 e14, 8.7 e14, 1.6 e15, 2.3 e15 photons/cm^2 s) separated by 2 s of dark were presented to both control and the TSA-treated retinal explants mounted on MEA. The recordings were made with a sampling rate of 25 kHz using the MC Rack software (Multi Channel Systems MCS GmbH). The analysis of recordings from 256-MEAs was performed using Python 3.6. Recordings were bandpass - filtered (400–5000 Hz, Butterworth 2nd order), and spikes were detected as threshold crossing of 5 times the standard deviation of the filtered signal with a pause time of 1.5 ms. Light-induced RGCs activation recorded by an electrode was quantified for each light intensity using a two-tailed, paired *t*-test comparing the detected spikes during the 20 repetitions of light-ON (350 ms of light flash) or light-OFF (350 ms after the light shut-off) versus the spontaneous activity recorded before light onset. Only electrodes with a statistically significant difference ($p < 0.01$ and t-statistic > 2) were considered light-activated. In addition, only channels light-activated for at least 3 out of 5 light intensities in the photopic light range (5.3 e13, 3 e14, 8.7 e14, 1.6 e15, 2.3 e15 photons/cm^2) were included in the analysis. These criteria were used to eliminate potential non-stable recordings. To quantify the degree by which light onset changes the spontaneous firing rate and to avoid an overestimation of the electrodes recording low spontaneous activity, a response ratio was calculated. The calculation is based on the well-established bias index used to quantify physiological light responses [23, 24] and is analogous to the Michelson contrast used to quantify the contrast in visual images:

Response ratio = (Firing rate LIGHT ON − Firing rate spontaneous)/(Firing rate LIGHT ON + Firing rate spontaneous).

Open field behavioral test

The open field test is based on natural mouse behavior to avoid brightly lit open spaces [25]. This test was performed based on the previously described procedure with minor modifications [26]. A custom-made box for light/dark transition test (60 × 30 × 30 cm) was divided into two chambers, one black and one white, connected by a door (5 × 5 cm). The mice were habituated in the dark for at least 1 h before the testing. The light chamber was illuminated from the top by white diodes (670 lux, LitePad® HO90, Rosco). Mice were placed into the dark compartment, and the door was opened after 3 s. Mice were allowed to move freely between the two chambers with the door open for 5 min. The time spent in the dark chamber was registered by an experimenter. After each trial, all chambers were disinfected to prevent a bias based on olfactory cues.

ERG recordings

Mice were dark adapted overnight, and subsequent manipulations were performed in dim red light. Mice were anesthetized with intraperitoneal injections of ketamine (95 mg/kg) and xylazine (5 mg/kg) solution and maintained on a heating pad at 37 °C. Pupils were dilated with a drop of 1% tropicamide. To optimize electrical recording, a topical drop (2% Methocel) was applied to each eye immediately before placing the corneal electrode. Flash-induced ERG responses were recorded from the right eye in response to light stimuli produced with a Ganzfeld stimulator. Light intensity was measured with a photometer at the level of the eye (Mavo Monitor USB). Four to 64 consecutive stimuli were averaged with an interval between light flashes in scotopic conditions of 10 s for dim flashes and up to 60 s for the highest intensity. Under photopic conditions, the interval between light flashes was fixed at 1 s. ERG signals were amplified and band-filtered between 0.3 and 1000 Hz with an amplifier (CP511 AC amplifier). Electrical signals were digitized at 20 kHz with a power laboratory data acquisition board (AD Instruments). Under dark adaptation, scotopic threshold responses (STR) were recorded to light flashes of −4 log cd·s·m^{-2}; rod responses were recorded to light flashes of −2 cd·s·m^{-2}, and mixed responses were recorded in response to light flashes of 1.5 log cd·s·m^{-2}. Oscillatory potential (OP) was isolated using white flashes of 1.5 log cd·s·m^{-2} in a recording frequency range of 100–10,000 Hz. Under light adaptation, cone-mediated responses to light flashes of 2 log cd·s·m^{-2} on a rod-saturating background of 30 cd·m^{-2} were recorded. Wave amplitudes of the STR, rod responses (b-rod), mixed responses (a-mixed and b-mixed), and OP were measured offline by an observer masked to the experimental condition of the animal.

Flow-sorting of the cone photoreceptors

A protocol from Palfi et al. [27]. was used to dissociate retinal cells. Briefly, PN19-26 control and TSA-treated retinal explant cultures were removed from membranes and

incubated in trypsin (Sigma-Aldrich) solution for 20 min at 37 °C. Following incubation with trypsin inhibitor (Sigma-Aldrich), cell suspension was washed with HBSS and passed through a 40-µm filter before fluorescence activated sorting (FACS). One biological replicate included at least 2 retinal explants prepared from different animals. Three independent biological replicates from control and TSA-treated retinal explants were used for cone photoreceptor FACS using an ARIAIII cell sorter (BD Biosciences). The sort was performed with a 100 µm nozzle tip, at a sheath pressure of 20.0 psi, and with purity precision. TN-XL positive cone photoreceptors were gated as follows: singlets forward scatter (FSC-A vs FSC-H)/singlets side scatter (SSC-A *vs*. SSC-H)/viable cells (FSC-A *vs*. SSC-A)/TN-XL + cells (FSC-A *vs*. TN-XL-A) (gating Fig. S5A, B). The purity of sorted TN-XL + cells was checked by performing post-sort FACS analysis (Fig. S5C, D).

Whole transcriptome sequencing and data analysis

2000–5000 frozen sorted-cells were lysed in ~10 µl of lysis buffer, and cDNA synthesis was performed using the SMART-Seq v4 Ultra Low Input RNA Kit (catalog 634888, Takara Bio). First-strand cDNA synthesis was performed using 20–50% of the input, and was followed by full-length double-strand cDNA amplification using 17 PCR cycles. The quality of the resulting cDNA was validated using Bioanalyzer and High Sensitivity DNA Kit (Agilent), and Qubit dsDNA HS fluorometric quantification (Thermo-Fisher Scientific). NGS libraries were prepared using 150 pg of cDNA input and the Nextera XT DNA Library Preparation Kit (catalog FC-131-1024, Illumina) with 11 cycles of PCR. Libraries were sequenced as single reads (75 bp read length) on a NextSeq500 (Illumina) with a depth of >20 million reads. Library preparation and sequencing procedures were performed by the same individual, and a design to minimize technical batch effects. Data quality of raw RNA-seq reads in FASTQ files was assessed using ReadQC (ngs-bits version 2018_04) to identify potential sequencing cycles with low average quality and base distribution bias. Reads were preprocessed with Skewer (version 0.2.2) and aligned using STAR (version 2.5.4a), allowing spliced read alignment to the mouse reference genome (Ensembl Mus musculus GRCm38). Alignment quality was analyzed using MappingQC (ngs-bits version 2018_04) and visually inspected with Broad Integrative Genome Viewer (version 2.4.0). Based on the genome annotation ITAG (Ensembl 75), normalized read counts for all genes were obtained using subread (version 1.6.0) and edgeR (version 3.28.0). Raw counts data were processed using iDEP, an integrated web application for RNA-seq data analysis [28]. To provide access to RNAseq data, we generated a BioJupies notebook [29] link providing an interactive and visual analysis of all the data (https://amp.pharm.mssm.edu/biojupies/notebook/LjknTl51J). Sequencing data are deposited on GEO with the accession number GSE141601.

For differential gene expression (DEG) analysis, gene counts were filtered to only retain genes with a value > 1 cpm (count per million), in at least two samples within at least one group (control or treated), leaving around 14,400 genes for determination of differential expression in each of the pair-wise comparisons between experimental groups. Differentially expressed genes between treated and control groups were identified using the two-tailed permutation FDR-based Student's *t* test (FDR < 0.05 and 250 randomizations). Only transcripts coding for protein sequences were retained for pathway analysis. Quantitative gene expression data was submitted and integrated into the PaintOmics 3 data analysis platform [30, 31], in order to identify trends in pathway modulation following the TSA treatment. A stable link is provided to access and visualize the results (http://www.paintomics.org/?jobID=4CIbSr1eA4).

Quantitative RT-PCR

For qRT-PCR, 2000–6000 cones from two pooled PN19-26 ex vivo $rd1^{TN\text{-}XL}$ explants were sorted in 350 µl RLT buffer (Qiagen) to lyse cells. RNA extractions were performed using an RNeasy Micro Kit (Qiagen), followed by cDNA synthesis using the QuantiTect Reverse Transcription Kit (Qiagen). qRT-PCR reactions were performed in technical duplicates of 4 biological samples of TSA-treated and control retinas, on BioRad CFX96 real-time system using QuantiTect SYBR Green PCR Kit (Qiagen) along with gene specific forward (fwd) and reverse (rev) primers (250 nM). The sequences of the primer sets used are listed in supporting Table S1. The PCR protocol included 40 cycles of: 94 °C (15 s), 57 °C (30 s), and 72 °C (30 s). Relative mRNA expression of each gene of interest was calculated using ΔΔCT method and GAPDH as a housekeeping gene.

Statistics

All data were analyzed using Excel (Microsoft) and GraphPad Prism 6. For each comparison between control and treated groups, normal distribution was determined with GraphPad software (D'Agostino & Pearson omnibus and Shapiro–Wilk normality tests). When applicable (methodology based) investigators were blinded for the condition. Quantification of in vivo survival for every time points, for different positions, was calculated using two-way ANOVA. The overall temporal survival curve shown in Fig. 2R was obtained by averaging all the analyzed positions from all the animals per stage. The statistical significance in the

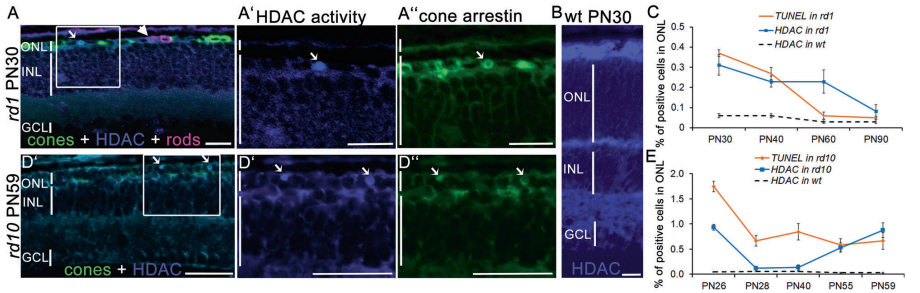

Fig. 1 Increased HDAC activity in RP photoreceptors at advanced stages of degeneration. A–A" HDAC in situ activity assay in *rd1* retinal cross-sections at PN30. HDAC activity (blue) was present in both rod (magenta, arrowhead, rhodopsin immunostaining) and cone photoreceptors (green, arrow, cone arrestin immunostaining). **A'** Magnification of the marked region indicating HDAC+ cell colocalizing with cone arrestin (**A"**). **B** HDAC activity in wild-type retina at PN30. **C** Percentage of TUNEL+ and HDAC+ cells in the ONL of *rd1* and wt mice over time. **D–D"** Representative image of a colocalization of HDAC activity and cone arrestin in *rd10* mice at PN59, with only cones remaining in the ONL. **E** Percentage of TUNEL+ and HDAC+ cells in the ONL of *rd10* and wt mice over time. Data are shown as mean ± SEM ($n = 3$–5 animals per age). Scale bars: 50 µm. ONL outer nuclear layer, INL inner nuclear layer, GCL ganglion cell layer, PN post-natal day.

broadening of the survival curves was assessed *via* shared control Cummings estimation plot using the DABEST package in R with 5000 bootstraps resamples (https://www.estimationstats.com/) [32]. A shared-control estimation plot represents the Hedges' *g* comparison of log2-transformed cone survival ratios. Since TSA treatment prevented $rd1^{TN\text{-}XL}$ cone loss up to 7 days post-injection, the cone survival ratio at PN26 was used as the control and compared to the survival ratio at PN30, PN37, PN45, PN60 and PN90. The statistical significance of Hedges' *g* difference was determined by unpaired two-sided permutation *t*-test.

Ex vivo survival was quantified on 5–12 different positions, from 3–5 retinal cross-sections obtained from different positions within a retinal explant. Unpaired, two-tailed *t*-tests were used to compare controls with treatments.

Statistical differences for LC3-LAMP1 puncta quantification and qRT-PCR were calculated using Mann–Whitney nonparametric test.

RNAseq raw data were processed and normalized using subread (version 1.6.0) and edgeR (version 3.28.0). Statistical data analysis was carried out using the Perseus tool suite for Omics data analysis [33]. Two-tailed, unpaired permutation-based FDR Students' *t* test on biological replicates' mean difference was applied (FDR < 0.05 and 250 randomizations). Log2 fold changes, mean differences, and *p* values are reported in the Gene expression dataset.

The statistical difference of light-induced response ratio between control and treated retinas was calculated using a Wilcoxon rank-sum test.

Statistical difference of open field behavioral test was calculated using a two-way ANOVA test.

Results

Secondary cone degeneration in RP is associated with an increased HDAC activity

To assess the involvement of HDACs in the secondary cone degeneration, we used an HDAC in situ activity assay [16] at advanced stages of photoreceptor degeneration in two mouse models for RP, the *rd1* and *rd10* mice. Different mutations in the rod-specific phosphodiesterase 6b (*Pde6b*) gene lead to fast rod photoreceptor degeneration, with the onset at PN9 in *rd1* and PN14 in *rd10* mice [15, 34, 35]. Cone degeneration begins once most rods have degenerated, around PN20 in the *rd1* and PN40 in the *rd10* mouse [1, 3]. At PN30, the outer nuclear layer (ONL) in *rd1* mice is reduced to only one row of photoreceptors, almost exclusively cones (Fig. 1A).

A combination of in situ HDAC activity assay with cone- and rod-specific immunostaining confirmed previously established association of increased HDAC activity and rod degeneration (Fig. 1A) [15, 16]. Interestingly, HDAC activity also colocalized with the cones, once the majority of rods have degenerated (Fig. 1A–A") [1]. The presence of HDAC positive cells within the ONL was detected through the entire period of cone cell death in *rd1* mice (Fig. 1C), while no positive signal for HDAC activity was detected in nuclei of wild-type mice at PN30 (Fig. 1B). Moreover, late stages of *rd10* degeneration also displayed increased HDAC activity, mirroring the timeline of photoreceptor cell death in the *rd10* mouse, characterized by massive rod loss up to PN26 [35], followed by continuous photoreceptor cell death, likely reflecting the simultaneous rod and cone loss (Fig. 1D, E). These findings suggest that the cell

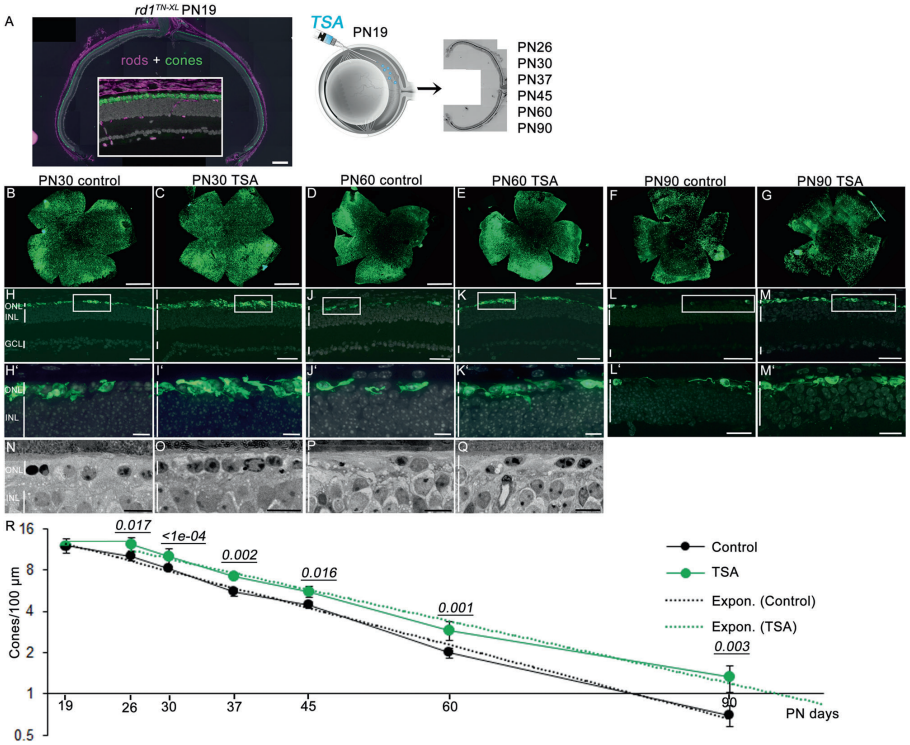

Fig. 2 HDAC inhibition promotes long-term cone survival in *rd1*$^{TN\text{-}XL}$ mice. A Retinal cross-section of an *rd1*$^{TN\text{-}XL}$ mouse at PN19, showing TN-XL-labeled cones (green), rods (magenta, anti-rhodopsin antibody), and nuclei (gray, DAPI). Note that the mouse secondary antibody used to detect anti-rhodopsin antibodies showed the non-specific signal in layers other than ONL. Schematic representation of a single intravitreal injection of TSA at PN19, followed by quantification of cone survival up to PN90. **B**–**G** Flat mounted retinas from control and TSA-treated eyes at indicated PN days. **H**–**M** Representative images of retinal cross-sections from control and TSA-treated retinas at PN30, PN60 and PN90 used to quantify of TN-XL labeled cones. **H'**–**M'** Magnifications of the marked regions shown in **H**–**M**. **N**–**Q** Retinal morphology of control and treated retinas at PN30 and PN60. **R** Quantification of cone survival in control and TSA-treated retinas. *Y* axis is in log2 scale. Data are shown as means ± SEM (n = 5–10 animals per age). Numerical p values by two-way ANOVA. The fitting of the exponential curves is shown in dotted lines. Scale bars: **A**, **H**–**M** 50 µm; **B**–**G** 500 µm; **H'**–**M'** 20 µm; **N**–**Q** 10 µm. ONL outer nuclear layer, INL inner nuclear layer, GCL ganglion cell layer, PN postnatal days.

death of both mutation-affected rods and secondary dying cones may be associated with HDAC overactivation.

HDAC inhibition prolongs cone survival in RP mice

To determine if HDAC inhibition has the potential to prevent secondary cone degeneration, we injected a well-established class I and II HDAC inhibitor, TSA, in the *rd1*$^{TN\text{-}XL}$ mouse that expresses the fluorescent TN-XL biosensor exclusively in M- and L-cones [19] (Figs. S1, S2). To minimize the indirect positive effects of increased rod survival afforded by HDAC inhibition on the *rd1* cone survival, we selected a late time-point to start the treatment, PN19. Already from PN19, the *rd1*$^{TN\text{-}XL}$ ONL is reduced to only one row of photoreceptors, almost exclusively cones (Fig. 2A). After a single intravitreal injection of TSA at PN19, we assessed cone survival up to 3 months of age at different time points: PN26, PN30, PN37, PN45, PN60, and PN90. Whole-mount preparations of sham-injected eyes showed center to periphery gradient of cone loss at PN30 (Fig. 2B). In contrast, an increased cone-specific fluorescent signal was detected in

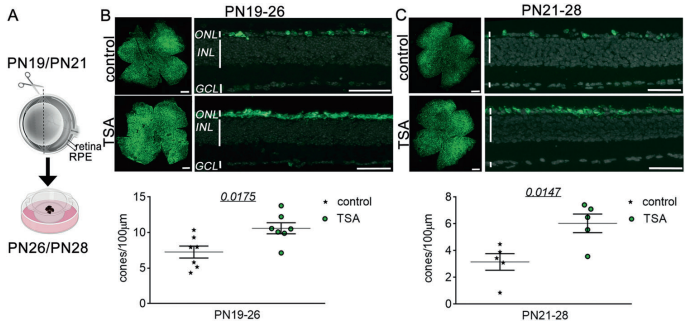

Fig. 3 HDAC inhibition protects *rd1*$^{TN\text{-}XL}$ cones ex vivo. A Schematic representation of the ex vivo retinal explants preparation. Retinas from *rd1*$^{TN\text{-}XL}$ mice were collected at PN19 or PN21 and treated for 7 days with control or TSA-medium. **B–C** Representative flat mount preparations and cross-sections of explanted retinas, that were used for the quantification of cone survival, shown in the dot plot below. Data are shown as mean ± SEM ($n = 5$–7 animals per age group). Numerical p values by unpaired, two-tailed t-test. Scale bars in whole mounts 500 µm; retinal cross-sections 50 µm. RPE retinal pigment epithelium, ONL outer nuclear layer, INL inner nuclear layer, GCL ganglion cell layer, PN postnatal day.

treated contralateral eyes (Fig. 2C). While at PN60 and PN90, loss of cones had proceeded in control eyes, with cones remaining only at the far periphery (Fig. 2D, F), the treated eyes showed higher immunofluorescent signals, suggesting enhanced cone preservation in the central retina up to 3 months of age (Fig. 2E, G). An increase in cone survival was even more evident on retinal cross-sections, where individual cone cell bodies and remaining cone segments could be clearly identified (Figs. 2H–M', S1, S2). A higher number of cones in TSA-treated animals was also evident in retinal light micrographs (Fig. 2N–Q). While untreated retinas showed a reduced density of nuclei, many of which were pyknotic, the treated retina displayed healthier cone morphology with classical heterochromatin distribution (Fig. 2O, Q) [22]. A single intravitreal injection was sufficient to prevent loss of *rd1*$^{TN\text{-}XL}$ cones for up to 7 days, while in control retinas, cone degeneration continued with ~15% fewer cones than at the beginning of the treatment. A plot of cone numbers up to PN90 showed that cone loss in control and treated retinas followed an exponential decay function, with the two curves clearly separated (Fig. 2R). In addition, fitted trend lines showed significantly broader separation of the two curves at PN90 (Figs. 2R and S3) and predicted an X-axis intersection of the treated curve with a delay of 16 days, compared to control (PN79 for treated *vs*. PN95 for control retinas, Fig. 2R). These extrapolations suggest that the TSA treatment not only delayed but also slowed down secondary cone degeneration.

To analyze the effects of continuous TSA treatment on cone survival, we treated *rd1*$^{TN\text{-}XL}$ retinal explants from PN19 until PN26 ex vivo. Retinal cultures, consisting of the retina and RPE layer, enable maintaining mature neurons in situ, and complex neuronal connections while providing the possibility for constant exposure to a drug via a culture medium (Fig. 3A). Similarly to *rd1*$^{TN\text{-}XL}$ cone degeneration in vivo, the center to periphery gradient of cone loss was more prominent in the control explant cultures (Fig. 3B). Quantification of cone numbers in retinal cross-sections showed ~30% increase in the cone survival in TSA-treated retinal explants (Fig. 3B).

Next, we asked if the HDAC inhibition has the potential to protect secondary dying cones even at a later stage of degeneration. For this, we started the treatment at PN21 and assessed the *rd1*$^{TN\text{-}XL}$ cone survival after one week in culture (Fig. 3C). Also in this case, the TSA treatment significantly improved cone survival, with 52% more cones in the treated explants. We also tested the neuroprotective properties of Panobinostat, a clinically approved pan-HDAC inhibitor within the same group of inhibitors as TSA [36]. As with TSA, 7 days treatment with Panobinostat increased *rd1*$^{TN\text{-}XL}$ cone survival up to 30% (Fig. S4).

HDAC inhibition improves cone-mediated light-responses

We then wanted to see whether the remaining cones were light-sensitive and able to drive functional responses. We used a micro-electrode array (MEA) [37] to record the light-mediated spiking activity of retinal ganglion cells (RGCs) of *rd1*$^{TN\text{-}XL}$ retinal explants. The experimental setup included a light source at the bottom of the MEA chamber, mimicking the physiological situation where light stimulation comes from the ganglion cell side, while the RPE layer

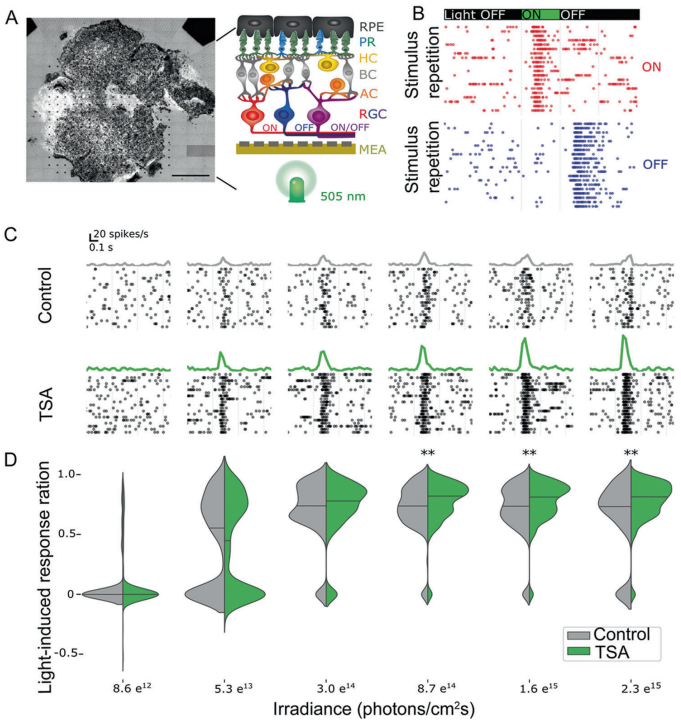

Fig. 4 HDAC inhibition improves cone function in *rd1*$^{TN\text{-}XL}$ retinal explants. **A** A micro-electrode array (MEA) with 256 electrodes was used to record retinal ganglion cell (RGC) responses in control and TSA-treated PN19-26 *rd1*$^{TN\text{-}XL}$ retinal explants. Schematic drawing of the MEA setup used in the study. **B** Representative recordings of ON and OFF responses from TSA-treated retinal explants during stimulation with flickering light (350 ms flashes, 505 nm) shown as raster plots. Each dot indicates one spike. The green bar indicates the start of light stimulation. **C** Exemplary spike responses obtained in ontrol (gray) and treated (green) explants at six different light intensities, shown as raster plots (bottom) and averaged firing rate histograms (top). **D** Quantification and discrimination of the response ratio in control (gray) and treated explants (green). Significant differences based on Wilcoxon rank-sum test are detected for three high light intensities ($n = 161$ channels from eight control, $n = 274$ from nine treated retinas, $^{**}p < 0.01$). RPE retinal pigment epithelium, PR photoreceptors, HC horizontal cells, BC bipolar cells, AC amacrine cells, RGC retinal ganglion cells.

on the top of explants provided a physiological environment for light absorption (Fig. 4A).

A LED emitting green light (505 nm) with increasing light intensities, far below the safety limit for the human eye [38], was used to stimulate cones in control and TSA-treated PN19-26 retinal explants. Light-ON and Light-OFF responses were detected in both control and treated retinas suggesting preservation of physiological network functionality (Fig. 4B). To estimate the degree of activity change upon light stimulation, we calculated a light-induced response ratio for ON responsive MEA electrodes. The light-induced response ratio quantifies how much the firing rate (Fig. 4C) increases during light stimulation and can be considered a simple link between the number of rescued cones and functional readout. The distribution of the light-induced response ratio, presented as a violin plot, demonstrates that increasing light intensities lead to a higher firing rate (Fig. 4D). Changes of the spontaneous activity under the same light intensities were not detected. For each condition (control *vs*. treatment), the light-induced response ratio of the two distributions were compared. While for low intensities, the median values in control and treated retinas were not significantly different, the light-induced response ratio increased in the treated samples and was significantly different above a light intensity of 8.7 e^{14} photons/cm^2 sec ($p < 0.01$). The median light-induced response ratio in

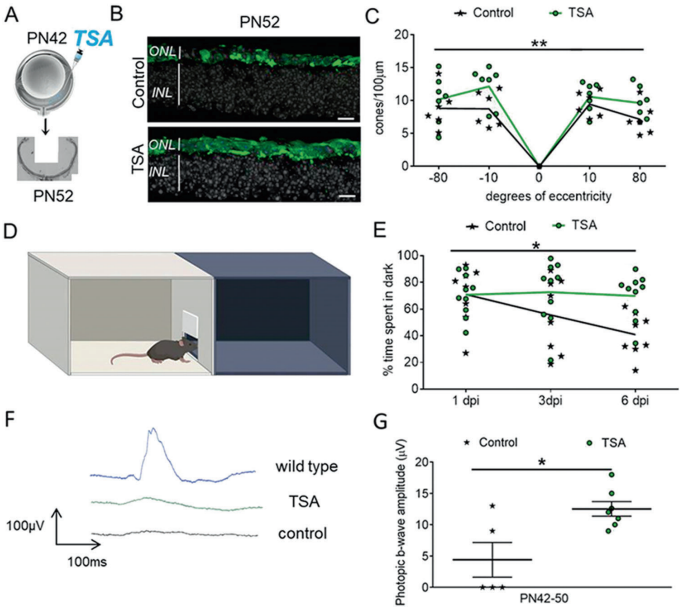

Fig. 5 HDAC inhibition promotes cone survival and visual function in *rd10* mice. A A schematic representation of a single intravitreal TSA injection at PN42 followed by quantification of cones 10 days post-injection. **B** Representative images of retinal cross-sections from control and TSA-treated retinas at PN52 used to count the number of cones (cone arrestin-labeled cones in green, DAPI-labeled nuclei in gray). **C** Spider diagram showing the number of cones along the dorso-ventral axis, corresponding to 10°, 80°, −10°, and −80° of eccentricity from the optic nerve, respectively. **D** Drawing of the open filed behavioral test used to assess cone-mediated vision. **E** Percentage of time spent in the dark compartment for control and TSA-treated animals 1, 3, and 6 days post-injection (dpi). **F** Representative traces of photopic ERG recordings used to evaluate cone function in wild-type, TSA- and sham-treated *rd10* retinas at PN50. **G** Photopic b-wave amplitudes of control and TSA-treated *rd10* mice. Data are shown as means ± SEM ($n = 5$–10 animals per group). Statistical significance was assessed using two-way ANOVA (**C** and **E**) and Mann–Whitney nonparametric test (**G**), with $*p < 0.05$, $**p < 0.01$. Scale bars: 10 µm. ONL outer nuclear layer, INL inner nuclear layer, PN postnatal day.

treated retinas reached 0.82 while in control condition it approached 0.74 (Fig. 4D).

To determine if HDAC inhibition has the potential to delay secondary cone death and preserve visual function independent of the underlying mutation, we injected *rd10* mice at a stage when the majority of rods have degenerated [1, 3]. A single intravitreal injection at PN42 resulted in a higher number of cones in TSA-treated compared to sham-treated retinas (Fig. 5A–C). Increased cone survival was accompanied by amelioration of vision-mediated behavior of *rd10* animals injected bilaterally with TSA (Fig. 5D, E). An improvement in cone function was also detected by electroretinography (ERG). At PN50, a modest but significant increase in photopic b-wave amplitudes was detected in TSA-treated retinas (Fig. 5F, G). Collectively our data suggest that HDAC inhibition has the potential to support cone survival and function at late stages of photoreceptor degeneration in different RP mouse models.

HDAC inhibition induces global changes in gene-transcription patterns in the surviving cones

We performed whole transcriptome analysis of flow-sorted *rd1*$^{TN\text{-}XL}$ cones from retinal explants after seven days in culture (PN19-26). TN-XL-positive cells represented 95% of FASC-sorted cells, suggesting a highly purified cone population (SI Appendix, Fig. S5). RNA-seq analysis of differentially expressed genes (DEG) in TSA-treated *vs.* untreated cones revealed 1845 genes with significantly different expression (enrichment of 1163 and reduction in 682 genes), as indicated in the volcano plot (Fig. 6A, Supplementary gene expression dataset). To identify signature trends for activation or inhibition of downstream

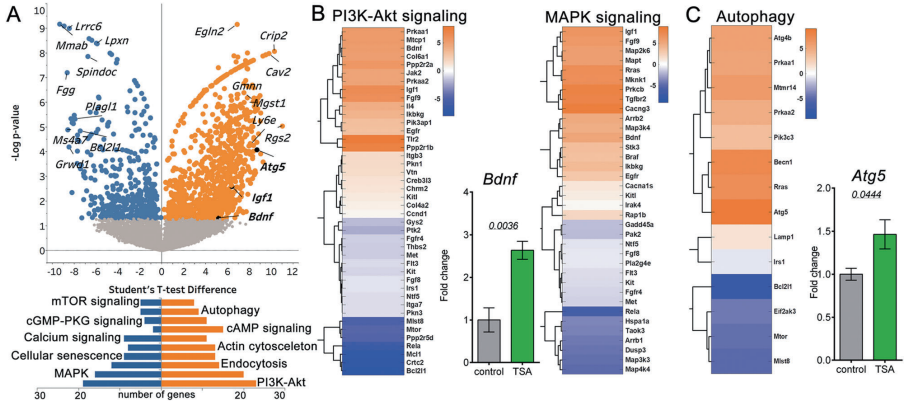

Fig. 6 Whole genome transcriptomic analysis of TSA-induced survival of *rd1*$^{TN\text{-}XL}$ cones. A A volcano plot representation of differentially expressed genes as detected by RNA-seq in flow-sorted cones from treated *vs*. untreated PN19-26 *rd1*$^{TN\text{-}XL}$ ($n = 3$ animals). Orange and blue dots: significantly enriched and perturbed genes, respectively, in TSA-treated cones (FDR-based, Student's *t* test of mean difference). PaintOmics analysis was used to identify differentially regulated pathways in TSA-protected cones. **B**, **C** Heat maps with hierarchical clustering of differentially expressed genes within PI3k-Akt, MAPK, and autophagy pathways. Genes showing Student's *t* test difference between TSA and control, with $p \le 0.05$ were selected. Bar graphs: qRT-PCR validation of differential expression of *Bdnf* (**B**) and *Atg5* (**C**) in FACS-sorted cones. Fold changes are relative to controls. Data are shown as mean ± SEM ($n = 4$ animals). Numerical *p* values by Mann–Whitney nonparametric test.

pathways, we used protein-coding genes with significant differential expression following the TSA treatment ($p \le 0.05$), regardless of their fold change. Top molecular pathways differentially regulated following the TSA treatment included transcriptional changes of around 40 genes belonging to PI3K-Akt and/or MAPK signaling pathways and more than 20 genes regulating cellular senescence, endocytosis, actin cytoskeleton, as well as cAMP and calcium signaling (Fig. 6A, http://www.paintomics.org/?jobID=4CIbSr1eA4).

The heatmap representation of the genes showing differential expression within the PI3K-Akt cascade (mmu04151) demonstrated the enrichment of about half of the genes in the TSA-treated cones (23/42 genes) (Fig. 6B). Similarly, 20 out of 36 genes were enriched within the MAPK cascade (mmu04010). Among highly abundant transcripts were the brain-derived neurotrophic factor (*Bdnf*), and the insulin-like growth factor 1 (*Igf1*), growth factors regulating MAPK and PI3K-Akt pathways. A significantly increased *Bdnf* expression in the TSA-treated cones sorted from independent samples was confirmed by quantitative PCR (qRT-PCR), while a tendency towards increased expression was observed for *Igf1* (Figs. 6B, S6). To determine if the survival of the TSA-treated cones was mediated *via* PI3K-Akt and/or MAPK pathways, we assessed cone survival in the *rd1*$^{TN\text{-}XL}$ explants following the combined treatment with TSA and well-established inhibitors of PI3K-Akt and MAPK pathways, LY294002 and U0126, respectively. U0126 blocks MAPK signaling by inhibiting MEK1/2 [39], while LY294002 inhibits both the PI3K-Akt pathway and autophagosome formation [40, 41]. To avoid potential cytotoxic effects of prolonged treatment with PI3K-Akt and MAPK inhibitors, we assessed cone survival in *rd1*$^{TN\text{-}XL}$ explants after one week in culture, but with inhibitors present only during the first 2 days. Interestingly, the TSA treatment of only 2 days afforded the same extent of cone protection as the 7 days treatment. Whereas LY204002 or U0126 had no effect on cone survival in control retinas, both inhibitors significantly decreased TSA-induced cone survival (Fig. 7A, B).

Pathway analysis also showed significant upregulation of 9/14 genes related to autophagy (mmu04140), an additional pro-survival mechanism (Fig. 6C) [42, 43]. Significant upregulation of the autophagy-related-5 gene (*Atg5*) in surviving cones was confirmed by qRT-PCR (Figs. 6C, S6). We also assessed the formation of autophagolysosomes in surviving cones by quantifying the colocalized puncta between an autophagosome marker, the microtubule-associated proteins 1A/1B light chain 3B (LC3B), and lysosome-associated membrane protein 1 (LAMP1) in control and treated *rd1*$^{TN\text{-}XL}$ cones. LC3-LAMP1 staining of retinal cross-sections from PN19-26 in vivo TSA-treated mice showed an overall increase in both LC3- and LAMP1-positive vesicles, as well in colocalizing puncta within the

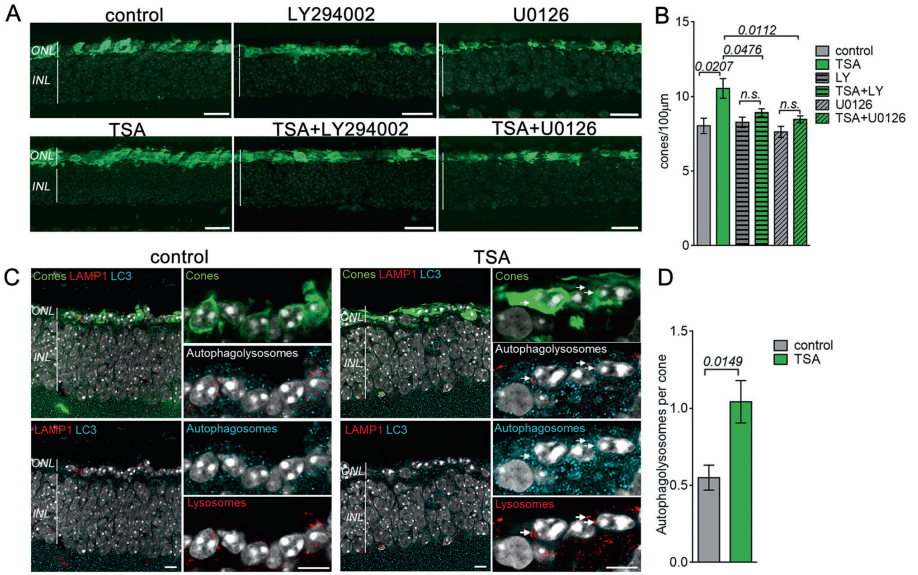

Fig. 7 TSA-induced cone survival is modulated by PI3K-Akt, MAPK, and autophagy. A Retinal cross-sections of control (top) or TSA-treated (bottom) *rd1*$^{TN\text{-}XL}$ retinas at PN26 incubated from PN19-PN21 with LY294002 or U0126. TN-XL cones appear green. **B** Quantification of cones in the ex vivo retinas at PN26. **C** Representative images from a single confocal plane on one retinal cross-section from an *rd1*$^{TN\text{-}XL}$ mouse at PN26, sham- or TSA-injected at PN19, with TN-XL cones (green), autophagosomes (cyan, LC3B antibody), and lysosomes (red, LAMP1 antibody). The colocalization of autophagosomes and lysosomes is marked with arrows. **D** Quantification of the number of colocalized LC3-LAMP1 (autophagolysosomes) puncta per cone in the ONL. Data are shown as mean ± SEM based on 6–10 positions within retina, $n = 6$–8 animals in **B**; $n = 3$ animals in **D**. Numerical p values by Mann–Whitney nonparametric test. Scale bars in **A** 20 µm, in **C** 10 µm. ONL outer nuclear layer, INL inner nuclear layer.

cones in comparison to sham-treated retinas (Fig. 7C, D). Similarly, increased LC3-LAMP1 colocalization in cones was also detected in ex vivo treated *rd1*$^{TN\text{-}XL}$ explants (Fig. S7).

Finally, to identify similar molecular signatures to the expression pattern obtained in this study, we submitted our data to the Library of Integrated Network-Based Cellular Signatures project (LINCS) (Fig. S8) [44]. The analysis matched our data to gene expression profiles of TSA and vorinostat treatments on human cell lines deposited in the LINCS platform. Of note, vorinostat is a clinically approved pan-HDAC inhibitor from the same class as TSA. This suggests a possibility for repurposing "off the shelf" HDAC-inhibiting drugs for the treatment of RP.

Discussion

Cone photoreceptors are indispensable for human vision in daylight, and their loss has devastating effects on daily tasks and life quality [45]. Here, we show that cones have an innate ability for survival even in the total absence of rods, which can be induced by HDAC-driven transcriptional changes. At the same time, HDAC inhibition may affect other cells in the retina, which could support cone survival in the absence of rods [46, 47]. A single intravitreal injection of HDAC inhibitor fully protected cones for one week and significantly slowed down cone loss up to 90 days even when all rods had already degenerated. Interestingly, the *rd1*$^{TN\text{-}XL}$ cone loss followed exponential kinetics, as suggested for other forms of neurodegeneration [48]. The observed exponential cone loss in the *rd1*$^{TN\text{-}XL}$ retina excludes the possibility of the cumulative damage caused by the loss of rods and suggests that secondary dying cones can be rescued at any time, although with the disease progression, fewer cells will be amenable for rescue. Therefore, a treatment even at late stages of the disease is likely to be beneficial [48]. Indeed, our data on HDAC-induced cone protection at different stages of *rd1*$^{TN\text{-}XL}$ cone loss (PN19 and PN21) confirm this and is furthermore in line with other

observations indicating that the window-of-opportunity for the treatment of retinal dystrophies is much broader than it is currently considered [2, 49].

Preserving retinal function in the absence of rods is the ultimate goal of neuroprotective therapies for late-stage RP. Recent studies suggest that therapies specifically targeting cones at stages where most of the rods are still present could preserve visual function in RP mouse models [3, 10]. Here we have demonstrated an intact cone-driven retinal circuitry in the TSA-treated *rd1*$^{TN\text{-}XL}$ retinal explants, even in the absence of rods, by recording cone-mediated light-induced responses from large populations of individual RGCs. Unfortunately, the low cone number and the impaired morphology of the remaining cones, at the stages where rods have already fully degenerated, is a major obstacle in assessing visual improvements by standard functional tests like ERG [50]. While we did not detect changes in ERG-wave amplitudes in *rd1*$^{TN\text{-}XL}$ mice treated at such late stages of degeneration, a modest improvement of ERG recordings was detected in *rd10* mice following the treatment. Notably, despite ERG amplitudes remaining lower than in wild-type mice, the significant improvement in visually-driven behavior suggests that the potential benefits for the daily tasks of RP patients may be achievable even at the late stages of the disease [51]. It is very challenging to assess the effectiveness of vision therapy, even in patients. For example, no improvements in ERG recordings were reported in patients following RPE65 gene augmentation therapy, although the useful vision was significantly increased in some patients [52]. Even in the patient who showed a dramatic improvement in the obstacle-path mobility test, *i.e.*, functional vision, the ERG did not differ significantly from baseline. Therefore, it is expected that even a minor but significant improvement in visual function by the ERG should be positively correlated with treatment outcome.

For the treatment of retinal diseases, intravitreal injections are the preferred route of administration, as larger volumes of a drug can be applied, and the risk of retinal damage is reduced. However, due to an extensive retinal circulation and the brain-retinal-barrier's permeability for low molecular weight compounds, intravitreally injected TSA is cleared from the mouse eye in less than 2 h [14]. Still, a single injection led to a long-lasting cone survival, suggesting the possibility of epigenetically induced pro-survival mechanisms that could counteract environmental insults caused by the absence of rods. While HDAC inhibition induces changes in gene expression within minutes [17], the effects of transcriptional regulation can persist for months [53].

In advanced RP, cones are exposed to high oxidative stress and inflammation [3, 4, 54] that elicit a broad range of responses, from proliferation to cell death [55]. Our RNA-seq data suggested changes in major pathways involved in regulating the cellular response to oxidative stress, the mitogen-activated protein kinases (MAPK), and phosphoinositide 3-kinase activated protein kinase (PI3K-Akt) pathways. While previous studies linked the neuroprotective effect of docosahexaenoic acid [56] and leukemia inhibitory factor to MAPK pathway activation in rod photoreceptors [57], our study highlights the role of MAPK signaling in the prevention of secondary cone degeneration. TSA-induced cone survival was significantly reduced by U0126, linking cone survival in secondary cone degeneration to the ERK pathway [39]. A similar reduction in cone survival was also observed when PI3K signaling was inhibited by LY294002, highlighting the importance of the PI3K-Akt pathway also in cone photoreceptor survival [58]. While more specific studies are necessary to precisely address the protective role of MAPK and PI3K-Akt activation in secondary dying cones, these results not only validate our RNA-seq data but also suggest that HDAC inhibition may lead to the expression of neurotrophic factors that mediate neuroprotection *via* activation of these pathways [59, 60]. Indeed, our data suggest that an increase in transcription of neurotrophic factors, such as *Bdnf*, may contribute to cone survival. Although BDNF-induced neuroprotective effects on light- or mutation-induced photoreceptor degeneration was recognized as early as 1992 by LaVail et al. [61], our study indicates a direct upregulation of *Bdnf* transcription in the cones protected from secondary degeneration.

Cone starvation has also been recognized as one of the main contributors to secondary cone death in RP [1, 10, 62]. Autophagy is the primary cellular mechanism for self-nourishment and recycling of metabolites to supplement macromolecules and energy under severe starvation [42]. The beneficial role of autophagy is demonstrated for the clearance of misfolded proteins in mutation-affected photoreceptors or dysfunctional RPE in age-related macular degeneration (AMD) [43, 63]. Nevertheless, in secondary cone degeneration, it remained unclear whether increased autophagy is beneficial or not [1, 64]. The observed upregulation of *Atg5* transcription and an increased number of autophagolysosomes in TSA-treated cones are in line with the previously reported effects of HDAC inhibition on autophagy induction [65] and highlight autophagy as a protective mechanism in secondary cone degeneration.

In our study, a single intravitreal TSA injection afforded a prolonged delay in cone cell death. Nevertheless, degeneration proceeded, albeit with slowed kinetics. This could stem from rapid TSA degradation and/or possible off-target effects. TSA is one of the most well-studied hydroxamate HDAC inhibitors, reversibly inhibiting class I and II HDACs [66]. Low nanomolar doses of TSA efficiently inhibit HDAC in tumor and non-tumor cells [67], but as TSA undergoes rapid metabolic degradation [68], systemic

treatments require repeated administration [67]. Translating our approach into a clinical application may benefit from the development of drug delivery systems that enable a sustained, long-term release of an HDAC inhibitor [69]. Alternatively, as a single intravitreal injection could prevent cone degeneration for one week in mice with extremely fast photoreceptor loss, monthly injections could have similar effects in patients where the loss of cones spans over decades [70]. Future studies may also address the development of more specific and effective HDAC inhibitors that may act longer on ocular tissue. Specifically, other drugs belonging to the group of hydroxamic acids, such as vorinostat, belinostat, and panobinostat, might be of interest as we show that clinically approved panobinostat protected cone photoreceptor ex vivo to a similar extent as TSA. LINCS analysis indicated that also vorinostat may be repurposed for RP treatment. Notably, the clinical data already available [71] would greatly facilitate the repurposing for RP treatment, while the side-effect profile associated with systemic application in cancer therapy would likely be of lesser concern if these drugs were used only locally in the eye.

Our previous studies showed HDAC overactivation at the peak of photoreceptor loss in ten rodent models for retinal dystrophies [15, 35]. Aberrant HDAC activity was detected in photoreceptors regardless of whether underlying mutations affect the phototransduction cascade (*rd1*, *rd10*, *Rho* KO, S334ter, P23H, *Cngb1* KO, *Cnga3* KO, *cpfl1*), the photoreceptor outer segment structure (*rd2*) or the visual cycle (*Rpe65* KO). This suggests that increased HDAC activity may contribute to the mutation-related photoreceptor cell death caused by cGMP accumulation [69], endoplasmic reticulum stress [72, 73], or microglia activation [74]. Importantly, HDAC inhibition is also extensively discussed as a therapeutic option for other diseases such as cancer [75], Alzheimer's disease [76], or Duchenne muscular dystrophy [77]. Consequently, in the view of the use of HDAC inhibition for the treatment of various diseases, and our previous data linking HDAC overactivation to rod loss in different mouse models of RP, this study highlights HDACs as a common denominator of both mutation-induced rod cell death and secondary cone degeneration and provides a unique therapeutic option for the treatment of RP regardless of the stage of degeneration.

Finally, detrimental environmental conditions inducing cone loss at the late stages of RP share essential similarities with AMD, the leading cause of blindness in the industrialized world [78]. Although RPE cells are considered the primary target for AMD pathology, loss of cone photoreceptors in the macular region in AMD patients characterizes the final stages of the disease [79]. Since RPE dysfunction in AMD may expose cones to a milieu similar to the one in late-stage RP, HDAC inhibition holds significant promise also for the treatment of more common forms of retinal degeneration.

Data availability

All analyzed datasets are included in the manuscript and SI Appendix.

Acknowledgements We are thankful to Klaudija Masarini, Norman Rieger, Patricia Velasco, Coni Imsand for technical assistance and Nicolas Casadei for the help in RNA-seq. We are grateful to Botond Roska for inspiring scientific discussions. We thank Irena Stingl for graphical design. This work was supported by the ProRetina foundation, the Kerstan Foundation, Deutsche Forschungsgemeinschaft (DFG TR 1238/4-1), Swiss National Science Foundation (31003A_173008), BMBF (FKZ: 01EK1613E), and GC2018-098557-B-I00 from MCIU/AEI/FEDER, UE. RGS is a recipient of a JIN grant RTI2018-098990-J-I00 from MCIU, Spain. We acknowledge support by Open Access Publishing Fund of the University of Tübingen.

Funding Open Access funding enabled and organized by Projekt DEAL.

Compliance with ethical standards

Conflict of interest The authors declare that they have no conflict of interest.

References

1. Punzo C, Kornacker K, Cepko CL. Stimulation of the insulin/mTOR pathway delays cone death in a mouse model of retinitis pigmentosa. Nat Neurosci. 2009;12:44–52.
2. Koch SF, Tsang SH. Success of gene therapy in late-stage treatment. Adv Exp Med Biol. 2018;1074:101–7.
3. Wang SK, Xue Y, Rana P, Hong CM, Cepko CL. Soluble CX3CL1 gene therapy improves cone survival and function in mouse models of retinitis pigmentosa. Proc Natl Acad Sci USA. 2019;116:10140–9.
4. Komeima K, Rogers BS, Lu L, Campochiaro PA. Antioxidants reduce cone cell death in a model of retinitis pigmentosa. Proc Natl Acad Sci USA. 2006;103:11300–5.
5. Byrne LC, Dalkara D, Luna G, Fisher SK, Clerin E, Sahel JA, et al. Viral-mediated RdCVF and RdCVFL expression protects

cone and rod photoreceptors in retinal degeneration. J Clin Invest. 2015;125:105–16.
6. Viringipurampeer IA, Metcalfe AL, Bashar AE, Sivak O, Yanai A, Mohammadi Z, et al. NLRP3 inflammasome activation drives bystander cone photoreceptor cell death in a P23H rhodopsin model of retinal degeneration. Hum Mol Genet. 2016;25:1501–16.
7. Jeon CJ, Strettoi E, Masland RH. The major cell populations of the mouse retina. J Neurosci. 1998;18:8936–46.
8. Cepko CL, Vandenberghe LH. Retinal gene therapy coming of age. Hum Gene Ther. 2013;24:242–4.
9. Leveillard T, Mohand-Said S, Lorentz O, Hicks D, Fintz AC, Clerin E, et al. Identification and characterization of rod-derived cone viability factor. Nat Genet. 2004;36:755–9.
10. Venkatesh A, Ma S, Le YZ, Hall MN, Ruegg MA, Punzo C. Activated mTORC1 promotes long-term cone survival in retinitis pigmentosa mice. J Clin Invest. 2015;125:1446–58.
11. Yang XJ, Seto E. HATs and HDACs: from structure, function and regulation to novel strategies for therapy and prevention. Oncogene. 2007;26:5310–8.
12. Haberland M, Montgomery RL, Olson EN. The many roles of histone deacetylases in development and physiology: implications for disease and therapy. Nat Rev Genet. 2009;10:32–42.
13. Marks P, Rifkind RA, Richon VM, Breslow R, Miller T, Kelly WK. Histone deacetylases and cancer: causes and therapies. Nat Rev Cancer. 2001;1:194–202.
14. Trifunovic D, Arango-Gonzalez B, Comitato A, Barth M, Del Amo EM, Kulkarni M, et al. HDAC inhibition in the cpfl1 mouse protects degenerating cone photoreceptors in vivo. Hum Mol Genet. 2016;25:4462–72.
15. Trifunovic D, Petridou E, Comitato A, Marigo V, Ueffing M, Paquet-Durand F. Primary rod and cone degeneration is prevented by HDAC inhibition. Adv Exp Med Biol. 2018;1074:367–73.
16. Sancho-Pelluz J, Alavi M, Sahaboglu A, Kustermann S, Farinelli P, Azadi S, et al. Excessive HDAC activation is critical for neurodegeneration in the rd1 mouse. Cell Death Dis. 2010;1:1–9.
17. Chen B, Cepko CL. HDAC4 regulates neuronal survival in normal and diseased retinas. Science. 2009;323:256–9.
18. Kumar A, Midha N, Gogia V, Gupta S, Sehra S, Chohan A. Efficacy of oral valproic acid in patients with retinitis pigmentosa. J Ocul Pharm Ther. 2014;30:580–6.
19. Wei T, Schubert T, Paquet-Durand F, Tanimoto N, Chang L, Koeppen K, et al. Light-driven calcium signals in mouse cone photoreceptors. J Neurosci. 2012;32:6981–94.
20. Kulkarni M, Trifunovic D, Schubert T, Euler T, Paquet-Durand F. Calcium dynamics change in degenerating cone photoreceptors. Hum Mol Genet. 2016;25:3729–40.
21. Kaplan HJ, Chiang CW, Chen J, Song SK. Vitreous volume of the mouse measured by quantitative high-resolution MRI. ARVO Ann Meet Abstr. 2010;51.
22. Samardzija M, Todorova V, Gougoulakis L, Barben M, Notzli S, Klee K, et al. Light stress affects cones and horizontal cells via rhodopsin-mediated mechanisms. Exp Eye Res. 2019;186:107719.
23. Farrow K, Masland RH. Physiological clustering of visual channels in the mouse retina. J Neurophysiol. 2011;105:1516–30.
24. Carcieri SM, Jacobs AL, Nirenberg S. Classification of retinal ganglion cells: a statistical approach. J Neurophysiol. 2003;90:1704–13.
25. Bourin M, Hascoet M. The mouse light/dark box test. Eur J Pharm. 2003;463:55–65.
26. Takao K, Miyakawa T. Light/dark transition test for mice. J Vis Exp. 2006:104.
27. Palfi A, Ader M, Kiang AS, Millington-Ward S, Clark G, O'Reilly M, et al. RNAi-based suppression and replacement of rds-peripherin in retinal organotypic culture. HumMutat. 2006;27:260–8.
28. Ge SX, Son EW, Yao R. iDEP: an integrated web application for differential expression and pathway analysis of RNA-Seq data. BMC Bioinforma. 2018;19:534.
29. Torre D, Lachmann A, Ma'ayan A. BioJupies: automated generation of interactive notebooks for RNA-seq data analysis in the cloud. Cell Syst. 2018;7:556–61 e3.
30. Hernandez-de-Diego R, Tarazona S, Martinez-Mira C, Balzano-Nogueira L, Furio-Tari P, Pappas GJ Jr, et al. PaintOmics 3: a web resource for the pathway analysis and visualization of multi-omics data. Nucleic Acids Res. 2018;46:W503–W9.
31. Garcia-Alcalde F, Garcia-Lopez F, Dopazo J, Conesa A. Paintomics: a web based tool for the joint visualization of transcriptomics and metabolomics data. Bioinformatics 2011;27:137–9.
32. Ho J, Tumkaya T, Aryal S, Choi H, Claridge-Chang A. Moving beyond P values: data analysis with estimation graphics. Nat Methods. 2019;16:565–6.
33. Tyanova S, Temu T, Sinitcyn P, Carlson A, Hein MY, Geiger T, et al. The Perseus computational platform for comprehensive analysis of (prote)omics data. Nat Methods. 2016;13:731–40.
34. Carter-Dawson LD, LaVail MM, Sidman RL. Differential effect of the rd mutation on rods and cones in the mouse retina. Invest Ophthalmol Vis Sci. 1978;17:489–98.
35. Arango-Gonzalez B, Trifunovic D, Sahaboglu A, Kranz K, Michalakis S, Farinelli P, et al. Identification of a common non-apoptotic cell death mechanism in hereditary retinal degeneration. PLoS One. 2014;9:e112142.
36. Laubach JP, Moreau P, San-Miguel JF, Richardson PG. Panobinostat for the treatment of multiple myeloma. Clin Cancer Res. 2015;21:4767–73.
37. Stutzki H, Leibig C, Andreadaki A, Fischer D, Zeck G. Inflammatory stimulation preserves physiological properties of retinal ganglion cells after optic nerve injury. Front Cell Neurosci. 2014;8:38.
38. International Commission on Non-Ionizing Radiation P. ICNIRP guidelines on limits of exposure to laser radiation of wavelengths between 180 nm and 1,000 mum. Health Phys. 2013;105:271–95.
39. Favata MF, Horiuchi KY, Manos EJ, Daulerio AJ, Stradley DA, Feeser WS, et al. Identification of a novel inhibitor of mitogen-activated protein kinase kinase. J Biol Chem. 1998;273:18623–32.
40. Vlahos CJ, Matter WF, Hui KY, Brown RF. A specific inhibitor of phosphatidylinositol 3-kinase, 2-(4-morpholinyl)-8-phenyl-4H-1-benzopyran-4-one (LY294002). J Biol Chem. 1994;269:5241–8.
41. Blommaart EF, Krause U, Schellens JP, Vreeling-Sindelarova H, Meijer AJ. The phosphatidylinositol 3-kinase inhibitors wortmannin and LY294002 inhibit autophagy in isolated rat hepatocytes. Eur J Biochem. 1997;243:240–6.
42. Levine B, Kroemer G. Biological functions of autophagy genes: a disease perspective. Cell. 2019;176:11–42.
43. Boya P, Esteban-Martinez L, Serrano-Puebla A, Gomez-Sintes R, Villarejo-Zori B. Autophagy in the eye: development, degeneration, and aging. Prog Retin Eye Res. 2016;55:206–45.
44. Duan Q, Reid SP, Clark NR, Wang Z, Fernandez NF, Rouillard AD, et al. L1000CDS(2): LINCS L1000 characteristic direction signatures search engine. NPJ Syst Biol Appl. 2016;2.
45. Bramall AN, Wright AF, Jacobson SG, McInnes RR. The genomic, biochemical, and cellular responses of the retina in inherited photoreceptor degenerations and prospects for the treatment of these disorders. Annu Rev Neurosci. 2010;33:441–72.
46. Jorstad NL, Wilken MS, Grimes WN, Wohl SG, VandenBosch LS, Yoshimatsu T, et al. Stimulation of functional neuronal regeneration from Muller glia in adult mice. Nature 2017;548:103–7.
47. Tokarz P, Kaarniranta K, Blasiak J. Inhibition of DNA methyltransferase or histone deacetylase protects retinal pigment epithelial cells from DNA damage induced by oxidative stress by the

stimulation of antioxidant enzymes. Eur J Pharm. 2016; 776:167–75.
48. Clarke G, Collins RA, Leavitt BR, Andrews DF, Hayden MR, Lumsden CJ, et al. A one-hit model of cell death in inherited neuronal degenerations. Nature 2000;406:195–9.
49. Samardzija M, Masarini K, Ueffing M, Trifunovic D. HDAC inhibition prevents primary cone degeneration even after the onset of degeneration. Adv Exp Med Biol. 2019;1185:383–7.
50. Han J, Dinculescu A, Dai X, Du W, Smith WC, Pang J. Review: the history and role of naturally occurring mouse models with Pde6b mutations. Mol Vis. 2013;19:2579–89.
51. Storchi R, Rodgers J, Gracey M, Martial FP, Wynne J, Ryan S, et al. Measuring vision using innate behaviours in mice with intact and impaired retina function. Sci Rep. 2019;9:10396.
52. Bainbridge JW, Mehat MS, Sundaram V, Robbie SJ, Barker SE, Ripamonti C, et al. Long-term effect of gene therapy on Leber's congenital amaurosis. N. Engl J Med. 2015;372:1887–97.
53. Stolzenberg DS, Stevens JS, Rissman EF. Histone deacetylase inhibition induces long-lasting changes in maternal behavior and gene expression in female mice. Endocrinology 2014;155:3674–83.
54. Zhao L, Zabel MK, Wang X, Ma W, Shah P, Fariss RN, et al. Microglial phagocytosis of living photoreceptors contributes to inherited retinal degeneration. EMBO Mol Med. 2015;7:1179–97.
55. Martindale JL, Holbrook NJ. Cellular response to oxidative stress: signaling for suicide and survival. J Cell Physiol. 2002;192:1–15.
56. German OL, Insua MF, Gentili C, Rotstein NP, Politi LE. Docosahexaenoic acid prevents apoptosis of retina photoreceptors by activating the ERK/MAPK pathway. J Neurochem. 2006;98:1507–20.
57. Agca C, Gubler A, Traber G, Beck C, Imsand C, Ail D, et al. p38 MAPK signaling acts upstream of LIF-dependent neuroprotection during photoreceptor degeneration. Cell Death Dis. 2013;4:e785.
58. Barber AJ, Nakamura M, Wolpert EB, Reiter CE, Seigel GM, Antonetti DA, et al. Insulin rescues retinal neurons from apoptosis by a phosphatidylinositol 3-kinase/Akt-mediated mechanism that reduces the activation of caspase-3. J Biol Chem. 2001;276: 32814–21.
59. Xia Z, Dickens M, Raingeaud J, Davis RJ, Greenberg ME. Opposing effects of ERK and JNK-p38 MAP kinases on apoptosis. Science. 1995;270:1326–31.
60. Yasuda S, Liang MH, Marinova Z, Yahyavi A, Chuang DM. The mood stabilizers lithium and valproate selectively activate the promoter IV of brain-derived neurotrophic factor in neurons. Mol Psychiatry. 2009;14:51–9.
61. LaVail MM, Unoki K, Yasumura D, Matthes MT, Yancopoulos GD, Steinberg RH. Multiple growth factors, cytokines, and neurotrophins rescue photoreceptors from the damaging effects of constant light. Proc Natl Acad Sci USA. 1992;89:11249–53.
62. Ait-Ali N, Fridlich R, Millet-Puel G, Clerin E, Delalande F, Jaillard C, et al. Rod-derived cone viability factor promotes cone survival by stimulating aerobic glycolysis. Cell. 2015;161:817–32.
63. Mitter SK, Song C, Qi X, Mao H, Rao H, Akin D, et al. Dysregulated autophagy in the RPE is associated with increased susceptibility to oxidative stress and AMD. Autophagy. 2014;10:1989–2005.
64. Rodriguez-Muela N, Hernandez-Pinto AM, Serrano-Puebla A, Garcia-Ledo L, Latorre SH, de la Rosa EJ, et al. Lysosomal membrane permeabilization and autophagy blockade contribute to photoreceptor cell death in a mouse model of retinitis pigmentosa. Cell Death Differ. 2015;22:476–87.
65. True O, Matthias P. Interplay between histone deacetylases and autophagy-from cancer therapy to neurodegeneration. Immunol Cell Biol. 2012;90:78–84.
66. Finnin MS, Donigian JR, Cohen A, Richon VM, Rifkind RA, Marks PA, et al. Structures of a histone deacetylase homologue bound to the TSA and SAHA inhibitors. Nature 1999;401:188–93.
67. Vanhaecke T, Papeleu P, Elaut G, Rogiers V. Trichostatin A-like hydroxamate histone deacetylase inhibitors as therapeutic agents: toxicological point of view. Curr Med Chem. 2004;11:1629–43.
68. Elaut G, Torok G, Vinken M, Laus G, Papeleu P, Tourwe D, et al. Major phase I biotransformation pathways of Trichostatin a in rat hepatocytes and in rat and human liver microsomes. Drug Metab Dispos. 2002;30:1320–8.
69. Vighi E, Trifunovic D, Veiga-Crespo P, Rentsch A, Hoffmann D, Sahaboglu A, et al. Combination of cGMP analogue and drug delivery system provides functional protection in hereditary retinal degeneration. Proc Natl Acad Sci USA. 2018;115:E2997–3006.
70. Agoston DV. How to translate time? The temporal aspect of human and rodent biology. Front Neurol. 2017;8:92.
71. Shah RR. Safety and tolerability of histone deacetylase (HDAC) inhibitors in oncology. Drug Saf. 2019;42:235–45.
72. Yao J, Qiu Y, Frontera E, Jia L, Khan NW, Klionsky DJ, et al. Inhibiting autophagy reduces retinal degeneration caused by protein misfolding. Autophagy. 2018;14:1226–38.
73. Samardzija M, Wenzel A, Naash M, Reme CE, Grimm C. Rpe65 as a modifier gene for inherited retinal degeneration. Eur-JNeurosci. 2006;23:1028–34.
74. Blank T, Goldmann T, Koch M, Amann L, Schon C, Bonin M, et al. Early microglia activation precedes photoreceptor degeneration in a mouse model of CNGB1-linked retinitis pigmentosa. Front Immunol. 2017;8:1930.
75. Romero D. HDAC inhibitors tested in phase III trial. Nat Rev Clin Oncol. 2019;16:465.
76. Cuadrado-Tejedor M, Garcia-Barroso C, Sanchez-Arias JA, Rabal O, Perez-Gonzalez M, Mederos S, et al. A first-in-class small-molecule that acts as a dual inhibitor of HDAC and PDE5 and that rescues hippocampal synaptic impairment in Alzheimer's disease mice. Neuropsychopharmacology. 2017;42:524–39.
77. Colussi C, Mozzetta C, Gurtner A, Illi B, Rosati J, Straino S, et al. HDAC2 blockade by nitric oxide and histone deacetylase inhibitors reveals a common target in Duchenne muscular dystrophy treatment. Proc Natl Acad Sci USA. 2008;105:19183–7.
78. Bressler NM. Age-related macular degeneration is the leading cause of blindness. JAMA. 2004;291:1900–1.
79. Curcio CA, Medeiros NE, Millican CL. Photoreceptor loss in age-related macular degeneration. Invest Ophthalmol Vis Sci. 1996;37:1236–49.

ACKNOWLEDGEMENTS

I would like to thank all of those I have met during these years, at NMI, at the University and everywhere around Tübingen. Tübingen was the perfect place for me to grow as a scientist and as a person.

Prof. Günther Zeck, thank you for the opportunity you gave me. In your lab, I always found everything I needed to develop my projects and reach my PhD goals. Thank you for your teaching and guidance.

I want to thank the members of my Advisory Board and the Robust Vision project, Prof. Eberart Zrenner, Prof. Jackob Macke and Prof. Katarina Sing. Having the possibility to discuss my work with scientists with your expertise has been a great privilege, and it pushed me to become a better scientist. Thank you for the helpful feedback and the fruitful discussions.

Thank you, to all the members of the Neurophysics lab: Thoralf, Miriam, MJ, Jenny, Julia, Lara, Florian, Luca. I learned so many things from you, but most importantly I always had fun.

To all the other members of the collaborative projects, especially Dr. Dragana Trifunović , Poornima Ramesh and Dr. Henner Koch, working with you has been a great opportunity to expand my interests and knowledge and do great science.

Julian Gently and Betül Uysal, I am grateful for your proof-reading and for your continued support when I needed it without ever expecting anything in return.

Nevena and Petre because you have given me a home during these years.

Marco Reato, you made me discover Tübingen, and this is only one of the many things I should thank you for. Thank you for your help during these years and especially at the beginning of this journey.

E in fine, un grazie alla mia famiglia per aver sempre creduto in me. Senza di voi questo non sarebbe stato possibile, Grazie.